Distant Retrograde Orbits

Modeling and Stability

Dominik M. Stahl

Technische Universiteit Delft

TU Delft

Distant Retrograde Orbits

Modeling and Stability

by

Dominik M. Stahl

to obtain the degree of

Master of Science
in Aerospace Engineering

at Delft University of Technology,
to be defended publicly on Friday June 3, 2022 at 02:00 PM.

Student number:	5144825	
Project duration:	January 13, 2021 – June 3, 2022	
Thesis committee:	Dr.ir. W. (Wouter) van der Wal,	TU Delft, chair
	ir. R. (Ron) Noomen,	TU Delft, supervisor
	Dr. B.V.S. (Botchu) Jyoti,	TU Delft, external examiner

An electronic version of this thesis is available at `http://repository.tudelft.nl/`.

Cover picture: NASA/JPL

TU Delft

Preface and Acknowledgments

This thesis puts an end to two and a half years of studying Aerospace Engineering in Delft. Of course this project would not have been possible without the help of many.

First and foremost I would like to thank Ron, my supervisor and mentor, for accompanying me on this journey. I really needed our weekly meetings in order to stay focused on the topic and to not get lost in the forest of things that could be researched on, but are not useful for this thesis. You helped me believe that I can actually make it to the end. After talking to you, the next steps always seemed clearer to me. I will also miss the chitchat and the Dutch lessons! Furthermore, I am thanking Jeannette for a very productive meeting in the begin of the thesis project that gave me some necessary orientation. I thank the other members of the committee, Wouter and Botchu, for taking the time to dive into this topic and for being there at the defense.

I would also like to thank my family for all their support before and during my master and especially Mom for accommodating me twice for several months, which became necessary due to the pandemic that shall not be named. We made the best out of the situation and despite my sister and me being hesitant about moving back home first, we had a lot of fun there. Furthermore, I am extremely grateful for my flatmates of the past two years – Elina, Emily, Kaushik, Pietro, Willem, and Vojtěch – without whom I for sure would have turned crazy at some point during my master. Thank you also to my fellow students Daniele, Frank, Marco, my best assignment partner Salvatore, and all the other people in Delft – thanks to you I enjoyed being here! Finally, my friends Emily, Katharina, Martin, Melvin, Philipp, and Philipp had the mercy to point out the stupid grammar and spelling mistakes that I did in this thesis, for which I am thankful.

Dominik
Delft, May 2022

Abstract

Distant Retrograde Orbits (DROs) are special orbits for third bodies in two-body systems. The third body revolves around the secondary – the smaller of the two primaries – in a retrograde way, meaning the direction is opposite to the direction that the primaries revolve around each other. DROs are not close to either of the primaries, making it difficult to model them as perturbed two-body orbits.

There is no analytical solution for the initial conditions of DROs. This thesis presents a novel method of calculating an initial velocity guess which is then fed into a differential corrector that is able to calculate the initial conditions. In contrast to the state-of-the-art, this happens without the method of incremental steps in the initial position, which requires to go through all possible DROs for a specific two-body system first.

For the calculation of DROs, numerical integration is done. Optimal integrator settings are determined, which is in this case an eighth-order Runge-Kutta method (RK8). By setting the tolerance to the lowest possible value, the accuracy requirements are satisfied.

Furthermore, this thesis explores a different method of modeling DROs that makes use of Fourier series and polynomials, which had already been proposed in [17] for a different set of parameters. By exploiting explicit knowledge about the shape of DROs, this approach is made more efficient in terms of accuracy per Fourier/polynomial parameters needed and thus the computation time is enhanced.

The second part of this study addresses the stability of DROs. This is analyzed in order to get an idea of what DROs would be suitable for future missions. For mass ratios of primary and secondary that realistically occur in the Solar System, all DROs that are closer to the secondary than the primary turn out to be stable when disregarding perturbations. Perturbations are modeled as a constant external acceleration with a constant direction, which is only a first step towards modeling the Sun's and other planet's point mass gravity (p.m.g.), the solar radiation pressure (s.r.p.), and other perturbations, as they are usually depending on time and position. With this rough estimate, only the Sun's p.m.g. is identified as a possible source of instability for DROs in the Earth-Moon system, as all other perturbations are too small.

Contents

List of Abbreviations

CM	Combined Method
CNSA	Chinese National Space Administration
CR3BP	Circular Restricted Three-Body Problem
DOP853	Eigth-Order Variable Step Size Runge-Kutta Method
DRO	Distant Retrograde Orbit
EMLS	Earth-Moon Like System
ISS	International Space Station
ivp	Initial Value Problem
MRSS	Modified Root Sum Squared
n.c.	Normalized Coordinate
PCLS	Pluto-Charon Like System
PCR3BP	Perturbed Circular Restricted Three-Body Problem
p.m.g.	Point Mass Gravity
RK	Runge-Kutta
RK8	Eighth-Order Runge-Kutta Method
RSS	Root Sum Squared
SELS	Sun-Earth Like System
s.h.g.	Spherical Harmonics Gravity
SJLS	Sun-Jupiter Like System
s.r.p.	Solar Radiation Pressure

List of Symbols

Symbol	Explanation	Unit

Latin Symbols

A	Spacecraft's Surface Area	[m^2]
a	Semi-Major Axis	[m] or [-] (n.c.)
a	Left Border for the CM	[-]
a	Parameter of $w_{a,b}$	[-]
a_0 to a_N	Fourier Coefficients	[-]
$a_\oplus$	Semi-Major Axis of Earth	[m]
a_a	Absolute Acceleration	[$m\,s^{-2}$]
a_{lm}	Acceleration from s.h.g. with Degree l and Order m	[$m\,s^{-2}$]
a_p	Semi-Major Axis of Planet p	[m]
a_r	Relative Acceleration	[$m\,s^{-2}$]
$a_{\text{s.r.p.}}$	Acceleration from s.r.p.	[$m\,s^{-2}$]
a_x	External Acceleration in x-Direction	[-]
a_y	External Acceleration in y-Direction	[-]
b	Right Border for the CM	[-]
b	Parameter of $w_{a,b}$	[-]
b_0 to b_N	Fourier Coefficients	[-]
C	Jacobi Constant	[-] (n.c.)
C	Order of Polynomial	[-]
$\bar{C}_{lm}$	Normalized Spherical Harmonics Gravity Field Coefficient	[-]
c	Parameter in New Set of Elements	[-]
d	Parameter in Derivation of New Set of Elements	[-]
d_1, d_2	Diameters of Primary and Secondary	[m]
d_0 to d_C	Polynomial Parameters	[-]
$d_{\oplus\leftmoon}$	Distance between Earth and Moon	[m]
d_p	Distance between Earth and Planet p	[m]
e	Eccentricity	[-]
f	Factor for MRSS	[-]
f	Common Logarithm of State Residual	[-]
G	Universal Gravitational Constant	[$m^3\,kg^{-1}\,s^{-2}$] or [-] (n.c.)
$\mathbf{I}_{6\times6}$	6-by-6 Identity Matrix	[-]
$\Im$	Imaginary Part	[-]
l	Spherical Harmonics Degree	[-]
$\mathbf{M}$	Monodromy Matrix	[-] (n.c.)
m	Mass	[kg] or [-] (n.c.)
m	Spherical Harmonics Order	[-]
m_1, m_2	Masses of Primary and Secondary	[kg] or [-] (n.c.)
$m_\oplus$	Mass of Earth	[kg]
m_p	Mass of Planet p	[kg]
N	Order of Fourier Series	[-]
n	Index of Fourier Coefficient	[-]
n	Order of RK Method	[-]
$\bar{P}_{lm}$	Normalized Associated Legendre Polynomial	[-]
p	Fourier Coefficients	[-]

$\Re$	Real Part	[-]
$R_\oplus$	Radius of Earth	[m]
r	Distance to Main Body	[m] or [-] (n.c.)
r	Distance to Secondary	[-] (n.c.)
r	Distance to Center of Earth	[m]
r_1, r_2	Radii of Primary and Secondary	[m]
r_1, r_2	Distances from Primary and Secondary	[-] (n.c.)
$\bar{S}_{lm}$	Normalized Spherical Harmonics Gravity Field Coefficient	[-]
s	Index of Polynomial Coefficient	[-]
t	Time	[-] (n.c.)
t_0	Initial Time	[-] (n.c.)
$t_{1/2}$	Time after 0.5 Revolutions	[-] (n.c.)
U	Potential in CR3BP	[-] (n.c.)
U	Potential in PCR3BP	[-] (n.c.)
U	Potential from s.h.g.	[$m^2\,s^{-2}$]
U_{lm}	Potential from s.h.g. with Degree l and Order m	[$m^2\,s^{-2}$]
V	Velocity in Vis-Viva Equation	[$m\,s^{-1}$] or [-] (n.c.)
V_c	Velocity on Circular Orbit	[$m\,s^{-1}$] or [-] (n.c.)
$w_{a,b}$	Logarithm of State Residual Function	[-]
$\mathbf{X}$	State Vector	[-] (n.c.)
$\mathbf{X}_0$	Initial State Vector	[-] (n.c.)
$\mathbf{X}_{1/2}$	State Vector after 0.5 Revolutions	[-] (n.c.)
$\mathbf{X}_1$	State Vector after One Revolution	[-] (n.c.)
$\mathbf{X}_n$	State Vector after n Revolutions	[-] (n.c.)
$\dot{\mathbf{X}}$	Time-Derivative of State Vector	[-] (n.c.)
X_1 to X_4	Two-Dimensional State Components	[-] (n.c.)
X_1 to X_6	Three-Dimensional State Components	[-] (n.c.)
$\dot{X}_1$ to $\dot{X}_6$	Time Derivatives of State Components	[-] (n.c.)
x	Coordinate in CR3BP	[-] (n.c.)
x	Common Logarithm of Step Size Δt	[-]
x_0	Initial x-Coordinate	[-] (n.c.)
$x_{1/2}$	x-Coordinate after 0.5 Revolutions	[-] (n.c.)
x_1	x-Coordinate after One Revolution	[-] (n.c.)
x_1, x_2	x-Coordinates of Primary and Secondary	[-] (n.c.)
$\dot{x}$	x-Velocity	[-] (n.c.)
$\dot{x}_0$	Initial x-Velocity	[-] (n.c.)
$\dot{x}_{1/2}$	x-Velocity after 0.5 Revolutions	[-] (n.c.)
$\dot{x}_1$	x-Velocity after One Revolution	[-] (n.c.)
$\ddot{x}$	x-Acceleration	[-] (n.c.)
$\ddot{x}_0$	Initial x-Acceleration	[-] (n.c.)
$\ddot{x}_{1/2}$	x-Acceleration after 0.5 Revolutions	[-] (n.c.)
$\ddot{x}_1$	x-Acceleration after One Revolution	[-] (n.c.)
y	Coordinate in CR3BP	[-] (n.c.)
y_0	Initial y-Coordinate	[-] (n.c.)
$y_{1/2}$	y-Coordinate after 0.5 Revolutions	[-] (n.c.)
y_1	y-Coordinate after One Revolution	[-] (n.c.)
y_1, y_2	y-Coordinates of Primary and Secondary	[-] (n.c.)
$\dot{y}$	y-Velocity	[-] (n.c.)
$\dot{y}_0$	Initial y-Velocity	[-] (n.c.)
$\dot{y}_{1/2}$	y-Velocity after 0.5 Revolutions	[-] (n.c.)
$\dot{y}_1$	y-Velocity after One Revolution	[-] (n.c.)
$\ddot{y}$	y-Acceleration	[-] (n.c.)
$\ddot{y}_0$	Initial y-Acceleration	[-] (n.c.)
$\ddot{y}_{1/2}$	y-Acceleration after 0.5 Revolutions	[-] (n.c.)
$\ddot{y}_1$	y-Acceleration after One Revolution	[-] (n.c.)
z	Coordinate in CR3BP	[-] (n.c.)
z_1, z_2	z-Coordinates of Primary and Secondary	[-] (n.c.)
$\dot{z}$	z-Velocity	[-] (n.c.)
$\ddot{z}$	z-Acceleration	[-] (n.c.)

Greek Symbols

α	Parameter in Derivation of New Set of Elements	[-]
β	Parameter in Derivation of New Set of Elements	[-]
Δ	Variation, Step	*Operator*
θ	Angle in [17]	[rad]
θ	Angle for Spherical Harmonics	[rad]
λ	Eigenvalue	[-]
λ_1 to λ_6	Eigenvalues of $\mathbf{M}$	[-]
μ	Mass Ratio of Primary and Secondary	[-]
$\mathbf{\Phi}$	State Transition Matrix	[-] (n.c.)
$\mathbf{\Phi}_{1/2}$	$\mathbf{\Phi}$ after 0.5 Revolutions	[-] (n.c.)
$\mathbf{\Phi}_1$	$\mathbf{\Phi}$ after One Revolution	[-] (n.c.)
Σ	Sum	*Operator*
$\Phi_{1,1}$ to $\Phi_{6,6}$	Entries of $\mathbf{\Phi}$	[-] (n.c.)
ϕ	Angle in CR3BP	[rad]
ϕ	Angle for Spherical Harmonics	[rad]
ψ	Parameter in New Set of Elements	[-]

Other Symbols

∂	Operator for Partial Derivatives	*Operator*
∞	Infinity	[-]
∇	Nabla Operator	*Operator*

1 Introduction

Distant Retrograde Orbits (DROs) are considered the most stable orbits for third bodies in two-body systems [5–7, 14, 26, 27, 30, 38, 49], and yet – at the start of this thesis project – no information about a human-made object performing a real mission in a DRO could be found in literature. This is either because no human-made object has done this or just because it has not been made public. Because of their stability, DROs in the Earth-Moon system would be the perfect target orbits for potential asteroid retrieval mission [31]. They could make sure that the asteroid does not escape the Earth-Moon system, nor alter its orbit and crash into Earth or Moon. Also a space station, that could be used as a space hub for interplanetary travels, would profit from being in an Earth-Moon DRO. The distance to Earth would make it a good location for a refill station – and the propellant could be supplied by the aforementioned asteroid [28].

Before this comes true, however, investigations regarding DROs have to be made. They are influenced by two main attracting bodies at the same time, which makes them different from most orbits. Usually, orbits can be modeled as elliptic two-body orbits with a third body that is perturbing the orbit. However, the two bodies from the two-body system (like the Earth-Moon system) are both too important for the DROs to be considered as just a perturbation. Therefore, the research question formulated for this thesis is:

What investigations are needed in order to do the orbit design for a future DRO mission?

The two sub-questions are:

1. **How can DROs be modeled efficiently in order to make the orbit design of missions that include DROs easier?**
2. **What DROs would be stable enough to be interesting for future missions?**

The first sub-question will be answered for a general mass ratio μ, whereas the second will focus primarily on the Earth-Moon system.

This thesis report is structured as follows. Chapter 2 tells more about the historic use of DROs and how they have been modeled so far using a Fourier series presented in [17]. Chapter 3 explains the theory that is needed to understand this thesis project. Chapter 4 is aimed at finding initial conditions for DROs based on the differential corrector – and presents starting values for it that are more efficient than the method of incremental changes. Chapter 5 evaluates different integrator settings in order to select those that satisfy the accuracy requirements. Chapter 6 models DROs with Fourier series and uses a better approach for that than [17]. Chapter 7 deals with the stability of DROs – with and without regarding possible perturbations. Chapter 8 supplies verification and validation results to confirm the correctness of the models and implementations that were used in this thesis project. Finally, conclusions and recommendations for future work can be found in Chapter 9. This is followed by Appendix A, presenting additional figures for Chapter 4, Appendix B with additional figures for Chapter 5, Appendix C explaining how to calculate the velocity in Chapter 6, and Appendix D with an explanation for the Jacobi constant in a perturbed version of the circular restricted three-body problem that is needed in Chapter 7.

2

Heritage

DROs have not been investigated extensively and at the start of the thesis project, they have also never been flown by a human-made spacecraft – to the best of the author's knowledge. Therefore, the available research is quite limited. Nevertheless, this chapter will describe a DRO mission that was performed by the Chinese National Space Administration (CNSA) as part of the *Chang'e-5* mission. Furthermore, research that has been done so far on the modeling and stability of DROs is briefly summarized.

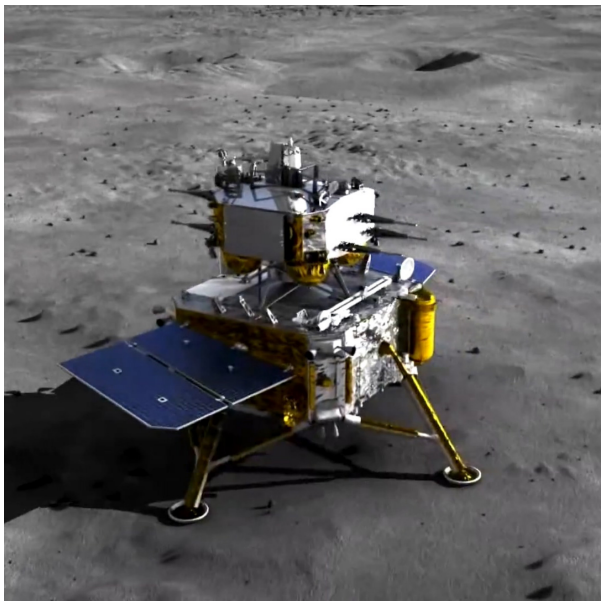

Figure 2.1: Lander of the *Chang'e-5* mission on the Moon's surface. Artist's impression by the *China News Service*.

Only one human-made spacecraft has performed DROs around the Moon so far. The current status of this spacecraft is unknown, in fact it might still be in a DRO. The Chinese *Chang'e-5* mission was originally a lunar sample return mission, and this objective was successfully carried out in 2020, as described in [43]. The lunar lander is illustrated in Figure 2.1. After delivering the Moon's samples to Earth, the service module flew to the Sun-Earth L1-point [43]. According to [2, 24], it has been reported by amateur satellite tracker Scott Tilley and others that the service module has entered an Earth-Moon DRO between September 2021 and January 2022. The module "is probably conducting enabling telemetry, tracking and control and Very Long Baseline Interferometry (VLBI) tests to support Chinese preparations for the next stage of China's Lunar Exploration Program (CLEP)" [24].

When it comes to research on DROs, their existence has been suggested by George William Hill already in the 19th century [15, 16], according to [9]. In their history of scientific discussion, DROs have had different names: According to [14], DROs have been know as “family a” orbits by Takehiko Matukuma in [29] and as “family f” orbits by Bengt Strömgren. The fact that DROs are more stable than their prograde counterparts was already assessed by John Jackson in 1913, who wrote about “remote retrograde satellites” in [18]. Also Michel Hénon stated in [14] that DROs are the only family of symmetric periodic orbits in a two-body system that are stable no matter the orbit size. However, this statement refers to the Hill problem, which (among other things) assumes the secondary to have a negligible mass. Therefore, it can not be applied to an arbitrary two-body system.

When it comes to modeling DROs, [17] has made an interesting attempt that uses Fourier series and Chebyshev polynomials. With their approach, an entire family of DROs can be modeled at the same time, rather than only one specific DRO. This is beneficial for mission planning, for example when the exact target DRO is not decided on yet, as both the position and the velocity can be obtained as derivable functions of both the location along a specific orbit and the orbit within the family of orbits.

3

Theory

In order to model DROs, an idealized version of the three-body problem – the circular restricted three-body problem (CR3BP) – will be introduced in Sections 3.1 and 3.2. Furthermore, some widely used astrodynamics concepts such as the state transition matrix and the differential corrector are presented in Sections 3.3 and 3.4. Finally, some real-life two-body systems in which a third body can perform DROs are discussed in Section 3.5.

3.1. Circular Restricted Three-Body Problem

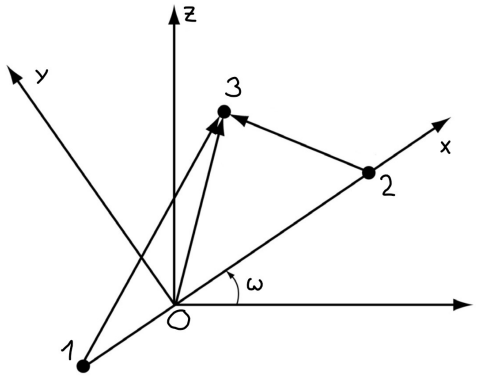

Figure 3.1: Depiction of the coordinate axes in the CR3BP. The origin O is at the barycenter of the primary (1) and the secondary (2), with all three of them lying on the x-axis. The coordinate system – in which the position of the third body (3) is expressed – is rotating about the z-axis with angular velocity ω. [50].

In the CR3BP two bodies – the heavier of which will be called *primary* and the other one *secondary* – are assumed to revolve around their common barycenter in circular orbits. The xyz-coordinate system is oriented such that its origin is in the barycenter of primary and secondary. The x-axis is directed such that the secondary is positioned on its positive direction and the primary on its negative direction. Since the coordinate system is co-rotating with primary and secondary, their positions on the x-axis are fixed. The z-axis points in the direction of the angular momentum of primary and secondary. Therefore, the y-axis – perpendicular to the x- and the z-axis – is in the plane in which primary and secondary rotate. This can be seen in Figure 3.1. In the common representation of the CR3BP, all units in the CR3BP are dimensionless. The mass ratio μ of primary (indicated with index 1) and secondary (indicated with index 2) defines the CR3BP:

$$\mu = \frac{m_2}{m_1 + m_2} \tag{3.1}$$

Then, the positions $x_{1/2}$ of primary and secondary are:

$$x_1 = -\mu, \qquad x_2 = 1 - \mu \tag{3.2}$$

The angular velocity is 1 in z-direction. This assumes the total mass $m_1 + m_2$ to be 1 and the universal gravitational constant G to be 1 as well.

Now, if a third body that has a negligible mass (and therefore does not influence the circular motion of primary and secondary) is inserted into the system, its equations of motion are [50, Equation (3.46)]:

$$\ddot{x} = \underbrace{x}_{\text{centrifugal}} \underbrace{-\frac{1-\mu}{r_1^3}(\mu + x) + \frac{\mu}{r_2^3}(1 - \mu - x)}_{\text{gravitational}} \underbrace{+2\dot{y}}_{\text{Coriolis}} \tag{3.3}$$

$$\ddot{y} = \underbrace{y}_{\text{centrifugal}} \underbrace{-\frac{1-\mu}{r_1^3}y - \frac{\mu}{r_2^3}y}_{\text{gravitational}} \underbrace{-2\dot{x}}_{\text{Coriolis}} \tag{3.4}$$

$$\ddot{z} = \underbrace{-\frac{1-\mu}{r_1^3}z - \frac{\mu}{r_2^3}z}_{\text{gravitational}} \tag{3.5}$$

Here, r_1 and r_2 are the distances from the third body to the primary and the secondary, respectively:

$$r_1 = \sqrt{(x - x_1)^2 + (y - y_1)^2 + (z - z_1)^2} = \sqrt{(x + \mu)^2 + y^2 + z^2} \tag{3.6}$$

$$r_2 = \sqrt{(x - x_2)^2 + (y - y_2)^2 + (z - z_2)^2} = \sqrt{(x - 1 + \mu)^2 + y^2 + z^2} \tag{3.7}$$

The gravitational and centrifugal part of the acceleration can be written as partial derivatives of a potential U (because they are conservative forces), which is:

$$U = \underbrace{\frac{1}{2}(x^2 + y^2)}_{\text{centrifugal}} + \underbrace{\frac{1-\mu}{r_1} + \frac{\mu}{r_2}}_{\text{gravitational}} \tag{3.8}$$

Then, the acceleration simplifies to:

$$\begin{bmatrix} \ddot{x} \\ \ddot{y} \\ \ddot{z} \end{bmatrix} = \nabla U + \underbrace{\begin{bmatrix} 2\dot{y} \\ -2\dot{x} \\ 0 \end{bmatrix}}_{\text{Coriolis}} = \begin{bmatrix} \partial U/\partial x + 2\dot{y} \\ \partial U/\partial y - 2\dot{x} \\ \partial U/\partial z \end{bmatrix} \tag{3.9}$$

In the CR3BP, it is possible to define a constant C, which can be written as [50, Equation (3.54)]:

$$C = U - \frac{1}{2}(\dot{x}^2 + \dot{y}^2 + \dot{z}^2) \tag{3.10}$$

It is usually referred to as the Jacobi constant.

3.2. Propagation

For the CR3BP, propagation is usually done in the co-rotating Cartesian coordinate system that has been described in the previous section. Depending on the application, this is done in two dimensions in the xy-plane or in three dimensions by including the z-direction. The state $\mathbf{X}$ is then represented by one of the following equations:

$$\mathbf{X} = \begin{bmatrix} X_1 & X_2 & X_3 & X_4 \end{bmatrix}^\mathsf{T} = \begin{bmatrix} x & y & \dot{x} & \dot{y} \end{bmatrix}^\mathsf{T} \tag{3.11}$$

$$\mathbf{X} = \begin{bmatrix} X_1 & X_2 & X_3 & X_4 & X_5 & X_6 \end{bmatrix}^\mathsf{T} = \begin{bmatrix} x & y & z & \dot{x} & \dot{y} & \dot{z} \end{bmatrix}^\mathsf{T} \tag{3.12}$$

With no loss of generality, the propagation of the three-dimensional state is discussed here. The accelerations $\ddot{x}$, $\ddot{y}$, and $\ddot{z}$ are functions of the state $\mathbf{X}$ itself and can be calculated from Equation (3.9). Therefore, the time-derivative of the state $\mathbf{X}$ is:

$$\dot{\mathbf{X}} = \begin{bmatrix} \dot{X}_1 \\ \dot{X}_2 \\ \dot{X}_3 \\ \dot{X}_4 \\ \dot{X}_5 \\ \dot{X}_6 \end{bmatrix} = \begin{bmatrix} \dot{x} \\ \dot{y} \\ \dot{z} \\ \ddot{x} \\ \ddot{y} \\ \ddot{z} \end{bmatrix} = \begin{bmatrix} X_4 \\ X_5 \\ X_6 \\ \ddot{x}(\mathbf{X}) \\ \ddot{y}(\mathbf{X}) \\ \ddot{z}(\mathbf{X}) \end{bmatrix} \tag{3.13}$$

This represents a system of first-order differential equations and can therefore be propagated using the known techniques for initial value problems (ivps), of which some are discussed in Chapter 5.

3.3. State Transition Matrix

The state transition matrix $\mathbf{\Phi}(t, t_0)$ is a useful and widely used tool in astrodynamics. In this thesis, it us used for the differential corrector in Section 3.4 and Chapter 4 and for stability considerations in Chapter 7. The state transition matrix $\mathbf{\Phi}(t, t_0)$ at any time t indicates how the state $\mathbf{X}(t)$ changes depending on how one changes the state $\mathbf{X}(t_0)$:

$$\mathbf{\Phi}(t, t_0) = \frac{\partial \mathbf{X}(t)}{\partial \mathbf{X}(t_0)} \qquad \text{or} \qquad \Phi_{i,j}(t, t_0) = \frac{\partial X_i(t)}{\partial X_j(t_0)} \quad \forall\, i, j \in (1, 6) \tag{3.14}$$

By definition, the state transition matrix $\mathbf{\Phi}(t_0, t_0)$ at time $t = t_0$ equals the identity matrix:

$$\mathbf{\Phi}(t_0, t_0) = \mathbf{I}_{6\times 6} \tag{3.15}$$

The state transition matrix $\mathbf{\Phi}(t, t_0)$ can be propagated with [37, Chapter 2]:

$$\dot{\mathbf{\Phi}}(t, t_0) = \frac{\partial \dot{\mathbf{X}}(t)}{\partial \mathbf{X}(t)} \mathbf{\Phi}(t, t_0) \tag{3.16}$$

It should be noted that predictions for the state $\mathbf{X}(t)$ that the state transition matrix $\mathbf{\Phi}(t, t_0)$ makes are not fully accurate, as they are assuming linearity; for predicting the effect of small variations in the initial state $\mathbf{X}(t_0)$ this is fully acceptable.

3.4. Differential Corrector

A tool to find exact initial conditions for closed orbits is the differential corrector. The concept is for example described in [4, 8, 10, 37, 39]. If a "good guess" for the initial conditions of a DRO is available, the differential corrector can be used to refine the initial conditions and find initial conditions that actually belong to a DRO. It makes use of the state transition matrix $\mathbf{\Phi}(t, t_0)$.

For finding the initial conditions of DROs, the fact is exploited that the velocity component $\dot{x}$ is zero at the two locations where the orbit crosses the x-axis due to the symmetries of the CR3BP. Therefore, an initial guess $\mathbf{X}_0$ for the state $\mathbf{X}(0)$ would be:

$$\mathbf{X}_0 = \begin{bmatrix} x_0 & 0 & 0 & \dot{y}_0 \end{bmatrix}^\mathsf{T} \tag{3.17}$$

If x_0 is smaller than x_2, meaning that the DRO starts between primary and secondary, the velocity component $\dot{y}_0$ has to be positive in order to obtain a retrograde orbit; if x_0 is greater than x_2, $\dot{y}_0$ has to be negative. This initial guess $\mathbf{X}_0$ is now propagated until the x-axis is being crossed again, this is after one half of an orbit at $t = t_{1/2}$. The state that results is denoted with $\mathbf{X}_{1/2}$. By definition, its y-component is zero:

$$\mathbf{X}_{1/2} = \begin{bmatrix} x_{1/2} & 0 & \dot{x}_{1/2} & \dot{y}_{1/2} \end{bmatrix}^\mathsf{T} \tag{3.18}$$

Due to symmetry, the velocity component $\dot{x}_{1/2}$ is desired to be zero. Along with the state, also the state transition matrix is propagated. The state transition matrix after half an orbit is denoted with $\mathbf{\Phi}_{1/2}$:

$$\mathbf{\Phi}_{1/2} = \mathbf{\Phi}(t_{1/2}, t_0) = \frac{\partial \mathbf{X}_{1/2}}{\partial \mathbf{X}_0} = \begin{bmatrix} \Phi_{1,1} & \Phi_{1,2} & \Phi_{1,3} & \Phi_{1,4} \\ \Phi_{2,1} & \Phi_{2,2} & \Phi_{2,3} & \Phi_{2,4} \\ \Phi_{3,1} & \Phi_{3,2} & \Phi_{3,3} & \Phi_{3,4} \\ \Phi_{4,1} & \Phi_{4,2} & \Phi_{4,3} & \Phi_{4,4} \end{bmatrix} \tag{3.19}$$

By the definition of the state transition matrix $\mathbf{\Phi}_{1/2}$, the change $\Delta\mathbf{X}_{1/2}$ in state after half an orbit that results from the initial change $\Delta\mathbf{X}_0$ in state can be approximated with:

$$\Delta\mathbf{X}_{1/2} = \mathbf{\Phi}_{1/2}\Delta\mathbf{X}_0 + \Delta t\dot{\mathbf{X}}_{1/2} \tag{3.20}$$

or

$$\begin{bmatrix} \Delta x_{1/2} \\ \Delta y_{1/2} \\ \Delta \dot{x}_{1/2} \\ \Delta \dot{y}_{1/2} \end{bmatrix} = \begin{bmatrix} \Phi_{1,1} & \Phi_{1,2} & \Phi_{1,3} & \Phi_{1,4} \\ \Phi_{2,1} & \Phi_{2,2} & \Phi_{2,3} & \Phi_{2,4} \\ \Phi_{3,1} & \Phi_{3,2} & \Phi_{3,3} & \Phi_{3,4} \\ \Phi_{4,1} & \Phi_{4,2} & \Phi_{4,3} & \Phi_{4,4} \end{bmatrix} \begin{bmatrix} \Delta x_0 \\ \Delta y_0 \\ \Delta \dot{x}_0 \\ \Delta \dot{y}_0 \end{bmatrix} + \Delta t \begin{bmatrix} \dot{x}_{1/2} \\ \dot{y}_{1/2} \\ \ddot{x}_{1/2} \\ \ddot{y}_{1/2} \end{bmatrix} \tag{3.21}$$

The last term takes into account that the time $t_{1/2}$ that is needed to reach the x-axis might not be the same before and after applying the change $\Delta\mathbf{X}_0$ to the initial state $\mathbf{X}_0$. The system of four linear equations in Equation (3.21) has nine unknowns (the two state changes $\Delta\mathbf{X}$ and Δt). The values of $\Delta x_{1/2}$ and $\Delta \dot{y}_{1/2}$ do not matter, therefore the first and the last equation can be neglected. More importantly, $\Delta y_{1/2}$ has to be 0 and $\Delta \dot{x}_{1/2}$ has to be $-\dot{x}_{1/2}$ in order to arrive at the x-axis with a velocity perpendicular to the x-axis. Also, if the starting position is chosen and should therefore not change, Δx_0 and Δy_0 have to be zero. Since due to the symmetry also the velocity $\dot{x}_0$ has to be zero, this also holds for $\Delta \dot{x}_0$. This results in the following system of two linear equations:

$$\begin{bmatrix} 0 \\ -\dot{x}_{1/2} \end{bmatrix} = \Delta\dot{y}_0 \begin{bmatrix} \Phi_{2,4} \\ \Phi_{3,4} \end{bmatrix} + \Delta t \begin{bmatrix} \dot{y}_{1/2} \\ \ddot{x}_{1/2} \end{bmatrix} \tag{3.22}$$

and therefore:

$$\Delta t = \frac{\dot{x}_{1/2}}{\frac{\Phi_{3,4}}{\Phi_{2,4}}\dot{y}_{1/2} - \ddot{x}_{1/2}} \qquad \text{and} \qquad \Delta\dot{y}_0 = \frac{\dot{x}_{1/2}}{\frac{\ddot{x}_{1/2}}{\dot{y}_{1/2}}\Phi_{2,4} - \Phi_{3,4}} \tag{3.23}$$

Now the first half of a DRO is attempted again with the new velocity $\dot{y}_{0,\text{new}}$:

$$\dot{y}_{0,\text{new}} \overset{\text{def}}{=} \dot{y}_{0,\text{old}} + \Delta\dot{y}_0 \tag{3.24}$$

This can be repeated until the remaining x-velocity $\dot{x}_{1/2}$ is considered small enough.

3.5. Selecting Mass Ratios

The mass ratio μ is the most important parameter for two-body systems. Therefore, the existing mass ratios in the Solar System shall be investigated, for which three kinds of two-body systems should be considered: Sun-planet systems, planet-moon systems, and binary asteroids. The mass ratios of all Sun-planet systems and the Sun-Pluto system can be found in Table 3.1, as well as some planet-moon systems and the Pluto-Charon system. The biggest values are found for the Pluto-Charon system ($\mu = 0.109$), the Earth-Moon system ($\mu = 0.0121$), and the Sun-Jupiter system ($\mu = 0.000954$). Two-body systems with lower mass ratios μ are becoming less interesting because – firstly – they are not very different from each other since the absolute value for the mass ratio μ barely changes at all and – secondly – they become more similar to the Hill problem, which is a different topic.

In order to include also binary asteroids in the considerations, Figures 3.2 and 3.3 depict the mass ratio μ plotted for all Sun-planet systems, known planet-moon systems and known binary asteroids. The mass ratios μ for the binary asteroids can only be estimated since their masses are not available but only their diameters. With assuming the density to be the same for every asteroid, the mass ratio

Table 3.1: Mass ratios μ of the Sun-planet systems and the Sun-Pluto system as well as the planet-moon systems and the Pluto-Charon system. For the Sun-planet systems, the entire planet system including the planet's moons are taken into account. This can lead to discrepancies with other sources.

(Dwarf) Planet	μ Sun-Planet [20]	Moon	μ Planet-Moon
Mercury	$1.66 \cdot 10^{-7}$		
Venus	$2.45 \cdot 10^{-6}$		
Earth	$3.04 \cdot 10^{-6}$	Moon	$1.21 \cdot 10^{-2}$ [34]
Mars	$3.23 \cdot 10^{-7}$	Phobos	$1.65 \cdot 10^{-8}$ [33]
		Deimos	$3.74 \cdot 10^{-9}$ [33]
Jupiter	$9.54 \cdot 10^{-4}$	Io	$4.70 \cdot 10^{-5}$ [32]
		Europa	$2.53 \cdot 10^{-5}$ [32]
		Ganymede	$7.81 \cdot 10^{-5}$ [32]
		Callisto	$5.67 \cdot 10^{-5}$ [32]
Saturn	$2.86 \cdot 10^{-4}$	Titan	$2.37 \cdot 10^{-4}$ [32]
Uranus	$4.36 \cdot 10^{-5}$		
Neptune	$5.14 \cdot 10^{-5}$	Triton	$2.10 \cdot 10^{-4}$ [32]
Pluto	$7.41 \cdot 10^{-9}$	Charon	$1.09 \cdot 10^{-1}$ [36]

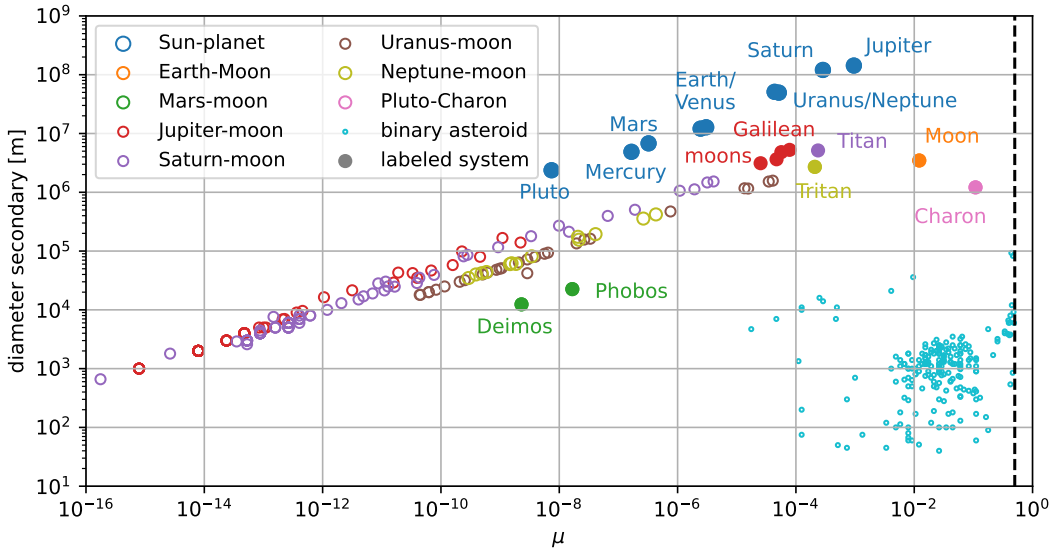

Figure 3.2: Mass ratio μ and diameter of the secondary plotted for chosen two-body systems in the Solar System. The dashed line represents $\mu = 0.5$, which is by definition the upper boundary for the mass ratio of a primary-secondary system. Mass and diameter for the moons of Jupiter, Saturn, Uranus, and Neptune are from [11, 13, 19, 21–23, 25, 40–42, 46–48, 51]. The diameters of the binary asteroids are taken from [3].

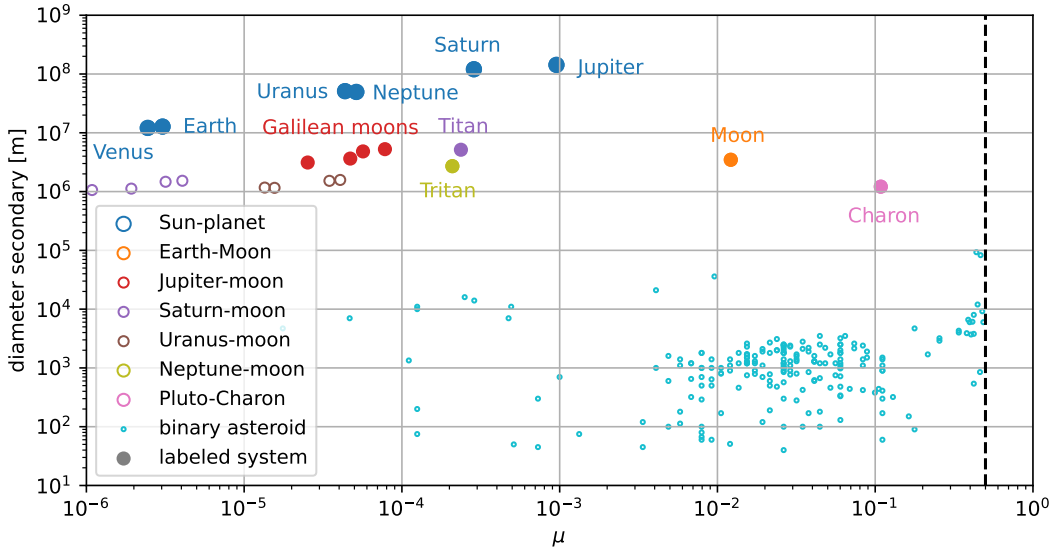

Figure 3.3: Zoom into Figure 3.2.

is the diameter ratio to the power three. The alert reader will notice that some of the binary asteroid systems seem to have the exact same value for the mass ratio μ. This is due to the low number of digits that [3] offers when it comes to the diameter ratio of primary and secondary. For example, out of the 118 binary asteroid systems that are listed, the diameter ratio r_2/r_1 occurring most often is 0.30 with 22 occurrences. This implies for the relation of the masses m_1 and m_2 and thus the mass ratio μ:

$$\frac{m_2}{m_1} = \left(\frac{d_2}{d_1}\right)^3 = \left(\frac{3}{10}\right)^3 = \frac{27}{1000} \tag{3.25}$$

$$\mu = \frac{m_2}{m_1 + m_2} = \frac{\frac{m2}{m1}}{1 + \frac{m2}{m1}} = \frac{\frac{27}{1000}}{1 + \frac{27}{1000}} = \frac{\frac{27}{1000}}{\frac{1027}{1000}} = \frac{27}{1027} \approx 0.0263 \tag{3.26}$$

and indeed at about $\mu = 0.0263$ many data points can be found.

The vertical axes of the plots represent the diameter of the secondary (since the mass of the secondary is not available for most of the binary asteroids). Noticeably, the data points that have the same body as primary lie approximately on one line in the log-log plot with the diameter changing by the factor 10 for the mass ratio μ changing by the factor 1000. This is because the density of Solar System bodies does not differ too much – the planet with the highest density is Earth with $5514\,\mathrm{kg/m^3}$ and Saturn has the lowest density of $687\,\mathrm{kg/m^3}$, making the difference less than one order of magnitude [35]. The lower the mass of the primary, the lower the line is in Figures 3.2 and 3.3, making the line with the Sun-planet systems the highest. The binary asteroids do not have a common primary and are therefore not restricted to one line. Figure 3.3 shows that with choosing the Sun-Jupiter, the Earth-Moon, and the Pluto-Charon systems as representative systems, most of the binary asteroids are covered as well when it comes to the mass ratio μ. There are only a few binary asteroids that have an even higher mass ratio than the Pluto-Charon system. On the other hand, when it comes to mass ratios that are even lower than the one in the Sun-Jupiter system, the two-body systems are quite similar to each other – as mentioned before. Therefore, one example shall be enough to cover all of them; and with the Sun-Earth system it includes our home planet.

In conclusion, with the aim of covering a representative range of mass ratios μ, the four systems that will be analyzed are the Sun-Earth like system (SELS), the Sun-Jupiter like system (SJLS), the Earth-Moon like system (EMLS), and the Pluto-Charon like system (PCLS). Note that these simplified systems assume rounded values for the mass ratio μ, as well as perfectly circular orbits, as can be read from Table 3.2. This is for the sake of simplicity and is represented in the letter “L” in the acronyms.

Table 3.2: Comparison of the simplified systems SELS, SJLS, EMLS, and PCLS with their real systems in terms of mass ratio μ and eccentricity e.

Primary	Secondary	μ	e	Simplified System	μ	e
Sun	Earth	$3.04 \cdot 10^{-6}$	0.017 [35]	SELS	$3 \cdot 10^{-6}$	0
Sun	Jupiter	$9.54 \cdot 10^{-4}$	0.049 [35]	SJLS	$1 \cdot 10^{-3}$	0
Earth	Moon	$1.21 \cdot 10^{-2}$	0.055 [34]	EMLS	$1 \cdot 10^{-2}$	0
Pluto	Charon	$1.09 \cdot 10^{-1}$	≈ 0 [36]	PCLS	$1 \cdot 10^{-1}$	0

3.6. Distant Retrograde Orbits

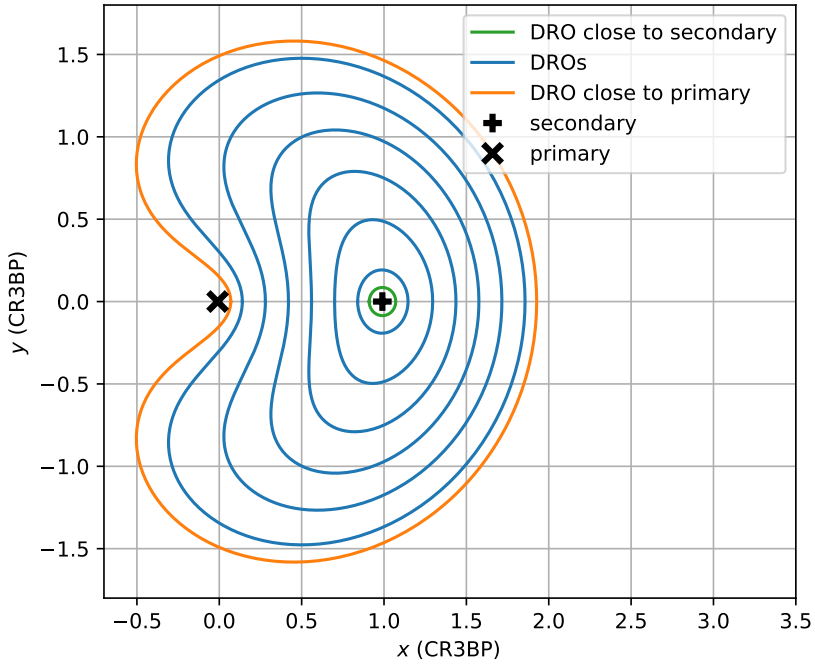

Figure 3.4: Several DROs depicted in the co-rotating reference frame. Each DRO is shown for one full revolution. $\mu = 0.01$.

DROs are orbits around the secondary of a two-body system. As the name suggests, they are retrograde, meaning they revolve around the secondary in the opposite direction of how secondary and primary are revolving around each other. From the perspective of the primary, DROs are by no means retrograde, as they revolve around the primary alongside the secondary – in a prograde way. This can better be understood when looking at Figures 3.4 to 3.6: Figure 3.4 shows various DROs with different starting positions in the co-rotating reference frame of the CR3BP, meaning that in this reference frame the primary and the secondary stay at the same position. The primaries, an thus the coordinate system, are rotating counterclockwise around the origin of this coordinate system. In this coordinate system, the DROs are clockwise. In Figure 3.5, an inertial coordinate system is depicted that coincides with the co-rotating coordinate system at time $t = 0$. In this coordinate system, the primaries are not fixed, their trajectories are depicted along which they travel counterclockwise. The DROs are counterclockwise as well, and they are shown for one full revolution around the secondary. This means that at the time that their orbit ends in Figure 3.5, the secondary is right behind the orbiting object, as seen from the primary. Then, the next orbit starts from there. This is shown for a DRO that is close to the secondary and one that starts close to the primary in Figure 3.6. The DRO close to the secondary stays close to the secondary for the entire time, while the DRO that starts close to the primary performs highly eccentric orbits whose argument of periapsis is changing a bit every orbit.

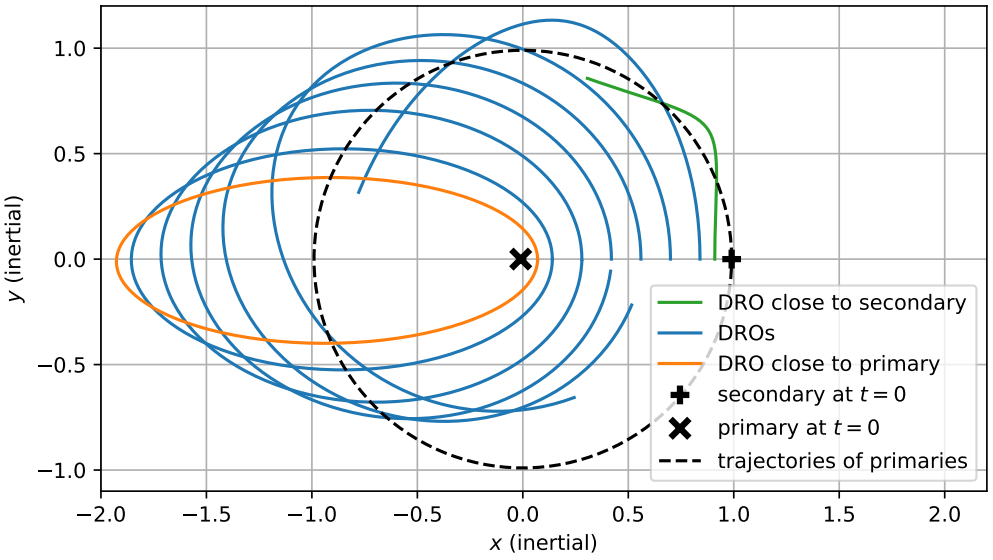

Figure 3.5: Several DROs depicted in an inertial reference frame. Each DRO is shown for one full revolution around the secondary in the co-rotating reference frame. The propagation time is about 1.23 for the green DRO, 6.30 for the orange DRO, and in between those for the blue DROs. $\mu = 0.01$.

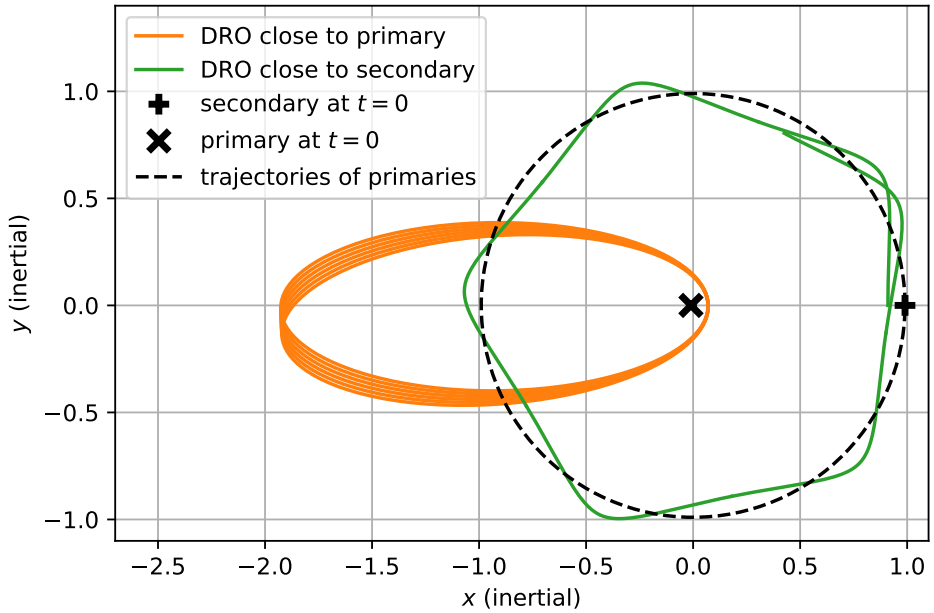

Figure 3.6: Several DROs depicted in an inertial reference frame. Each DRO is shown for exactly six revolutions around the secondary in the co-rotating reference frame. The propagation time is about 7.37 for the green DRO and 37.78 for the orange DRO. $\mu = 0.01$.

4

Initial Conditions

In order to find initial conditions for DROs in the CR3BP, the differential corrector explained in Section 3.4 is to be used. In Section 4.1, the method of incremental changes is introduced, which was also used in [17]. Sections 4.2 and 4.3 aim to find better starting velocities for the differential corrector that do not emerge from incremental changes. The enhancement that is introduced by this new technique is evaluated in Section 4.4.

4.1. Method of Incremental Changes

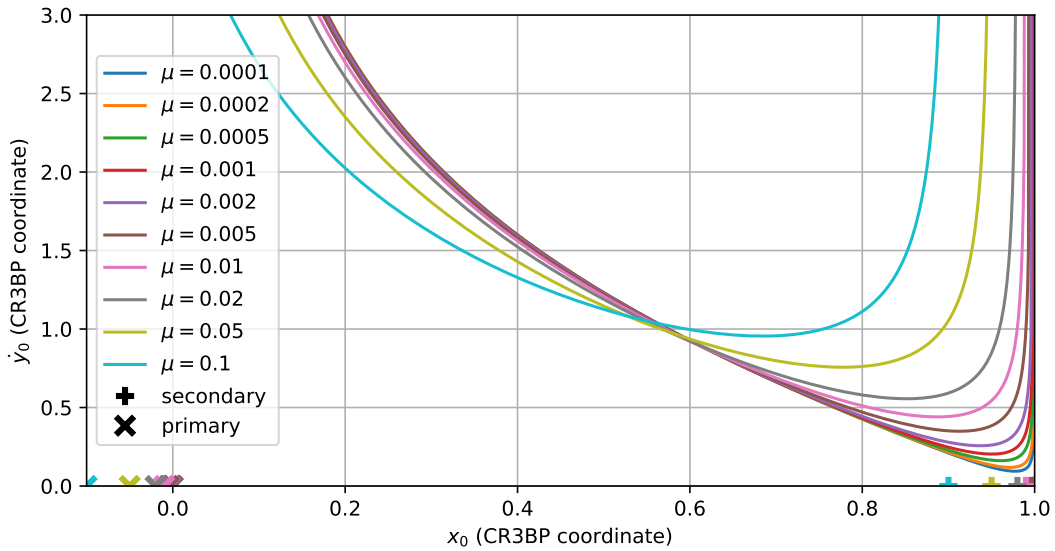

Figure 4.1: Initial velocities $\dot{y}_0$ for DROs depending on their initial position x_0 in the CR3BP with different mass ratios μ.

The differential corrector method does not work with an arbitrary initial value for the initial velocity. The reason is that in the CR3BP there are also other orbits that start and end on the x-axis with velocities perpendicular to it. Among these are Lyapunov orbits around the linear Lagrange points, orbits around the primary, and prograde orbits around the secondary. With an arbitrary initial value the differential corrector method can converge to any of those mentioned orbits and it can also not converge at all. Therefore, an initial value is needed that is already *close* to the actual value of the initial velocity in DROs. [17] proposes the following approach: Close to the secondary the initial velocity can be approximated very well by assuming a circular orbit around the secondary. Then, the differential corrector is applied in order to obtain the true initial velocity for this specific orbit. A *small* step towards the primary

is taken and the true initial velocity from the previous orbit is taken as initial guess for the next orbit. This algorithm is to be continued until the required initial distance from the secondary is reached. It is possible that the change in true initial velocity is too big. In this case the differential corrector might not converge to a DRO, which can be solved by using a smaller step size. This happens especially close to the secondary and close to the primary, since the required changes in initial velocity are relatively high there, as can be seen in Figure 4.1. It is understood that this can become a long process: For the determination of the initial conditions for a single DRO, many steps have to be taken.

The general shape of the lines in Figure 4.1 can be explained easily. In the vicinity of the secondary, it holds that a smaller distance to the secondary leads to a higher initial velocity for the DRO. The lower the mass ratio μ, the farther the initial velocity decreases when the starting position x_0 gets further away from the secondary. This is because the assumed mass of the secondary – and therefore its influence – in this two-body system decreases with decreasing mass ratio μ. When the starting position x_0 approaches the primary, the initial velocity $\dot{y}_0$ has to increase again in order to defy the primary's gravity field. Since for the mass ratios μ in Figure 4.1 (of which the greatest is 0.1), the primary has always about the same mass, the shapes of the curves close to the primary do not differ much. Only their locations do, as the primary does have a different position in the CR3BP depending on the mass ratio μ. This is reflected in the common shift along the x-axis of primary, secondary, and the initial y-velocity curve.

4.2. Better Starting Velocities

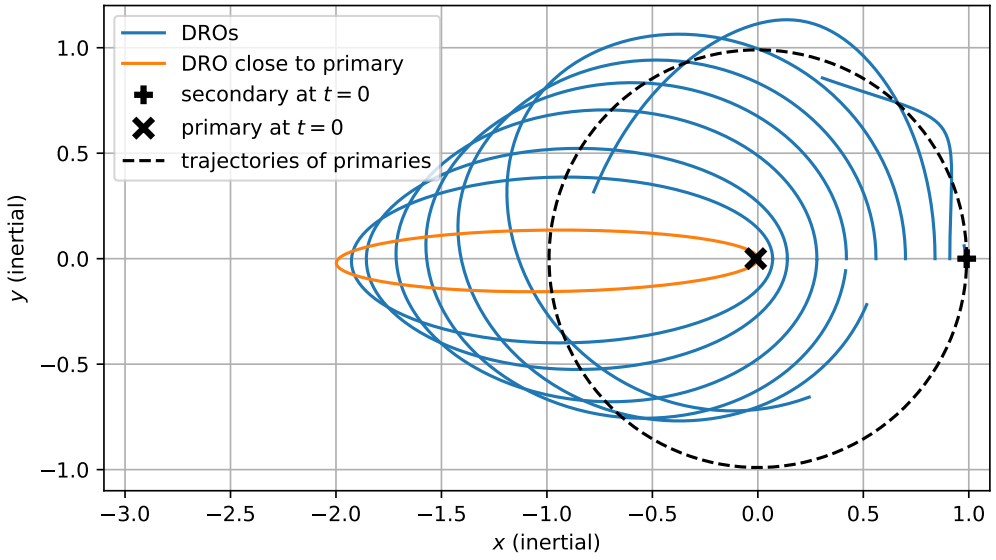

Figure 4.2: Several DROs depicted in an inertial reference frame. The orange DRO starts at $x_0 = 0 = x_1 + 0.01$. Each DRO is shown for exactly one orbit. $\mu = 0.01$.

The method of incremental changes as described in the previous section can take a long time to come to a result for a specific orbit since obtaining an initial value for the initial velocity already requires to compute many orbits. Therefore, a formula that estimates the initial velocity directly is desirable. The estimate needs to be close enough to the true value so that the differential corrector method actually converges to the initial conditions of DROs.

If the orbit is *close* to the secondary, the initial velocity $\dot{y}_0$ can be estimated with assuming an unperturbed circular orbit around the secondary. According to [50, Equation (6.18)], the velocity V_c on a circular orbit is:

$$V_c = \sqrt{\frac{Gm}{r}} \tag{4.1}$$

With the mass m of the secondary being μ, the gravitational constant G being 1 and the distance r to the secondary being $1-\mu-x_0$ (only locations left of the secondary are regarded), the initial velocity $\dot{y}_0$ close to the secondary can be approximated with:

$$\dot{y}_0 \approx \sqrt{\frac{\mu}{1-\mu-x_0}} \tag{4.2}$$

A similar approach yields an approximation for the initial velocity $\dot{y}_0$ of DROs that are close to the primary. But here, the limiting case is not a circular orbit, but a highly eccentric one. The semi-major axis a of this orbit is 1. This can be seen in Figure 4.2, which depicts some DROs in an inertial reference frame. The closer the starting location gets to the primary, the closer the eccentricity of the DRO gets to 1 while also the semi-major axis approaches 1 (dimensionless CR3BP unit). Then, the *vis-viva* equation [50, Equation (6.21)] can give an indication of the velocity V:

$$V^2 = Gm\left(\frac{2}{r}-\frac{1}{a}\right) \tag{4.3}$$

This time, the mass m of the central body is the mass of the primary, which is $1-\mu$. The distance r to the primary is $x_0+\mu$. Therefore, the velocity V calculates to:

$$V = \sqrt{(1-\mu)\left(\frac{2}{x_0+\mu}-1\right)} = \sqrt{2\cdot\frac{1-\mu}{x_0+\mu}-(1-\mu)} \tag{4.4}$$

This has to be compensated by the intrinsic rotation that the CR3BP already has: The relative motion of a fixed point on the x-axis (on the right-hand side of the primary) is equal to the distance to the primary (which is $x_0+\mu$), since the rotational velocity of the CR3BP is 1. The relative motion is pointing in positive y-direction, which is also the direction in which the DRO is being started. Therefore, $x_0+\mu$ needs to be subtracted from Equation (4.4) in order to obtain a good estimate of the initial velocity $\dot{y}_0$ close to the primary:

$$\dot{y}_0 \approx \sqrt{2\cdot\frac{1-\mu}{x_0+\mu}-(1-\mu)}-(x_0+\mu) \tag{4.5}$$

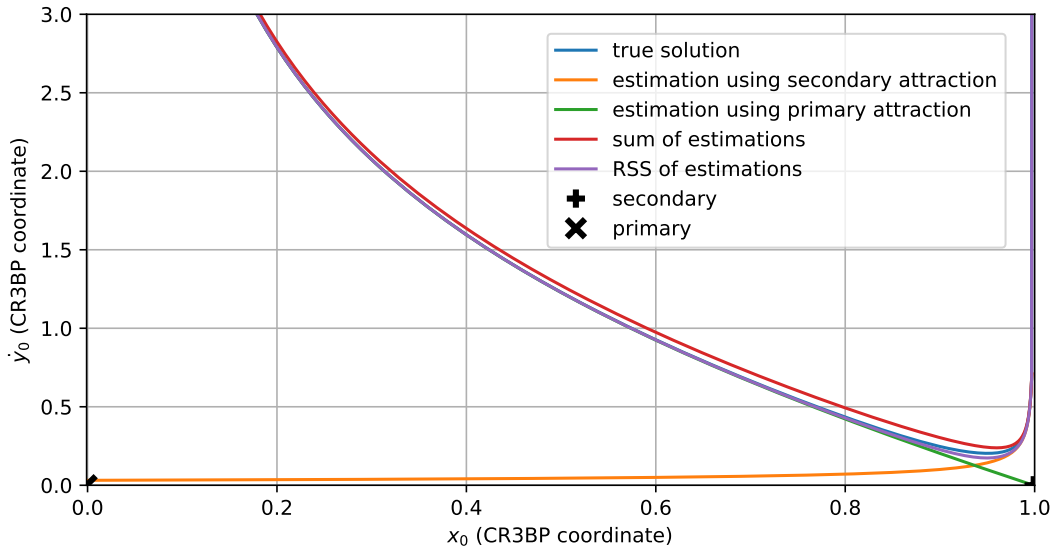

Figure 4.3: Initial velocities $\dot{y}_0$ for DROs depending on their initial position x_0 in the CR3BP with mass ratio $\mu = 0.001$. The true value (blue) is displayed as well as an estimate using the attraction of the secondary, an estimate using the attraction of the primary, their sum, and their RSS.

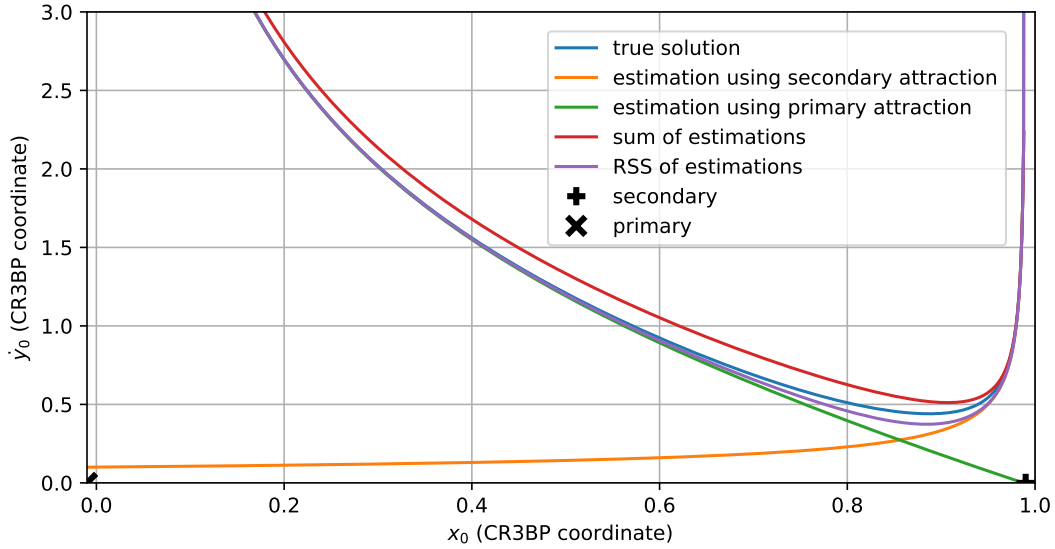

Figure 4.4: Initial velocities $\dot{y}_0$ for DROs depending on their initial position x_0 in the CR3BP with mass ratio $\mu = 0.01$. The true value (blue) is displayed as well as an estimate using the attraction of the secondary, an estimate using the attraction of the primary, their sum, and their RSS.

Figures 4.3 and 4.4 show the initial velocities for two different mass ratios μ, as well as the estimates from Equations (4.2) and (4.5). It can be seen that close to the secondary Equation (4.2) seems to be a good estimate for the true value of the initial velocity $\dot{y}_0$ – as expected – and close to the primary Equation (4.5) seems to be a good estimate – again, as expected. At the location where the two estimates cross, which is at about $x_0 = 0.9$, the true value is higher than the two estimates. Furthermore, the estimate that takes the secondary gravity into account results in a very low estimated initial velocity close to the primary, and vice versa. This immediately suggests to add the two estimates in order to obtain an even better estimate that is valid for every DRO, not only the ones close to the primary or close to the secondary. This sum can also be found in Figures 4.3 and 4.4.

The question that arises now, is if this sum is a good initial guess for the differential corrector algorithm. This has been tested with a CR3BP with mass ratio $\mu = 0.01$. As Figures 4.5 and 4.6 show, not even half of the initial positions x_0 result in a DRO, with the most deviations occurring in two zones: between $x_0 \approx 0.5$ and $x_0 \approx 0.8$ and for x_0-values below 0.2. For x_0-values that are between 0.5 and 0.8, Figure 4.4 shows that indeed the sum of the estimates for the initial velocity $\dot{y}_0$ is a bit higher than the true value. Furthermore, the estimate using the secondary attraction does not go down to zero close to the primary, which seems to be the reason for the differential corrector not to converge to a DRO close to the primary. A more detailed analysis of when the algorithm using the sum of the estimates converges to a DRO can be found in Figure 4.7. Here, the resulting orbit family depending on starting position x_0 and mass ratio μ is shown. It can be seen that for $\mu < 0.001$ all resulting orbits are DROs. The larger the mass ratio μ increases above 0.001, the more starting positions x_0 do not result into a DRO. Furthermore, it can be seen that the non-DRO orbits arise mainly in two regions of the starting position x_0: very close to the primary and at $x_0 < 0.8$. The reasons are the same as before: Close to the primary and for x_0 being a bit smaller than 0.8, the sum of the estimates for the initial velocity $\dot{v}_0$ and its true solution do not coincide very well.

A note about Figures 4.5 and 4.6 shall be made: The “other repeating orbits” seem to have a very interesting shape heavily influenced by the secondary when in reality they are just elliptical orbits around the primary that experience very little influence from the secondary. Their pericenter can be seen twice in Figures 4.5 and 4.6: on the x-axis on the secondary facing side and on the x-axis on the opposing side. If the elliptical orbit were to experience no perturbation from the secondary, the pericenter would be at the same location every orbit in an inertial reference frame. It being on the other side of the secondary implies that the secondary has performed half a revolution in the meantime, for which it takes

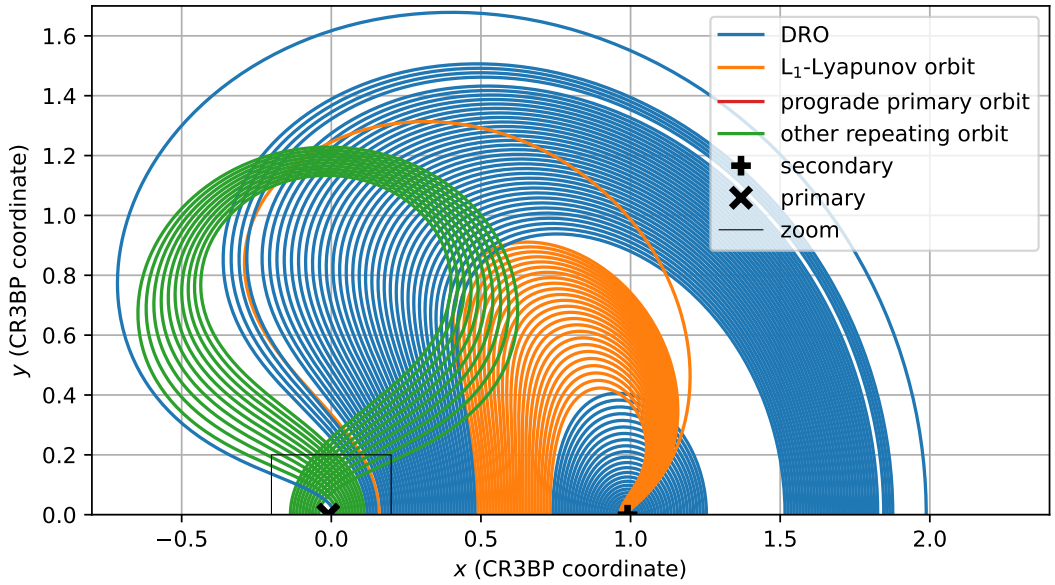

Figure 4.5: Resulting orbits from the differential corrector method with using the sum of the estimates for the initial velocity that are based on primary and secondary attraction respectively as a starting point. $\mu = 0.01$.

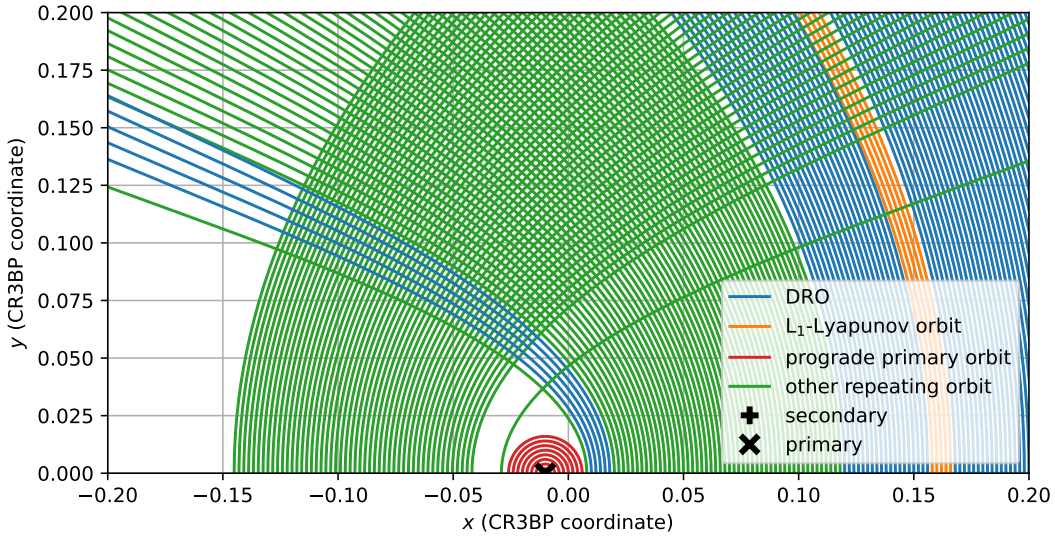

Figure 4.6: Zoom into Figure 4.5.

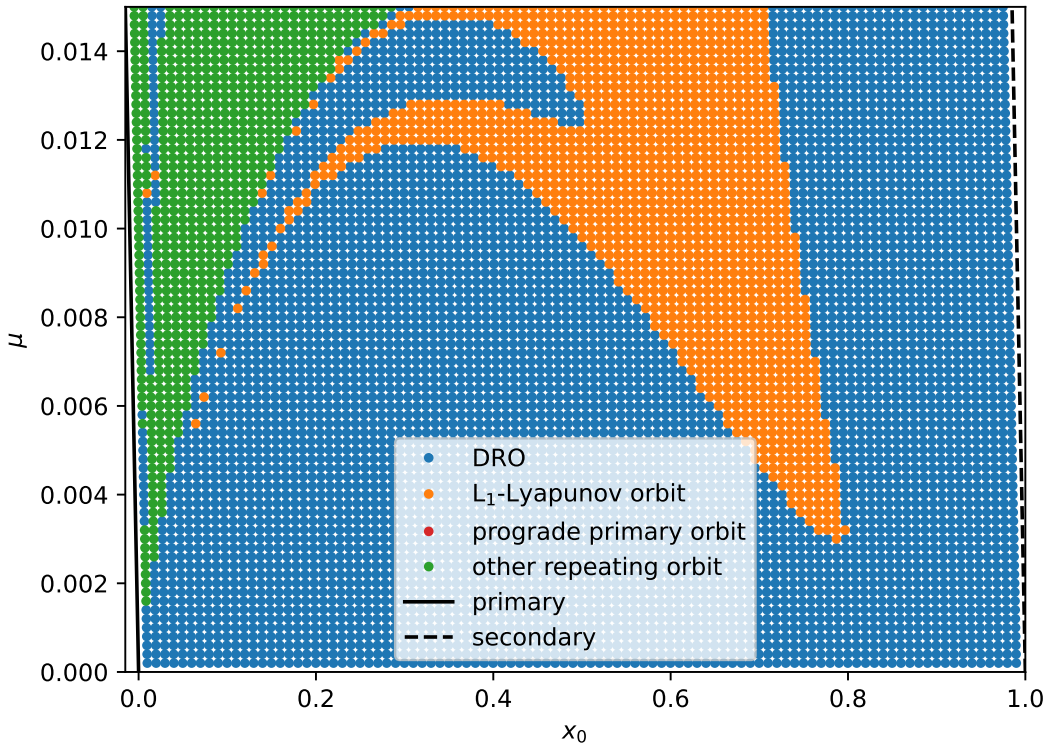

Figure 4.7: Orbit type that is obtained with applying the differential corrector to the sum of the estimates (Equation (4.2) + Equation (4.5)) with different mass ratios μ.

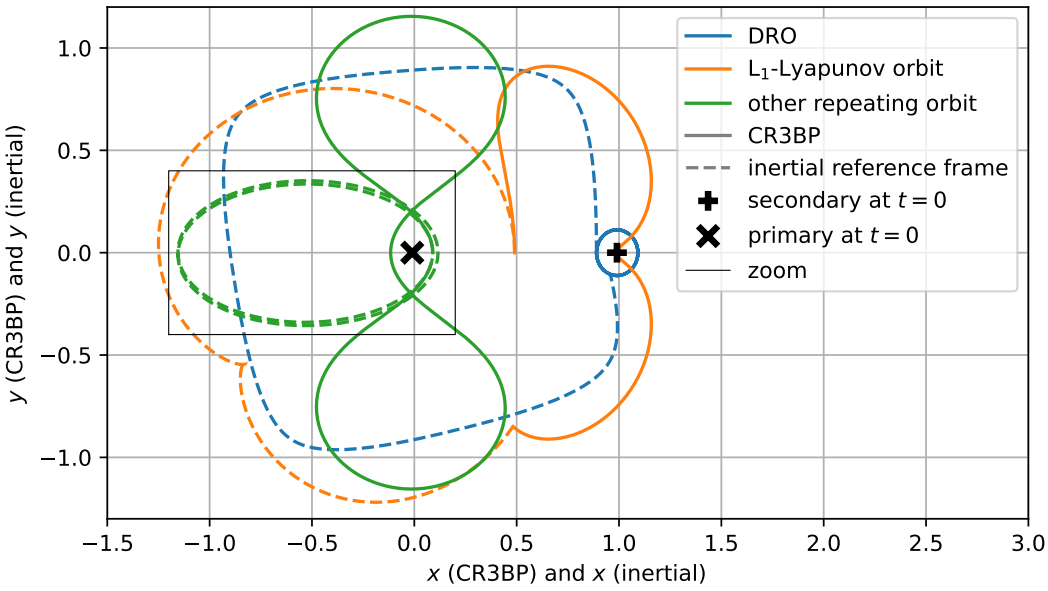

Figure 4.8: DRO, L_1-Lyapunov orbit, and another repeating orbit in the CR3BP in both, the co-rotating reference frame (CR3BP) (solid lines) and an inertial reference frame (dashed lines). The orbits in the rotating reference frame have been propagated until time $t = 2\pi$. Primary and secondary are depicted at their locations at $t = 0$ only. $\mu = 0.01$.

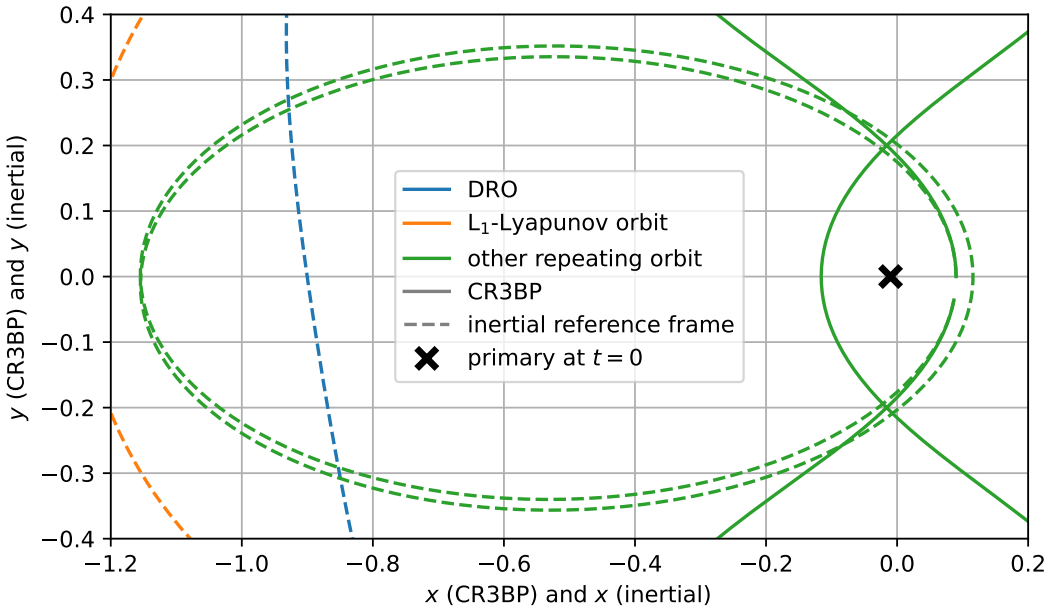

Figure 4.9: Zoom into Figure 4.8.

exactly the time π. Therefore, the green orbits are expected to have a period that is close to π (close and not exactly because there *is* a perturbation from the secondary). One DRO, one L_1-Lyapunov orbit and one of those "other repeating orbits" are illustrated in Figures 4.8 and 4.9 in an inertial reference frame. The propagation time is 2π, within this time the "other repeating orbit" performs only slightly less than two orbits, confirming the reflections on the period of this orbit. In Figure 4.9 it seems like the first and the second orbit have slightly different dimensions in positive x- and positive and negative y-direction. This is due to the fact that the inertial coordinate frame is centered at the barycenter of primary and secondary. The primary – alias the focal point of the ellipse – is moving on a circle around the barycenter, which makes the ellipse seem to *shift*.

Both of these problems mentioned before – the bad $\dot{y}_0$ initial guesses for very low x_0 values and those close to $x_0 \approx 0.8$ – can be lessened by using the root sum squared (RSS) of the two estimates rather than their sum. The RSS is closer to the maximum of the two values than the sum of the two values. Since close to the primary and close to the secondary the respective estimates are already quite good, it is desired that this value is not altered too much by the other estimate. Also, in between primary and secondary the true value of the initial velocity $\dot{y}_0$ is estimated better. All of this can be seen clearly in Figure 4.4. The formula for the RSS estimate is:

$$\begin{aligned}\dot{y}_0 &\approx \sqrt{\sqrt{\frac{\mu}{1-\mu-x_0}}^2 + \left(\sqrt{2\cdot\frac{1-\mu}{x_0+\mu} - (1-\mu)} - (x_0+\mu)\right)^2} \\ &= \sqrt{\frac{\mu}{1-\mu-x_0} + \left(\sqrt{2\cdot\frac{1-\mu}{x_0+\mu} - (1-\mu)} - (x_0+\mu)\right)^2}\end{aligned} \tag{4.6}$$

This estimate can be seen in Figures 4.3 and 4.4. It shall be tested if this estimate yields DROs reliably. This is tested with $\mu = 0.01$. The result can be seen in Figure 4.10. In order to get a better overview about the mass ratios μ that work with this new initial velocity guess, Figure 4.11 shows to which orbits the RSS approach leads. It can be seen that for $\mu < 0.1$ the approach reliably yields DROs.

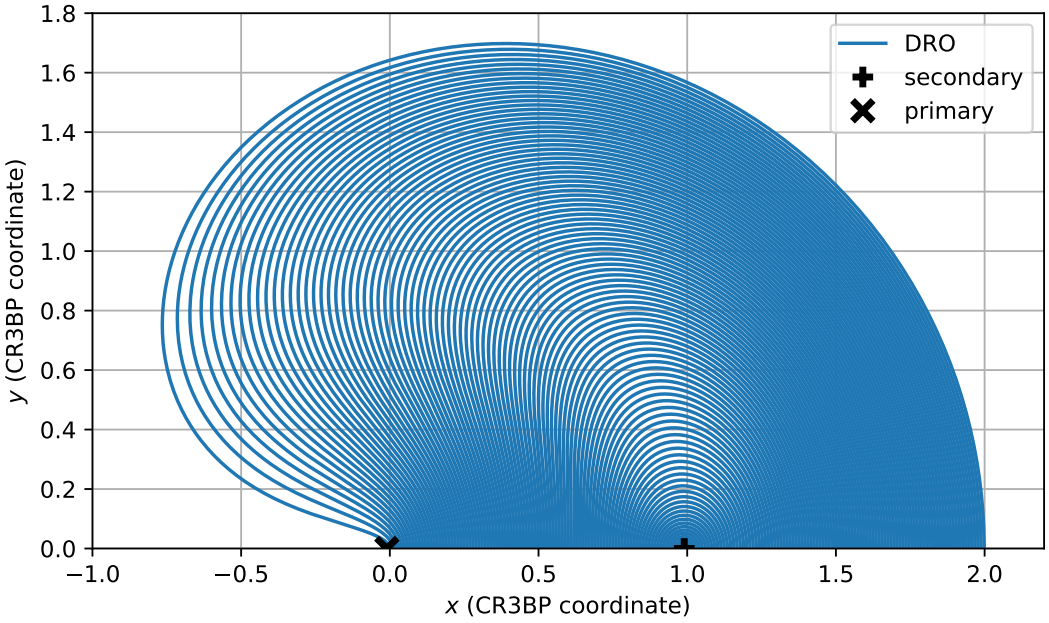

Figure 4.10: DROs obtained with applying the differential corrector to the RSS of the estimates (Equation (4.6)). $\mu = 0.01$.

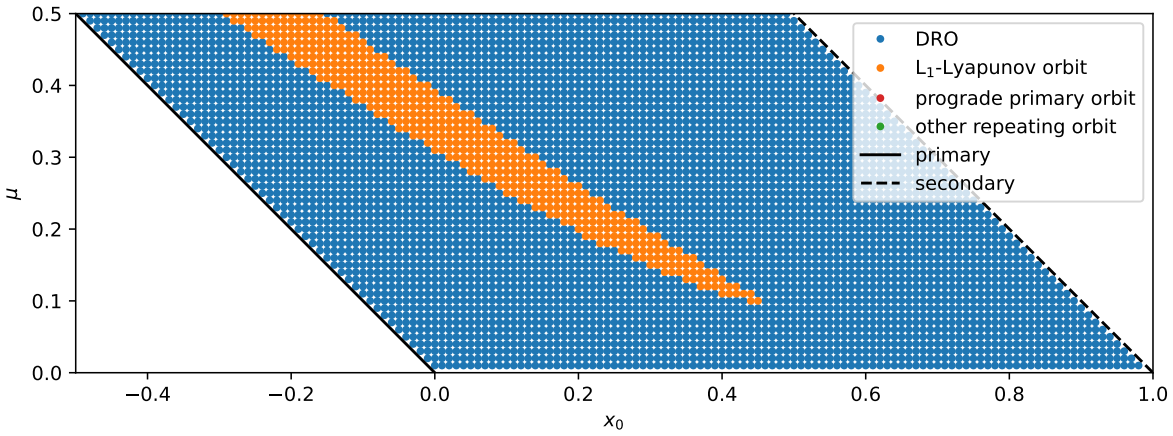

Figure 4.11: Orbit type that is obtained with applying the differential corrector to the RSS of the estimates (Equation (4.6)) with different mass ratios μ.

4.3. Modifying Root Sum Squared

In order to get rid of the few DROs whose initial velocity can not be calculated with the RSS method (see Figure 4.11), the method shall be slightly modified. Figure 4.11 shows that the problems arise approximately in the middle between primary and secondary (and for higher mass ratios μ closer to the primary). Figures 4.3 and 4.4 show that the RSS estimate for the initial velocity is too low (in general, and especially in the region where convergence to DROs is not reached). Therefore, a possible solution would be to multiply the RSS approximation by a factor f. This makes the estimate for $\dot{y}_0$:

$$\dot{y}_0 \approx f \cdot \sqrt{\frac{\mu}{1-\mu-x_0} + \left(\sqrt{2 \cdot \frac{1-\mu}{x_0+\mu} - (1-\mu)} - (x_0+\mu)\right)^2} \tag{4.7}$$

Applying the differential corrector to this initial guess will be called modified root sum squared (MRSS) in the following.

Figures 4.12 to 4.16 show for different values of f if the unmodified RSS method or the MRSS method yields a DRO. In case both of them lead to DROs, the figures indicate which of them converges with a

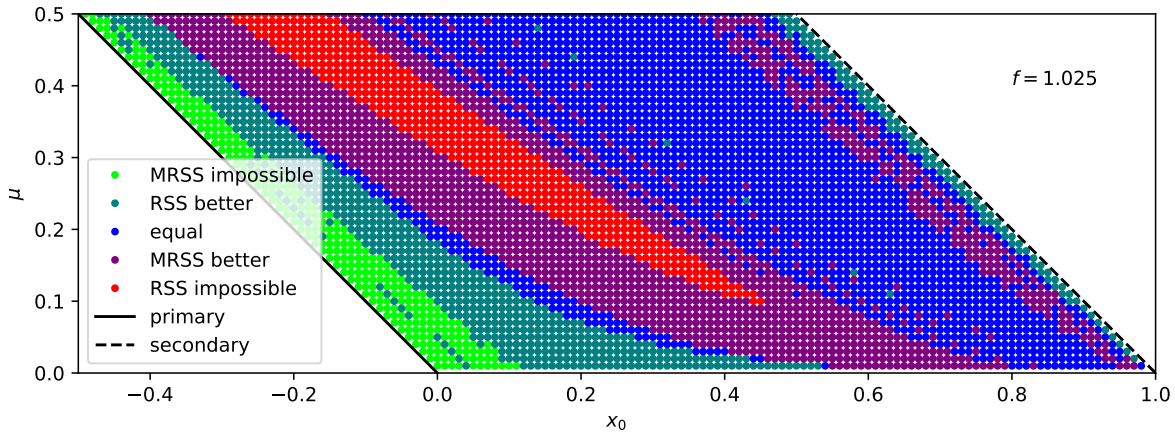

Figure 4.12: Comparison in which cases only RSS (light green) and only MRSS (red) yield a DRO. If both lead to a DRO, the color indicates if RSS needs less iterations (dark green), MRSS needs less iterations (purple), or both need the same number of iterations (blue). Black indicates that neither RSS nor MRSS yield a DRO. $f = 1.025$.

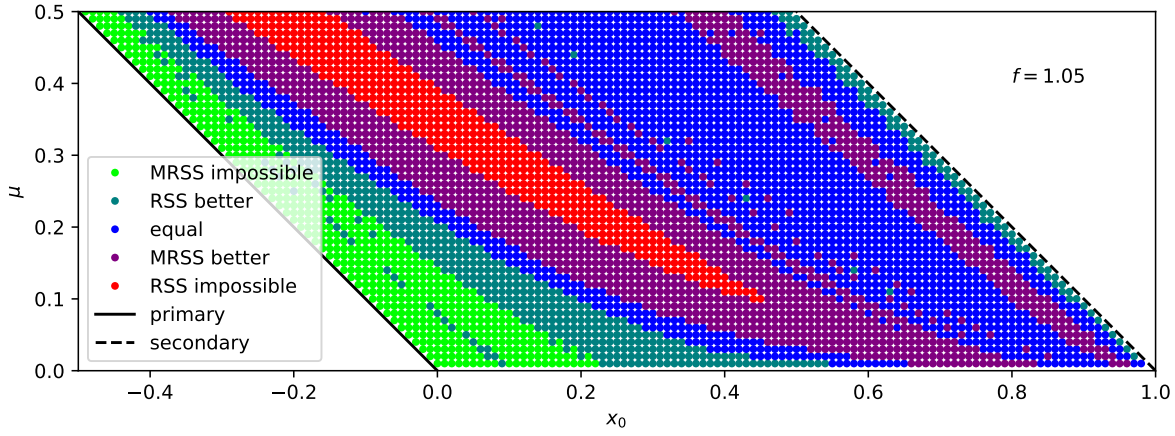

Figure 4.13: Comparison in which cases only RSS (light green) and only MRSS (red) yield a DRO. If both lead to a DRO, the color indicates if RSS needs less iterations (dark green), MRSS needs less iterations (purple), or both need the same number of iterations (blue). Black indicates that neither RSS nor MRSS yield a DRO. $f = 1.05$.

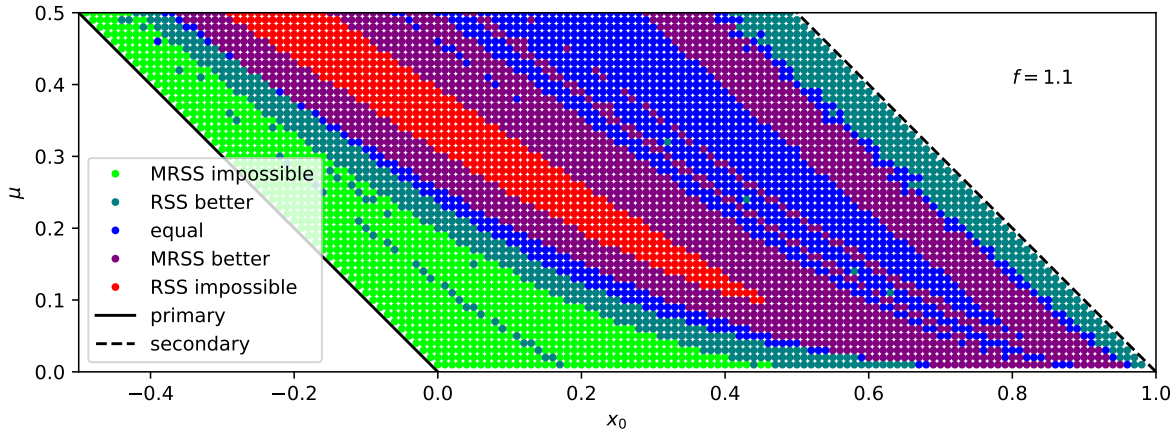

Figure 4.14: Comparison in which cases only RSS (light green) and only MRSS (red) yield a DRO. If both lead to a DRO, the color indicates if RSS needs less iterations (dark green), MRSS needs less iterations (purple), or both need the same number of iterations (blue). Black indicates that neither RSS nor MRSS yield a DRO. $f = 1.1$.

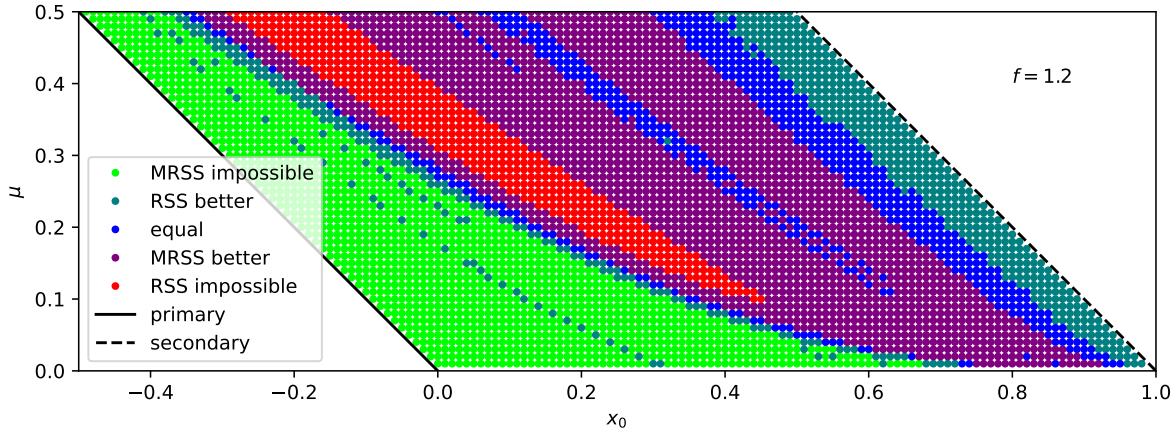

Figure 4.15: Comparison in which cases only RSS (light green) and only MRSS (red) yield a DRO. If both lead to a DRO, the color indicates if RSS needs less iterations (dark green), MRSS needs less iterations (purple), or both need the same number of iterations (blue). Black indicates that neither RSS nor MRSS yield a DRO. $f = 1.2$.

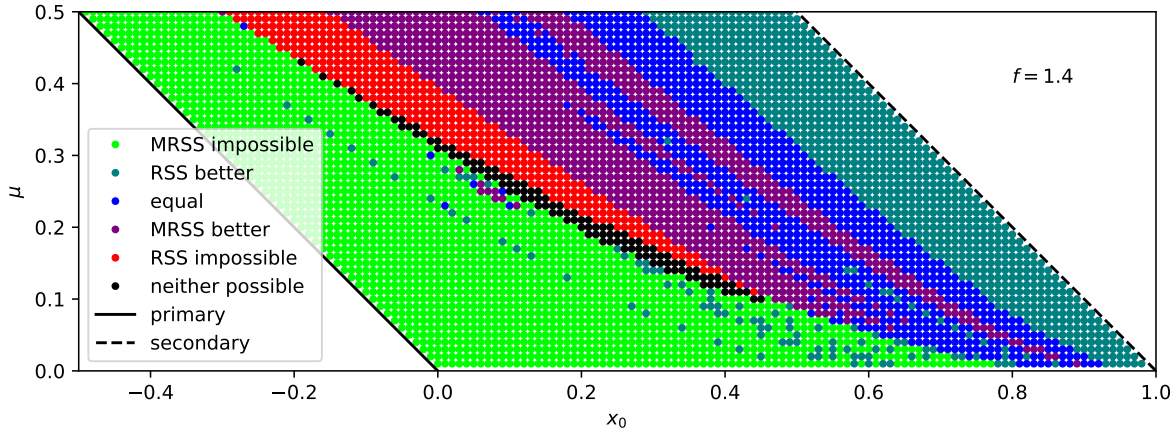

Figure 4.16: Comparison in which cases only RSS (light green) and only MRSS (red) yield a DRO. If both lead to a DRO, the color indicates if RSS needs less iterations (dark green), MRSS needs less iterations (purple), or both need the same number of iterations (blue). Black indicates that neither RSS nor MRSS yield a DRO. $f = 1.4$.

smaller number of iterations needed. The goal would now be to find a factor f that leads to a non-DRO region that has no common points with the RSS non-DRO region. In this case, a condition could be set up that decides in which cases RSS and in which cases MRSS should be used, with having a solution for any possible combination of mass ratio μ and starting position x_0. Of the five factors f that are depicted in Figures 4.12 to 4.16, only $f = 1.4$ in Figure 4.16 leads to DROs that can not be computed with either method, since all other figures do not show any black dots. Furthermore, it can be observed that the light green area – indicating that the new MRSS method does not yield a DRO – is extending more and more to the right (higher x_0-values) with increasing factor f. This suggests that factors f that are higher than 1.4 are not successful either since the light green area will extend further and further into the red area, increasing the size of the black area even more. Therefore, a decision has to be made between the remaining factors $f = 1.025, 1.05, 1.1, 1.2$. Of course any number in between could be tried as well but for the sake of eliminating the non-DRO region this is not necessary.

For this decision, another criterion is needed. For that it is crucial to stress the meaning of the purple area: It represents all possible combinations of mass ratio μ and starting position x_0 at which the MRSS method performs better in terms of the number of iterations than the RSS method. The use of the number of iterations as a measure of *how fast* a method converges to a DRO is discussed in Section 4.4. A larger purple area therefore means that for a larger fraction of the possible DROs the number of iterations needed can be decreased, and is therefore to be sought. $f = 1.2$ in Figure 4.15 shows the largest purple area but the light green and the red area are *dangerously close* to each other, which makes it harder to define a simple border that fits in between them. Since the criterion with the size of the purple area is only a secondary criterion, in this case $f = 1.1$ is chosen, which still has a large purple area. Here, it is easily possible to define in which cases RSS and in which cases MRSS should be used. While in the blue area it does not matter, it would be beneficial if the entire purple area used MRSS and the dark green area used RSS. On the other hand it is compulsory that the entire red area uses MRSS and the entire light green area uses RSS.

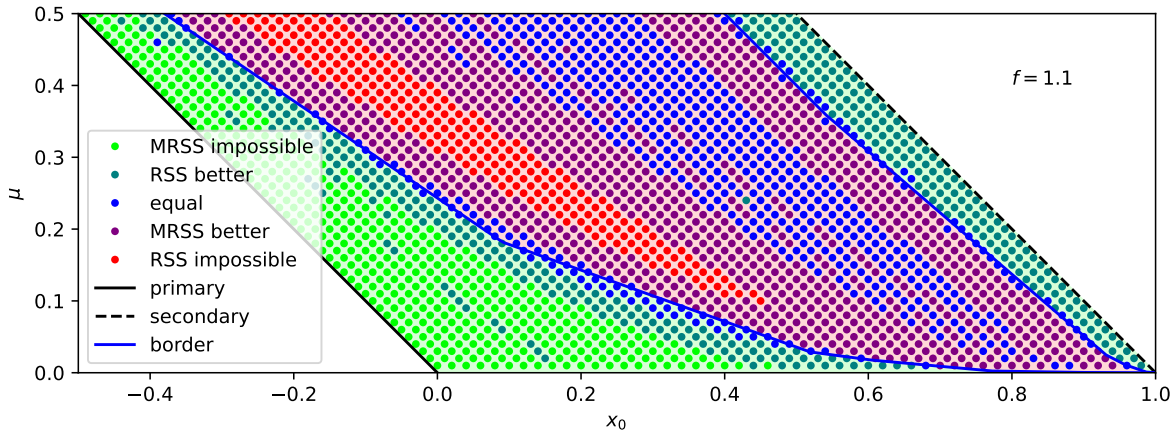

Figure 4.17: Comparison in which cases only RSS (light green) and only MRSS (red) yield a DRO. If both lead to a DRO, the color indicates if RSS needs less iterations (dark green), MRSS needs less iterations (purple), or both need the same number of iterations (blue). The border (solid blue line) divides regions where RSS is recommended (green shaded background) and regions in which MRSS is recommended (red shaded background). $f = 1.1$.

Figure 4.17 shows in which regions it is recommended to use the MRSS method (red background) instead of the RSS method (green background). More details for the low mass ratio μ region can be seen in Figures 4.18 and A.1 to A.4. The region with the blue dots allows the border to be rather imprecise, since for the blue dots it does not matter on which side of the border they end up, since they indicate that RSS and MRSS perform equally well. Therefore, the easiest approach for defining the border between RSS and MRSS is to use a piecewise linear function of μ. As a result, the left and right borders $a(\mu)$ and $b(\mu)$ could be as follows:

$$a(\mu) = \begin{cases} 0.36 - 1.48\mu & \text{for} \quad 2/11 < \mu \\ 0.6 - 2.8\ \mu & \text{for} \quad 14/487 < \mu \leq 2/11 \\ 0.74 - 7.67\mu & \text{for} \quad 2/121 < \mu \leq 14/487 \\ 0.8 - 11.3\ \mu & \text{for} \quad 1/490 < \mu \leq 2/121 \\ 0.93 - 75\ \mu & \text{for} \quad 1/10625 < \mu \leq 1/490 \\ 0.97 - 500\ \mu & \text{for} \quad 1/112500 < \mu \leq 1/10625 \\ 0.99 - 2750\ \mu & \text{for} \quad 1/2225000 < \mu \leq 1/112500 \\ 1 - 25000\ \mu & \text{for} \quad \mu \leq 1/2225000 \end{cases} \tag{4.8}$$

$$b(\mu) = \begin{cases} 0.9 - 1\ \mu & \text{for} \quad 60/167 < \mu \\ 0.96 - 1.167\mu & \text{for} \quad 20/833 < \mu \leq 60/167 \\ 0.98 - 2\ \mu & \text{for} \quad 1/100 < \mu \leq 20/833 \\ 0.99 - 3\ \mu & \text{for} \quad 1/1700 < \mu \leq 1/100 \\ 1 - 20\ \mu & \text{for} \quad \mu \leq 1/1700 \end{cases} \tag{4.9}$$

The estimate for the initial velocity $\dot{x}_0$ is then:

$$\dot{y}_0 \approx f \cdot \sqrt{\frac{\mu}{1-\mu-x_0} + \left(\sqrt{2 \cdot \frac{1-\mu}{x_0+\mu} - (1-\mu)} - (x_0+\mu)\right)^2} \tag{4.10}$$

with f being:

$$f = \begin{cases} 1.1 & \text{for } a(\mu) < x_0 < b(\mu) \\ 1 & \text{else} \end{cases} \tag{4.11}$$

In Figures 4.17 and 4.18, there are in total zero red dots in the green area and three green dots in the red area. Another green dot in the red area can be found in Figure A.2. This means that out of the $82\,500$ combinations of starting position x_0 and mass ratio μ that have been evaluated in Figures 4.17, 4.18 and A.1 to A.4, four lead to the use of the less optimal technique, while no combination leads to the use of a technique that is not applicable because it does not result in a DRO. This means that the combined method (CM) defined by Equations (4.8) to (4.11) always yields a DRO and does so in the very most cases with fewer iterations needed than the RSS method. Therefore it is to be preferred and will be applied in the rest of this thesis for finding initial conditions of DROs.

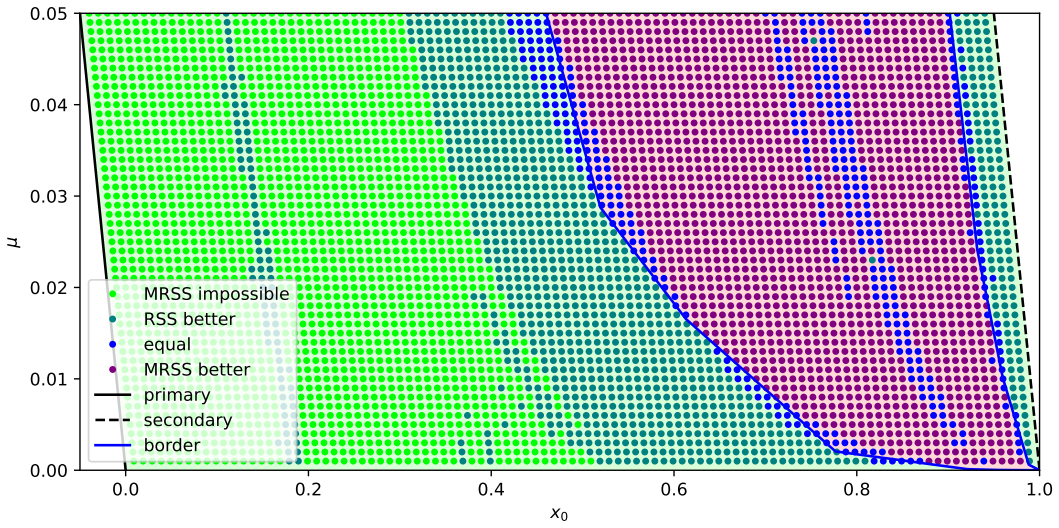

Figure 4.18: Zoom into Figure 4.17.

4.4. Quantifying the Combined Method Enhancement

It needs to be evaluated if the new CM yields the initial conditions for a DRO at a specific starting location x_0 *faster* than the method of incremental changes. *Faster* in this context can refer to different criteria such as computation time, propagation time, or number of iterations. Computation time typically depends on the machine that runs the simulation. Propagation time refers to the amount of time that is covered by the simulation(s). Having the propagation time as a criterion would not take into account that in regions of large acceleration more computational effort – and thus more computation time – is needed for the same amount of propagation time. Therefore – and for the sake of simplicity – the number of iterations is taken as an indication for *how fast* a method converges. It should be noted, that DROs close to the primary have a longer propagation time and therefore tend to require more computation time than DROs that are close to the secondary. Furthermore, orbits that are close to the secondary or the primary tend to require more computation time than DROs that are in between because they experience larger accelerations and therefore the local step size of the propagation algorithm will be chosen to be smaller.

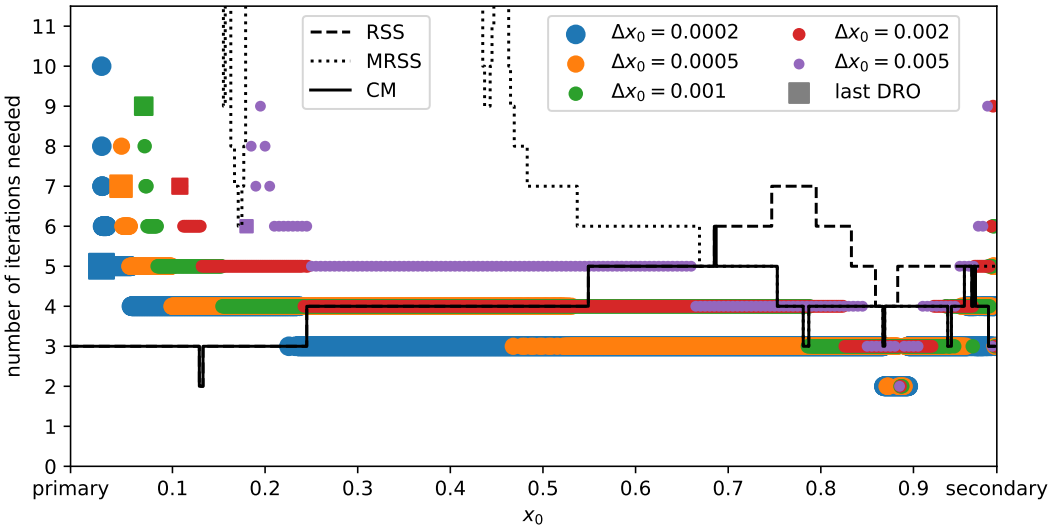

Figure 4.19: Number of iterations that are needed in order for the differential corrector to converge to a DRO. The solid line represents the approach that uses the CM, which is always the optimal out of the RSS method (dashed line) and the MRSS method (dotted line). The colored dots represent the incremental change approach, as described in Section 4.1 with different step sizes for the change Δx_0 in starting position. For some values of x_0, the algorithm yields an orbit different from a DRO, then the last DRO is marked with a square. $\mu = 0.01$. Similar plots for $\mu = 0.1$, $\mu = 0.001$, and $\mu = 3 \cdot 10^{-6}$ can be found in Figures A.5 to A.7.

This all being said, Figure 4.19 compares the number of iterations that is needed for the differential corrector algorithm to converge to a DRO for $\mu = 0.01$. A first thing to notice is that with the differential corrector method, not all of the orbits end up being DROs. Starting at the secondary, the algorithm converges to DROs only up until $x_0 = 0.18$ for $\Delta x = 0.005$, $x_0 = 0.0234$ for $\Delta x = 0.0002$, and start positions x_0 in between for step sizes Δx_0 in between. It is not surprising that a smaller step size yields a lower starting position x_0 that can be reached, since a higher step size leads to a larger difference in starting velocity $\dot{v}_0$ and therefore convergence is harder to reach.

Regarding the number of iterations that are needed for the algorithm to converge to a DRO, it can not be stressed enough that with the RSS method only the exact number of iterations that is depicted in Figure 4.19 for a specific starting position x_0 is needed in order to obtain a DRO. For example for $x_0 = 0.6$, five propagated orbits are needed for convergence. On the other hand, for the method of incremental changes, all of the numbers that are on the right-hand side of the target position x_0 have to be summed up in order to obtain the number of iterations that is needed to obtain a DRO. Figure 4.20 shows the cumulated number of iterations. It can clearly be seen that the CM performs significantly better than the method of incremental changes in terms of total computational effort. Although of course

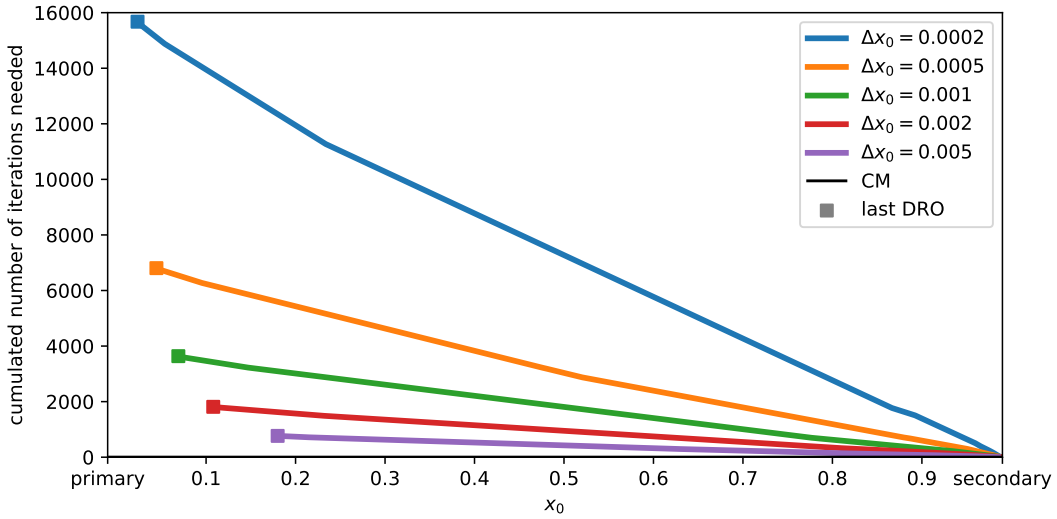

Figure 4.20: Number of iterations that are needed in order for the differential corrector to converge to a DRO. The solid line represents the approach that uses the RSS of the two estimates as initial guess (Equation (4.6)). The dots represents the incremental change approach, as described in Section 4.1 with different step sizes for the change Δx_0 in starting position. With some of the step sizes the algorithm yields an orbit different from a DRO, in this case the last DRO is marked with a square. $\mu = 0.01$.

it should be noted that this holds true if one specific DRO should be computed. If the entire orbit family is needed then the numbers need to be summed up also for the CM.

The shape of the curves from Figure 4.19 shall be discussed here. The line for the RSS method has a maximum for $x_0 \approx 0.77$. This matches approximately the findings from Figure 4.4: The largest difference between the true solution and the RSS can be found between $x_0 \approx 0.7$ and $x_0 \approx 0.95$. It can be assumed that the comparably large number of iterations needed in this region is due to the large gap between the initial guess for the initial velocity $\dot{y}_0$ and its true solution and that the low numbers of iterations needed close to primary and secondary are due to their good accordance. For the method of incremental changes on the other hand, the slope of the true solution in Figure 4.4 is decisive for the performance of the algorithm. For regions with a high slope the initial velocity $\dot{y}_0$ changes quickly with x_0 and therefore the initial guess is farther off than for regions with a small slope. And indeed, $\Delta x_0 = 0.002$ and $\Delta x_0 = 0.005$ reach the minimum number of iterations needed at about $x_0 \approx 0.885$ in Figure 4.19 which coincides with a very flat region of the true solution in Figure 4.4.

The relation between RSS, MRSS, and CM fits well to previous findings: As is was also evident from Figure 4.18 (for $\mu = 0.01$), Figure 4.19 shows that RSS needs more iterations than MRSS in the region between $x_0 \approx 0.7$ and $x_0 \approx 0.95$, while it needs less for $x_0 < 0.67$ and $x_0 > 0.97$. Also, MRSS does not yield DROs for $x_0 < 0.46$ with two "islands" where MRSS does yield DROs at $x_0 \approx 0.17$ and $x_0 \approx 0.44$. Indeed, for any starting position x_0, the CM uses the method (RSS or MRSS) that requires less iterations.

Figures A.5 to A.7 show the number of iterations that are needed for $\mu = 0.1$, $\mu = 0.001$, and $\mu = 3 \cdot 10^{-6}$, respectively. They show that for lower mass ratios μ the advantage of the CM over the method of incremental changes is even bigger. For example, in Figure A.7 for $\mu = 3 \cdot 10^{-6}$ the CM (and the RSS method) needs only two iterations for most of the starting positions x_0 while the method of incremental changes needs three for most of the starting positions x_0 for the smallest step size $\Delta x_0 = 0.0002$. And of course – as stressed before – this is for only one particular DRO, but the method of incremental changes requires to calculate all steps before that as well.

4.5. Conclusions

In this chapter, the method of incremental changes that was suggested by [17] was analyzed. This uses the initial velocity for a certain DRO as a starting point in order to calculate the initial velocity of a neighboring DRO. This turned out to be quite inefficient as in order to compute a specific DRO, all DROs between the secondary and the desired starting location x_0 have to be computed. With the CM, an algorithm was found that is reliably able to compute an initial velocity that is close enough to the true initial velocity of the desired DRO, such that the differential corrector is able to find the DRO. The CM does not require to compute any additional DROs, which makes it very handy when the initial conditions of a specific DRO are needed.

5

Integrator Settings

Usually in astrodynamics simulations there are two properties that have to be chosen with care as they influence the computation time and the accuracy of the result: the propagator and the integrator. In this specific case, the propagator is already set by the equations of the CR3BP in Chapter 3: the Cowell type. The integrator on the other hand is subject of a thorough investigation: If the step size is chosen to be too large, the error that is made in each of the steps (truncation error) is driving the total error to be large. On the other hand, if the step size is chosen too small, the error that accumulates from all the rounding that happens in each step due to the limited accuracy of floating-point numbers (rounding error) takes over and dominates the total error.

This chapter will first look into different fixed step size Runge-Kutta (RK) methods and evaluate which of them is best in propagating DROs. Then, variable step size RK methods are investigated and their (dis-)advantages for DROs explained. Finally, a conclusion for the further analysis is drawn.

5.1. Fixed Step Size Runge-Kutta Methods

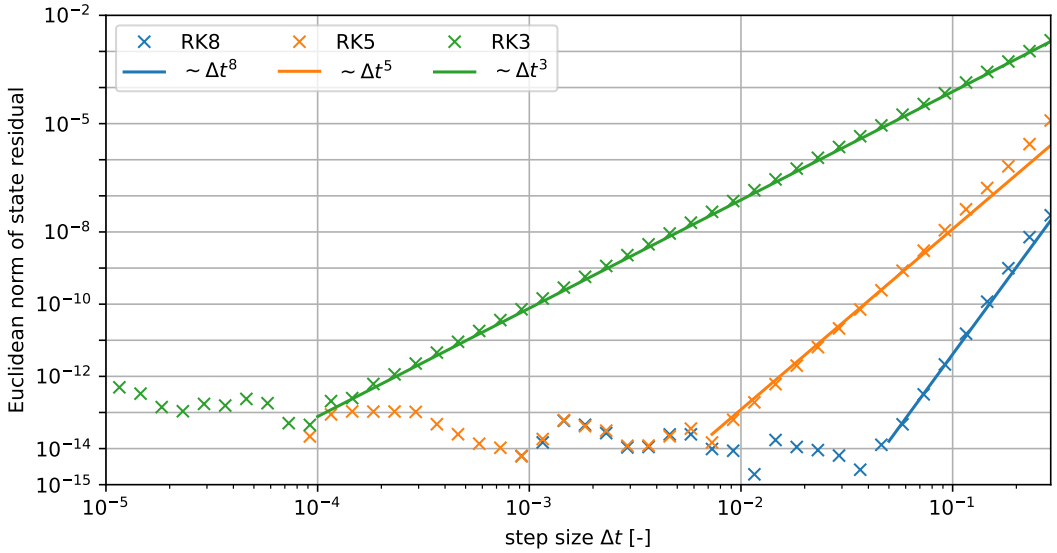

Figure 5.1: The Euclidean norm of the state residual depending on the step size Δt of the integration for various RK methods. $\mu = 0.001$, $x_0 = 0.799$.

Fixed step size RK methods of any order are readily available. The order indicates "how fast" the algorithm converges to the true solution of an ivp. This can be observed in Figure 5.1: The Euclidean

norm of the state residual of the nth degree RK method is proportional to the nth power of the step size Δt in the region that is dominated by the truncation error. In the region that is dominated by the rounding error, the residual stays approximately constant, since the rounding error per step does not depend on the step size Δt. However, as for lower step sizes Δt more steps are needed, the residual gets slightly larger when the step size Δt gets even lower. This trend is overshadowed by the erratic behavior of the rounding error, making it hard to actually identify the slope of this ascend.

The state residual in this case is the difference between the state after half an orbit with the step size Δt and the state after half an orbit with a more accurate step size $\Delta t/1.2$. The factor 1.2 is not too large in order to not let the rounding error distort the results of the simulation that is supposed to be the more accurate one. It is also not too small in order for the two simulations to be visibly different from each other. Therefore, the residual can be seen as an indication of how large the error is that the propagation is making after half an orbit. For this thesis, three RK methods are compared to each other that are all available in the *SciPy* library. They are a third-order RK method, a fifth-order RK method, and an eighth-order RK method. Figure 5.1 shows that with the eighth-order Runge-Kutta method (RK8) the largest steps can be taken while at the same time reaching the lowest Euclidean norm of the state residual.

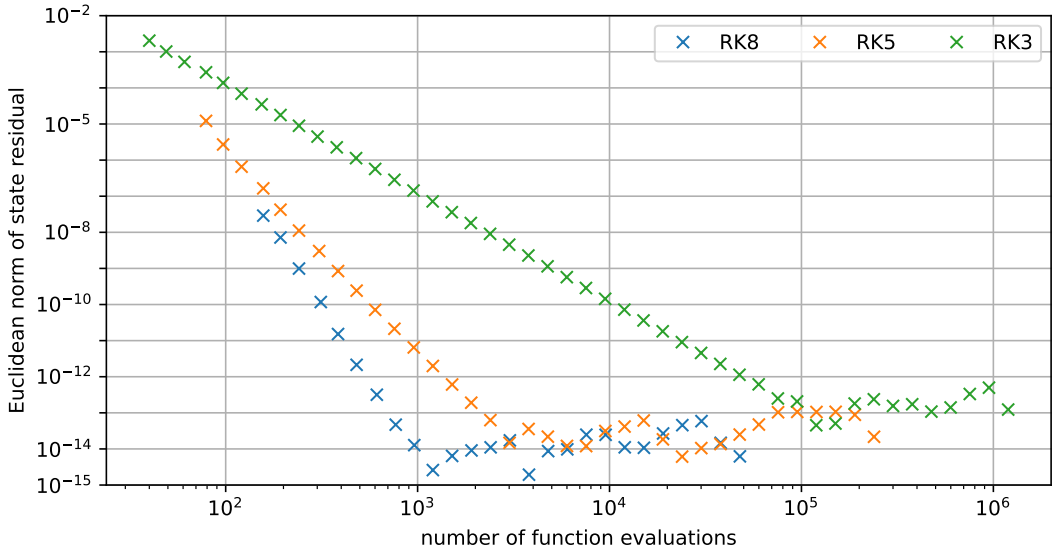

Figure 5.2: The Euclidean norm of the state residual depending on the number of function evaluations for various RK methods. $\mu = 0.001$, $x_0 = 0.799$.

This does not necessarily mean that this is the method that needs to lowest amount of computational effort, since one step in RK8 needs more computational effort than in a lower-order RK method. Therefore, the computational effort is estimated with the number of function evaluations that are needed in total for half an orbit. “Function evaluations” in this case refers to the evaluations of the right-hand side of Equation (3.13). This is depicted in Figure 5.2. It shows that indeed RK8 is the method that needs the least number of function evaluations while at the same time reaching the lowest residual. In Figure 5.1, the step sizes Δt at which the rounding error dominates the total error and the step sizes Δt at which the truncation error does so can clearly be distinguished: For step sizes Δt higher than ≈ 0.04 to 0.05 the residual of RK8 follows closely a function that is proportional to Δt^8 – indicating that this region is dominated by the truncation error. For step sizes Δt lower than ≈ 0.04 to 0.05 the residual of RK8 behaves rather erratic but stays always very close to the minimum – indicating that this region is dominated by the rounding error. The lowest residual can be found at the border between those two regions.

In the following it will be assumed that the RK8 scheme is the optimal one for all possible DROs. The aim would now be to obtain the optimal step size Δt for each of the DROs. Since it is of course not feasible to analyze each of the plots containing the Euclidean norm of the state residual like Figure 5.1

manually, an algorithm needs to be created for that. The easiest solution would be to just take the step size Δt that belongs to the lowest Euclidean norm of the state residual. But this is problematic for two reasons: Firstly, only a finite number of step sizes Δt can be investigated and the best step size Δt might not be represented well in whatever grid one chooses. But more importantly, the region that is dominated by the rounding error shows a rather erratic behavior. In general it does hold that the larger the difference in step size Δt between the optimum and current step size Δt, the higher the residual, but it can not be guaranteed. In order to avoid choosing a step size Δt that is lower than the optimum, the analysis needs to be a bit more elaborate.

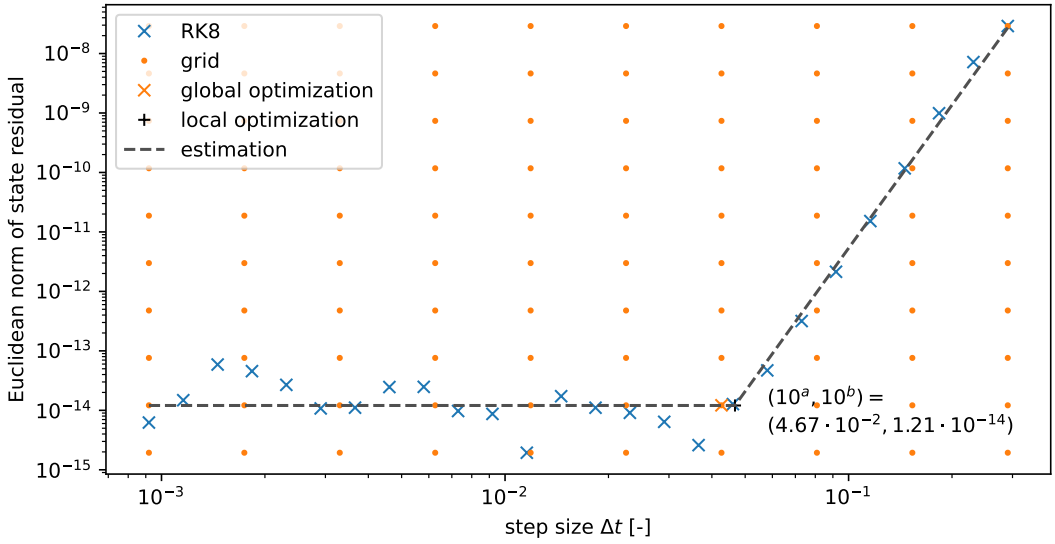

Figure 5.3: The Euclidean norm of the state residual depending on the step size Δt of the RK8 method. Global optimization via grid search and then local optimization via least squares method is performed to find the point between the region dominated by the truncation error and the region dominated by the rounding error. $\mu = 0.001$, $x_0 = 0.799$.

In fact, it turns out to be an optimization problem. For the explanation of the approach, the common logarithm of the step size Δt will be called x and the common logarithm of the Euclidean norm of the state residual will be called f. Then, f follows approximately the function $w_{a,b}(x)$:

$$f \approx w_{a,b}(x), \qquad w_{a,b}(x) = \begin{cases} b & \text{for } x < a \\ b + n \cdot (x - a) & \text{else} \end{cases} \tag{5.1}$$

where n is the degree of the RK method, which in the case of RK8 is 8. The parameters a and b are the coordinates of the point that represents the optimal step size Δt – which can be computed to be 10^a – and the respective residual – which is 10^b. Now the optimization problem is to find a and b such that $f \approx w_{a,b}(x)$ is the best possible approximation. This local optimization can easily be done by a least-squares method. The least-squares method works even more efficiently when being supplied with the Jacobian matrix of $w(x)$, which can be computed with:

$$\frac{\partial w_{a,b}(x)}{\partial a} = \begin{cases} 0 & \text{for } x < a \\ -n & \text{else} \end{cases} \qquad \text{and} \qquad \frac{\partial w_{a,b}(x)}{\partial b} = \begin{cases} 1 & \text{for } x < a \\ 1 & \text{else} \end{cases} = 1 \tag{5.2}$$

In order to be sure that the local optimization yields the global minimum and not only a local minimum, a global optimization shall be applied first. In this case – due to the relative simplicity of the optimization problem – it turns out to be sufficient to apply a grid search algorithm. This can be seen in Figure 5.3: The grid is a ten by ten grid that goes from the minimum to the maximum of the investigated step size Δt and the observed Euclidean norm of the state residual, respectively. The grid is represented by the orange dots, while the orange cross represents the one grid point that is optimal. From there, a local

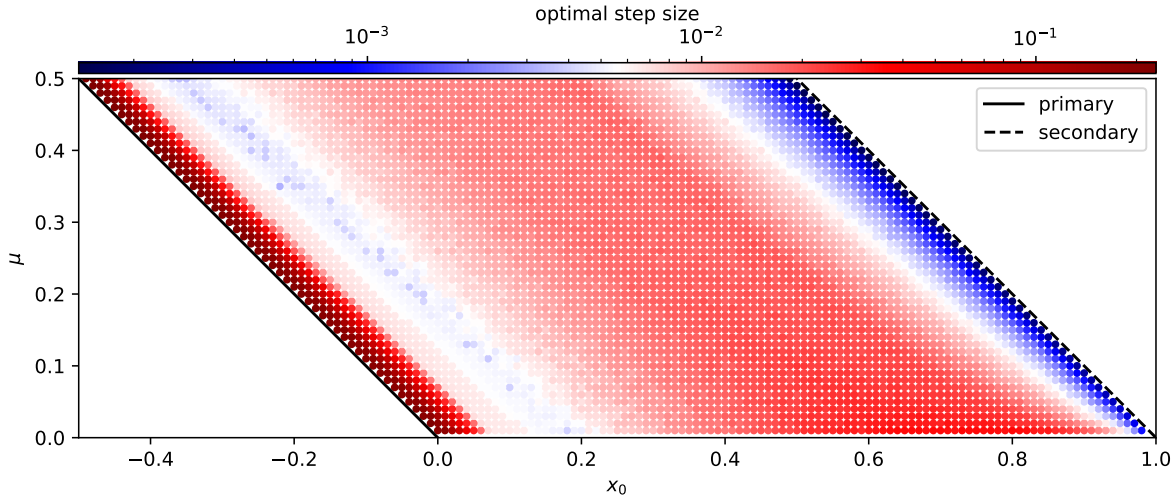

Figure 5.4: Optimal step size Δt depending on the mass ratio μ and the starting position x_0 of the DRO.

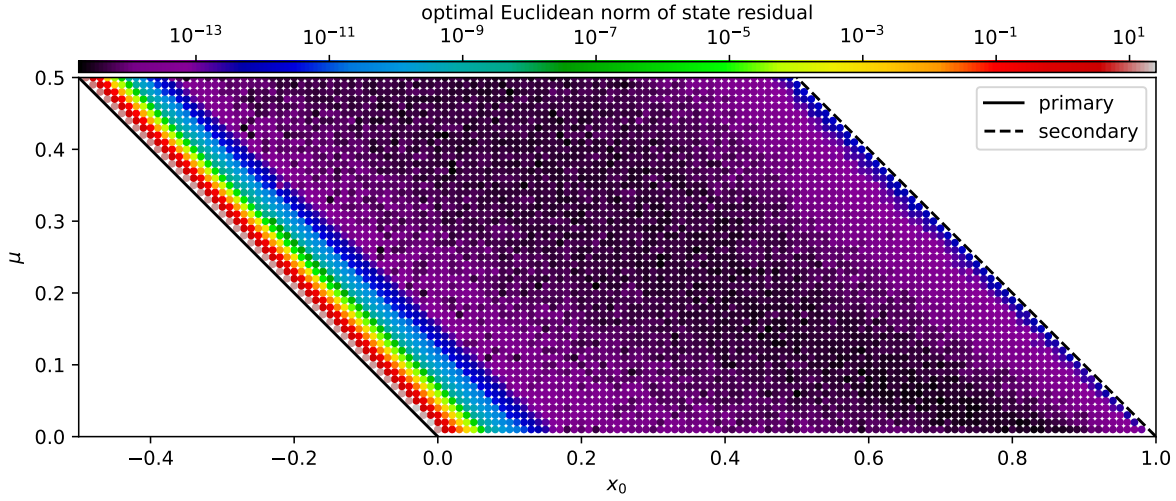

Figure 5.5: Euclidean norm of the state residual when using the optimal step size Δt as depicted in Figure 5.4.

optimization is started that results in the black cross. This procedure is performed in order to obtain the optimal step size depending on the specifics of the DRO, which is discussed in the following.

Figure 5.4 shows the optimal step size for the RK8 scheme depending on the mass ratio μ and the starting position x_0. The respective Euclidean norm of the state residual can be found in Figures 5.5 and 5.6. The optimal step size Δt close to the secondary is low, compared to the other starting positions that are farther away from the secondary. This is expected since the accelerations as well as the changes in acceleration close to the secondary are high. For the same reasoning, the norms of the state residuals for DROs that start close to the secondary are larger than for DROs that start in the middle between primary and secondary. Figure 5.6 suggests that there are even more than two orders of magnitude in between, but regarding the fact that for DROs close to the secondary the norm of the state residual does not exceed 10^{-12}, this is still an acceptable result.

However, the same line of reasoning could be applied to the DRO that start close to the primary, and this is definitely not supported by Figures 5.4 to 5.6: The optimal step size does not decrease when the starting position approaches the primary, but the contrary happens. The norm of the state residual increases – as expected –, but by way more than it should: While this norm rises to about 10^{-12} for

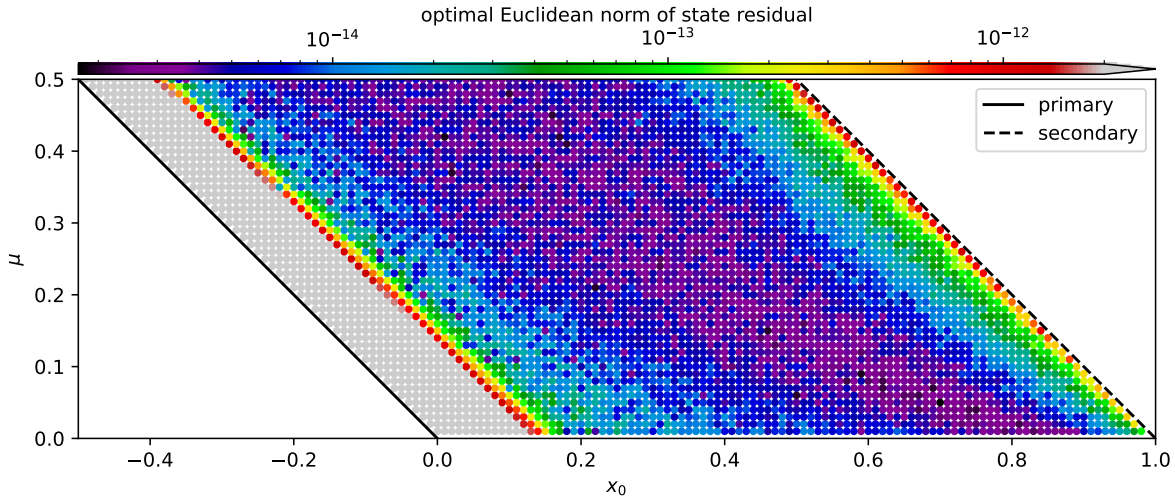

Figure 5.6: Figure 5.5 with adjusted color map.

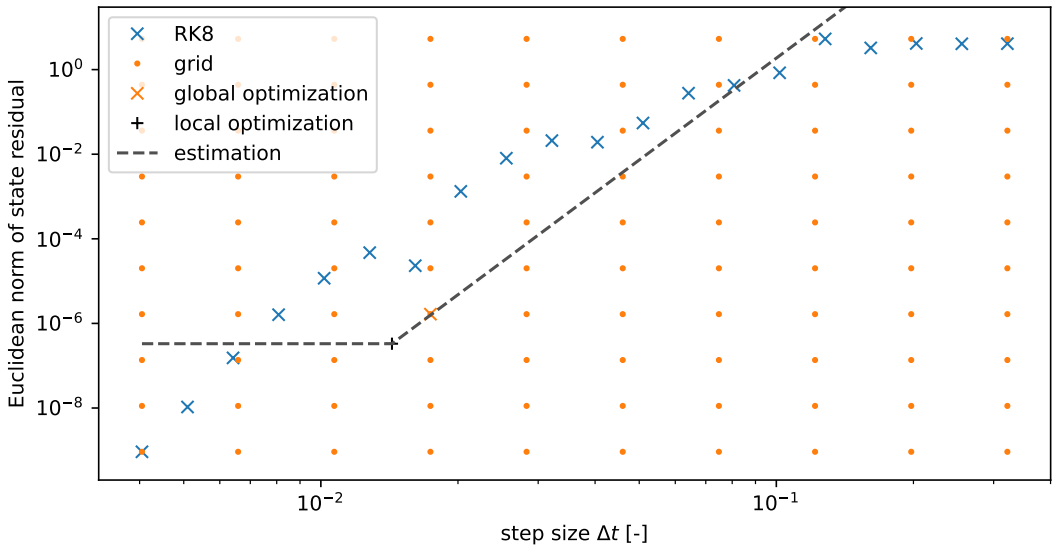

Figure 5.7: The Euclidean norm of the state residual depending on the step size Δt of the RK8 method. Global optimization via grid search and then local optimization via least squares method is performed to find the point between the region dominated by the truncation error and the region dominated by the rounding error. $\mu = 0.1$, $x_0 = -0.03$.

DROs close to the secondary, it rises to 10^1 for DROs close to the primary. This residual can clearly not be accepted.

To understand why the (supposedly) optimal step size increases when the starting position approaches the primary, the previously described optimization algorithm shall be investigated. This is done exemplary for the case of $\mu = 0.1$ and $x_0 = -0.3$, which is in the region of DROs for which a lower step size Δt should be expected. This can be seen in Figure 5.7. The expected shape of the RK8 points in this plot is not met at all. Instead of first horizontal and then linearly increasing, it is the other way around. Furthermore, if the optimal step size is similar to the one of DROs close to the secondary, it is expected to be lower than 10^{-3}, which is not even in the plot. This indicates that the range of step sizes Δt has been chosen incorrectly, and should be shifted to a lower region.

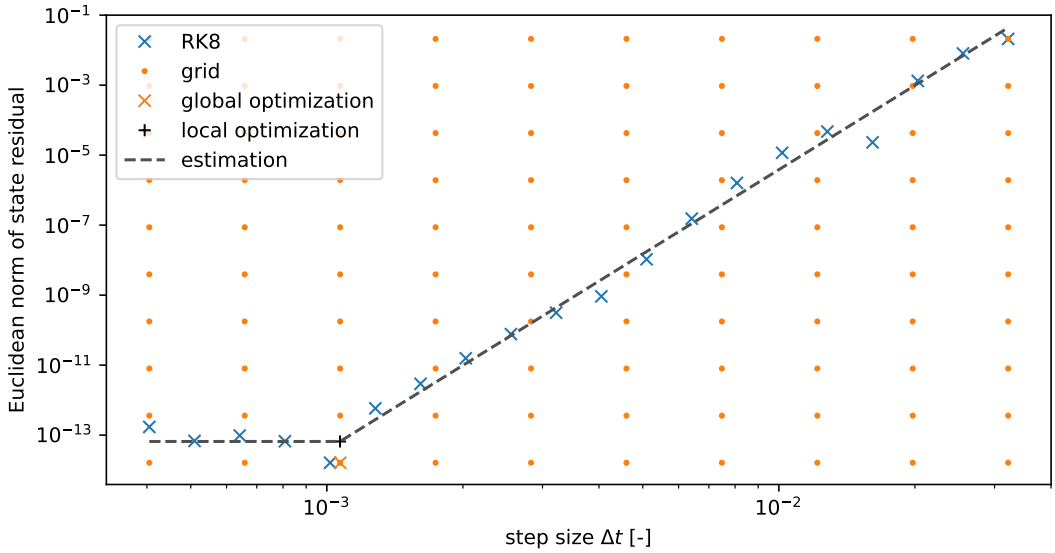

Figure 5.8: The Euclidean norm of the state residual depending on the step size Δt of the RK8 method. Global optimization via grid search and then local optimization via least squares method is performed to find the point between the region dominated by the truncation error and the region dominated by the rounding error. $\mu = 0.1$, $x_0 = -0.03$.

This can be seen in Figure 5.8. It should also be noted, how the region of step sizes Δt was defined previously, and how it is defined now: Previously – in Figures 5.4 to 5.7 –, the step size Δt went from one 1000^{th} to one 10^{th} of the duration of half a DRO. Now, the adjusted range for further calculations is from one $10\,000^{\text{th}}$ to one 100^{th} of the duration of half a DRO. This new range should not be applied to DROs that start far away from the primary, since it might exclude the optimal step size Δt. Therefore, it is only applied for $x_0 < 0.3 - \mu$.

The result of this can be seen in Figures 5.9 and 5.10. The step size in Figure 5.9 is behaving way more as expected; high in between primary and secondary and low close to primary and secondary. Only the data row that is closest to the primary – where $x_0 = 0.01 - \mu$ holds – is off, as it indicates a high step size. Also the optimal norm of the state residual in Figure 5.10 looks more promising than before in Figures 5.5 and 5.6: The residual does not exceed $2 \cdot 10^{-12}$ with the three data rows close to the primary being an exception. While this system does work better and for more DROs than before, there still seems to be a problem close to the primary. This could be solved by introducing even smaller step sizes for this region. Or – and this is the path that was chosen in this work – one could think about variable step sizes instead. This promises to be additionally helpful for DROs close to the primary, as they have a very high variability in acceleration as the orbits extend from very close to the primary to very far away from both, primary and secondary. Having a fixed step size Δt for those orbits means that all steps have to be performed with the small step size Δt that is required in the region close to the primary, even if this region resembles only a small fraction of the orbit.

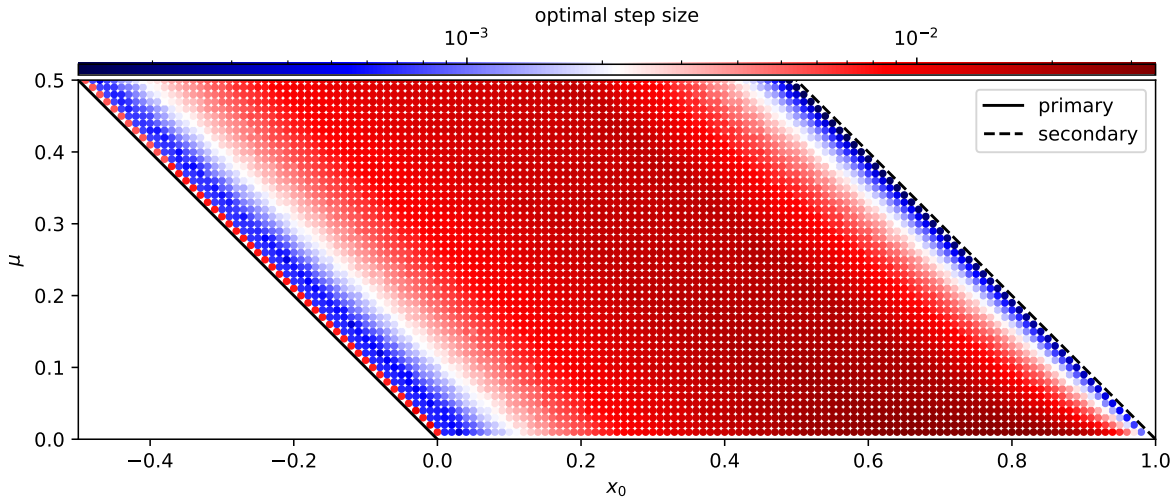

Figure 5.9: Optimal step size Δt depending on the mass ratio μ and the starting position x_0 of the DRO as calculated with the modified approach.

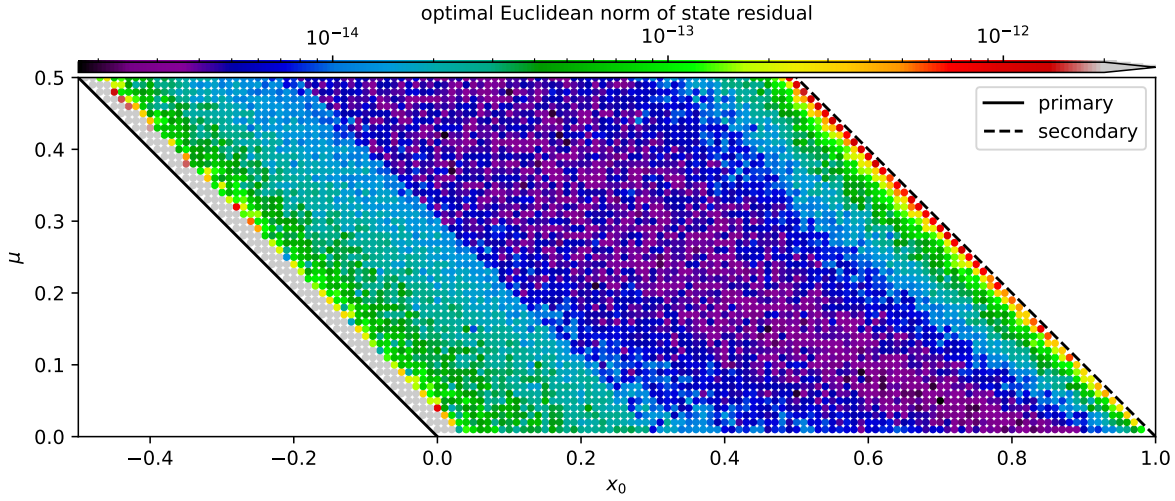

Figure 5.10: Euclidean norm of the state residual when using the optimal step size Δt as depicted in Figure 5.9.

But before introducing variable step size methods in the next section, Figure 5.10 should be analyzed further. As said before, the new range of step sizes Δt is applied to DROs that are *left* of the line $x_0 = 0.3 - \mu$. In Figure 5.6 it looks like using this line is a safe choice; *safe* meaning that all the DROs whose optimal step size Δt is not found in the original approach are *safely* taken into account. Since the "problems" in Figure 5.6 start only left of the line $x_0 = 0.2 - \mu$, they should all be taken into account. This does not correspond with the findings of Figure 5.10: The line $x_0 = 0.3 - \mu$ can clearly be seen, as the numbers for the optimal Euclidean norm of the state residual are higher than in Figure 5.6 – even right behind the border where there should be no difference, which needs to be investigated further.

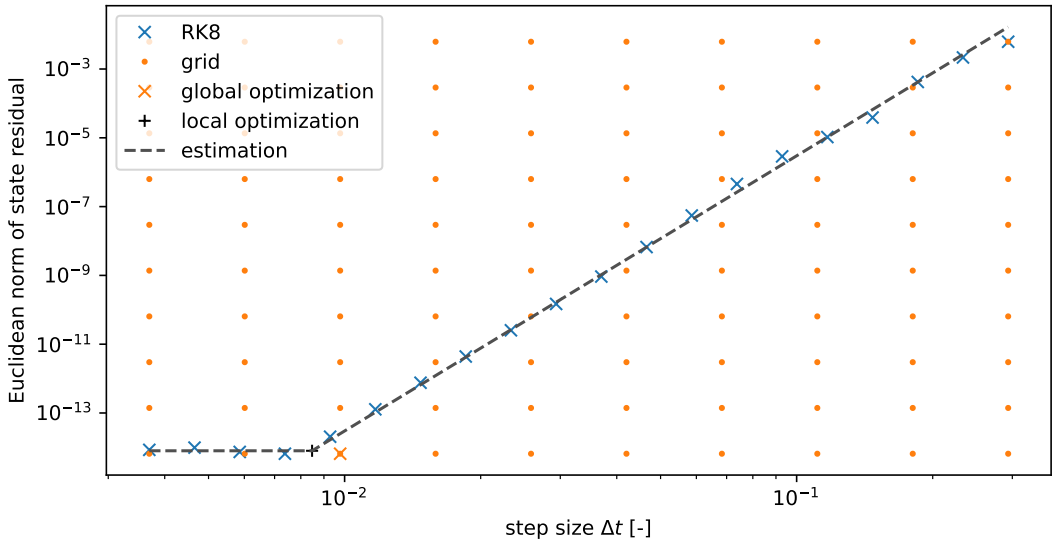

Figure 5.11: The Euclidean norm of the state residual depending on the step size Δt of the RK8 method. Global optimization via grid search and then local optimization via least squares method is performed to find the point between the region dominated by the truncation error and the region dominated by the rounding error. $\mu = 0.1$, $x_0 = 0.19$.

To come up with an answer, a specific point left of the line $x_0 = 0.3 - \mu$, but very close to it is investigated. It is the point where $\mu = 0.1$ and $x_0 = 0.19$. Figure 5.11 shows the original approach, and it can clearly be seen that the algorithm finds a reasonably looking optimum point. Now, for Figure 5.12, the range of step sizes Δt is shifted to lower step sizes by a factor 10. It should be noted that the scale of the vertical axis of Figure 5.12 is wildly different from the one in Figure 5.11. It is apparent that incorporating more data with very low step sizes Δt means incorporating more data that deviates from the horizontal line, as the residual gets slightly larger for smaller step sizes Δt. This is different from the anticipated constant behavior that has been used to model the optimization problem and is the reason for the Euclidean norm of the state residual being higher when incorporating lower step sizes Δt. Therefore, this small discrepancy is not a problem itself and can be explained easily. However, even the new method does not seem to work for all DROs since the ones that start close to the primary do still not work correctly, as can be seen in Figures 5.9 and 5.10. For that reason and because a fixed step size Δt does not seem to be right for DROs as accelerations can vary significantly during a single orbit, the possibilities of having a variable step size Δt will be explored in the next section.

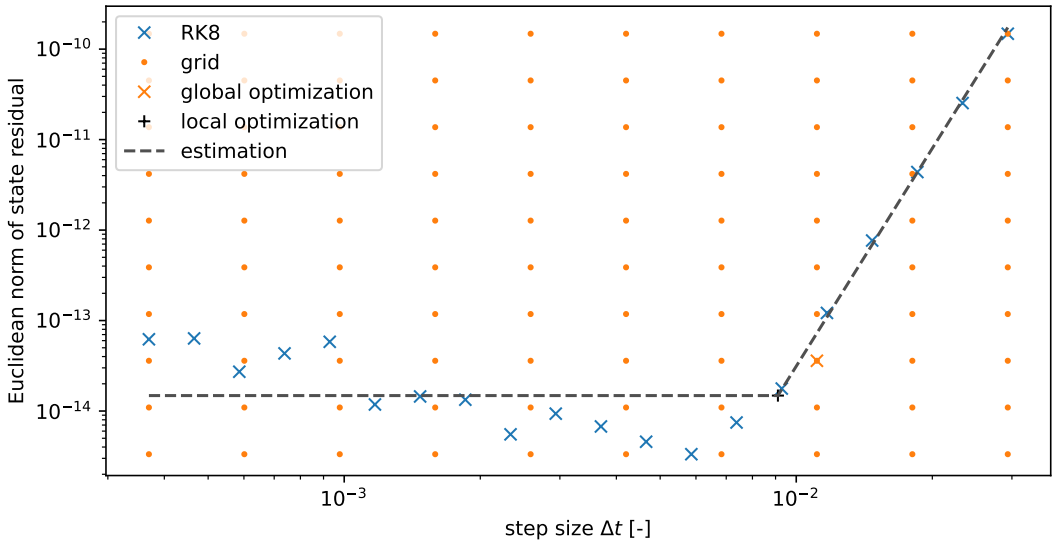

Figure 5.12: The Euclidean norm of the state residual depending on the step size Δt of the RK8 method. Global optimization via grid search and then local optimization via least squares method is performed to find the point between the region dominated by the truncation error and the region dominated by the rounding error. $\mu = 0.1$, $x_0 = 0.19$.

5.2. Variable Step Size Runge-Kutta Methods

The integration method that is investigated in this section is the eighth-order variable step-size Runge-Kutta method (DOP853) that is already implemented in *SciPy*. Its order is 8, which coincides with the previously analyzed RK8, so that the two methods are comparable. While fixed step size methods are characterized by their step size, variable step size methods are characterized with their tolerance. They are briefly explained in [44]: The solver adapts the step size such that the estimate for the local truncation error stays below the tolerance. The estimate is made with using an RK method with a different order, in the case of DOP853 this is done with a third- and a fifth-order RK method (hence the name).

Figures 5.13 to 5.15 show the Euclidean norm of the state residual depending on the number of function evaluations for RK8 and DOP853 for different values of the starting position x_0. The three figures are all in the EMLS; equivalent figures for SELS, SJLS, and PCLS can be found in Appendix B. The general trend in all figures and for both RK8 and DOP853 is from top left to bottom right – which is expected. And yet, in Figure 5.13 the DOP853 method seems to perform very well with a residual that is lower than 10^{-13} while at the same time using only 26 function evaluations. In order to explain this phenomenon it should be noted that residual does not mean error: The *error* that is made by the propagation is actually unknown, since there is no analytical solution for it. Therefore, the error is approximated using the difference between a propagation and a more accurate propagation. This difference is called *residual*. When the number of function evaluations is 26 and the tolerance is increased by only a small amount, the number of function evaluations is still 26, with only the time partitions altered a tiny bit. Therefore, the "more accurate" propagation that is used for computing the residual is not at all more accurate, it is almost the same which leads to the residual being very close to zero. As a result, for the further analysis those data points will be excluded as they are misleading.

The plots show three important key insights: Firstly, for a given residual, there is always a DOP853 that needs less function evaluations than the respective RK8 method. Secondly, by how much DOP853 is better than RK8 depends on the starting location x_0: Close to the secondary, where the accelerations do not change very much along one orbit, the difference is smaller than close to the primary, where the accelerations change significantly along one orbit. This is expected, since the benefits of having a variable step size are large if a large range of step sizes is actually used – which is the case when the accelerations vary much.

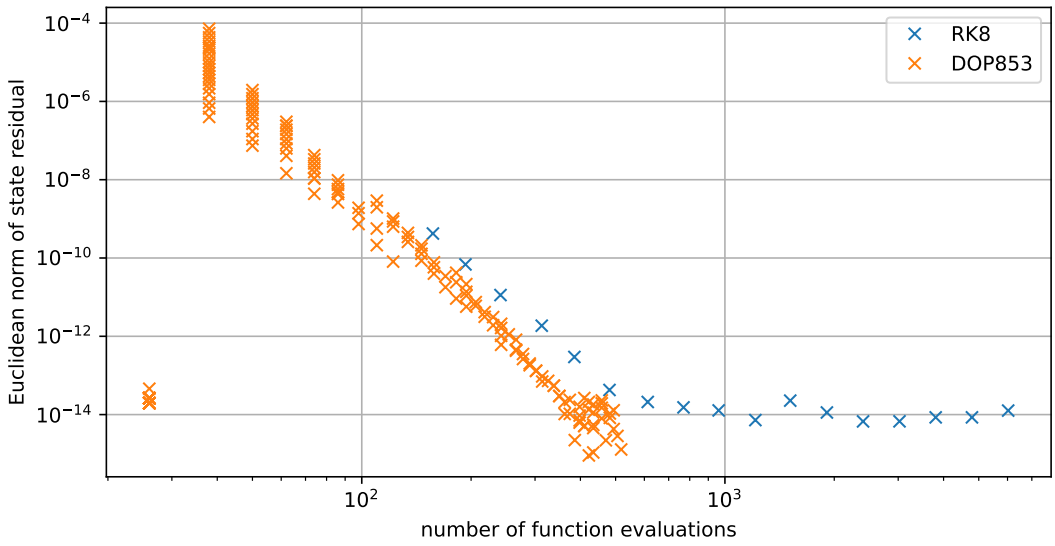

Figure 5.13: Euclidean norm of the state residuals depending on the number of function evaluations for RK8 and DOP853. $\mu = 0.01$ (EMLS) and $x_0 = -\mu + 0.95$.

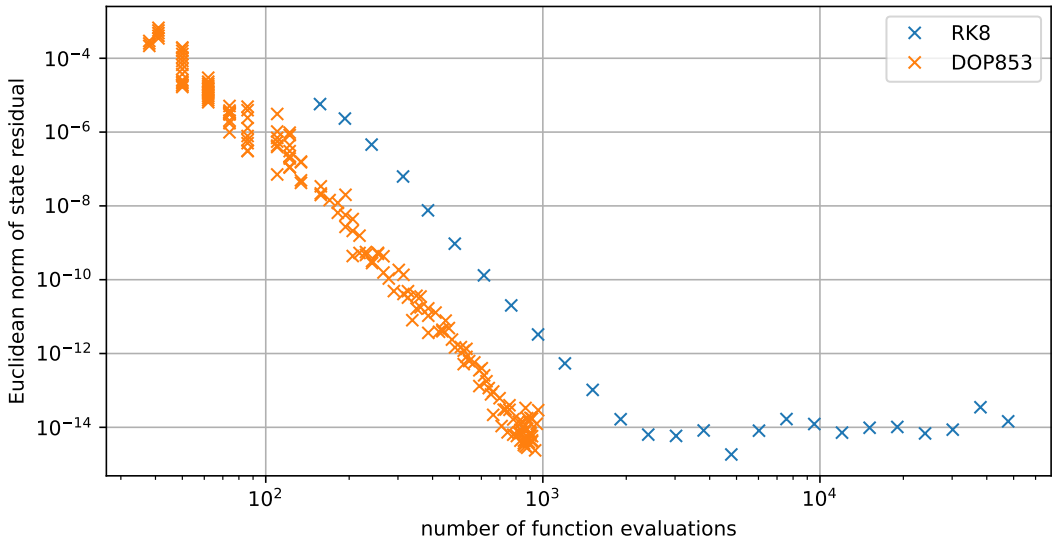

Figure 5.14: Euclidean norm of the state residuals depending on the number of function evaluations for RK8 and DOP853. $\mu = 0.01$ (EMLS) and $x_0 = -\mu + 0.5$.

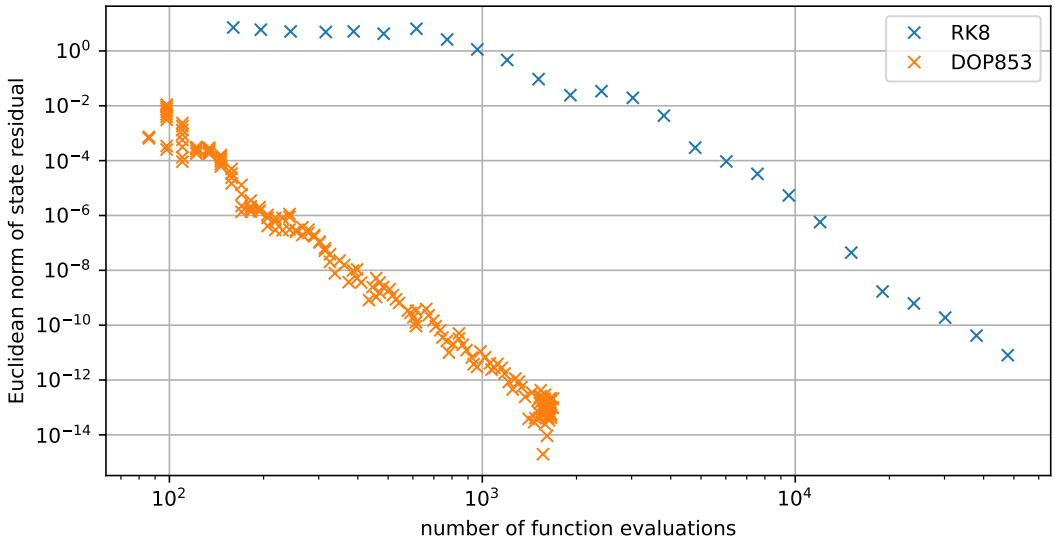

Figure 5.15: Euclidean norm of the state residuals depending on the number of function evaluations for RK8 and DOP853. $\mu = 0.01$ (EMLS) and $x_0 = -\mu + 0.05$.

Thirdly: When the tolerance is lowered beyond a “reasonable point” (the point at which no improvement in terms of residual is possible due to rounding errors), the number of function evaluations does not increase further with the residual staying approximately constant. This is insofar important as it implies that there is no optimum for the tolerance; increasing the tolerance never results in a worse residual or in too many function evaluation. Therefore, the recommendation for using this specific implementation of DOP853 is to set the tolerance as low as possible. If the computation time is required to be smaller, Figures 5.13 to 5.15 can help to determine how many function evaluations will be needed for a certain accuracy. Though this is not expected as the variable step size DOP853 reduced the number of function evaluations for the computation-heavy DROs that are close to the primary compared to RK8 by more than the factor 10, as can be seen in Figure 5.15.

It should be mentioned that in Figure 5.15 no enhancement takes place for RK8 between 100 and 1000 function evaluations. This is not surprising, as for 1000 function evaluations the propagation is already quite bad with the residual being 1, which is the distance between primary and secondary. As there is not much room for further worsening as the number of function evaluations becomes even lower, the residual stays almost the same (at least in this logarithmic plot).

5.3. Conclusions

It can be concluded that among the fixed step size RK methods that have been investigated, RK8 has performed best. It was archived to provide an overview of which step size is recommended for which orbit, which can be seen in Figure 5.10. This is except for DROs that start very close to the primary. Their computation time is too long to be analyzed efficiently, which is why alternatives to RK8 have been investigated. It has then be proven that DOP853 performs better than RK8 under all tested conditions and that the tolerance setting can be set to the lowest possible value without loosing accuracy and without needing too many function evaluations.

6

Modeling with Fourier Series

In order to obtain an estimate of the shape of a DRO without actually having to numerically propagate half an orbit, Hirani and Russel proposed in [17] to model DROs with Fourier series. Their approach is explained in the first section of this chapter, followed by the analysis of a novel approach that takes the shape of DROs more into account.

6.1. Traditional Approach

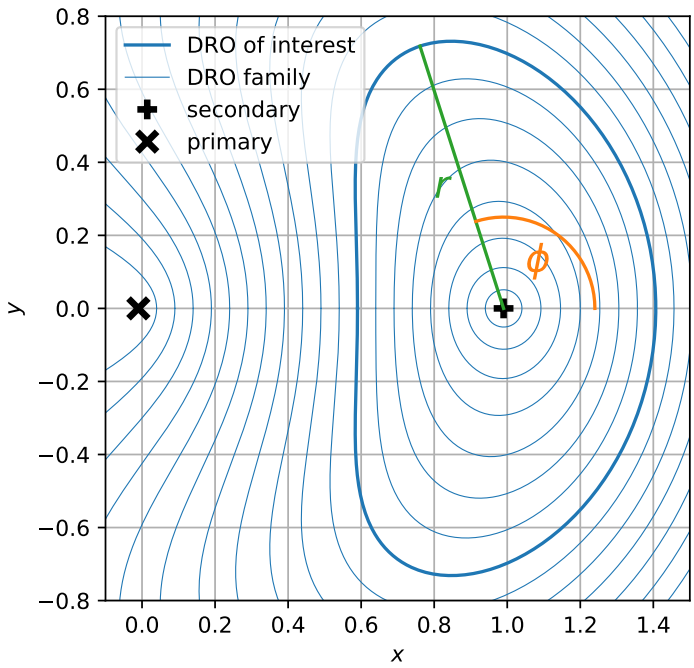

Figure 6.1: Example DROs in the EMLS ($\mu = 0.01$). The highlighted DRO has the starting location $x_0 - x_1 = 0.6$. The definition of ϕ and r can be concluded from this plot.

The approach explained in this section follows very closely Hirani and Russell [17]. However, some minor changes have been applied, which will be important later. The x- and y-positions are approximated using Fourier series that are functions of the angle ϕ. The introduced angle ϕ is defined as the angle between the current position, the secondary and the x-axis. This can be seen in Figure 6.1; further it should be noted that this angle is called θ in [17]. The Fourier coefficients for any orbit given by $x(\phi)$ and $y(\phi)$ are retrieved by evaluating $x(\phi)$ and $y(\phi)$ at 256 equally spaced angles ϕ_1 to ϕ_{256}. The Fourier series is restricted to have N cosine and sine parameters, respectively. Because DROs are

symmetric with respect to the x-axis, the coefficients for the sine terms are zero for $x(\phi)$ as well as the cosine terms for $y(\phi)$ and can thus be eliminated. Therefore, $x(\phi)$ can be approximated using the parameters a_0 to a_N as:

$$x(\phi) \approx \sum_{n=0}^{N} a_n \cos(n\phi) \tag{6.1}$$

while $y(\phi)$ uses the parameters b_1 to b_N:

$$y(\phi) \approx \sum_{n=1}^{N} b_n \sin(n\phi) \tag{6.2}$$

The parameters a_0 to a_N and b_1 to b_N are chosen such that at the angles ϕ_1 to ϕ_{256} the following systems of equations are satisfied as good as possible – meaning that the sum of the squares of the residuals is to be minimized:

$$\begin{bmatrix} x(\phi_1) \\ x(\phi_2) \\ \vdots \\ x(\phi_{256}) \end{bmatrix} \approx \begin{bmatrix} 1 & \cos(\phi_1) & \cos(2\phi_1) & \cdots & \cos(N\phi_1) \\ 1 & \cos(\phi_2) & \cos(2\phi_2) & \cdots & \cos(N\phi_2) \\ \vdots & \vdots & \vdots & \ddots & \vdots \\ 1 & \cos(\phi_{256}) & \cos(2\phi_{256}) & \cdots & \cos(N\phi_{256}) \end{bmatrix} \begin{bmatrix} a_0 \\ a_1 \\ a_2 \\ \vdots \\ a_N \end{bmatrix} \tag{6.3}$$

$$\begin{bmatrix} y(\phi_1) \\ y(\phi_2) \\ \vdots \\ y(\phi_{256}) \end{bmatrix} \approx \begin{bmatrix} \sin(\phi_1) & \sin(2\phi_1) & \cdots & \sin(N\phi_1) \\ \sin(\phi_2) & \sin(2\phi_2) & \cdots & \sin(N\phi_2) \\ \vdots & \vdots & \ddots & \vdots \\ \sin(\phi_{256}) & \sin(2\phi_{256}) & \cdots & \sin(N\phi_{256}) \end{bmatrix} \begin{bmatrix} b_1 \\ b_2 \\ \vdots \\ b_N \end{bmatrix} \tag{6.4}$$

One way to obtain the best solution is by solving the arising least-squares problem, for which several implementations exists. Within the scope of this thesis, the *NumPy* function `numpy.linalg.lstsq()` is used, which yields the $2N + 1$ Fourier coefficients for the specific DRO. However, the goal is to have a model for the entire family of DROs for one specific CR3BP. In order to archive that, a finite number (256 in [17]) of DROs is regarded with the starting positions $x_{0,1}$ to $x_{0,256}$, for each of which all Fourier coefficients are computed. Each of the Fourier coefficients p is then approximated with an order C polynomial function:

$$p(x_0) = \sum_{s=0}^{C} d_s x_0^s \tag{6.5}$$

The parameters d_0 to d_C for each of the polynomials are the least squares solutions to the following system of equations:

$$\begin{bmatrix} p(x_{0,1}) \\ p(x_{0,2}) \\ \vdots \\ p(x_{0,256}) \end{bmatrix} \approx \begin{bmatrix} 1 & x_{0,1} & x_{0,1}^2 & \cdots & x_{0,1}^C \\ 1 & x_{0,2} & x_{0,2}^2 & \cdots & x_{0,2}^C \\ \vdots & \vdots & \vdots & \ddots & \vdots \\ 1 & x_{0,256} & x_{0,256}^2 & \cdots & x_{0,256}^C \end{bmatrix} \begin{bmatrix} d_0 \\ d_1 \\ d_2 \\ \vdots \\ d_C \end{bmatrix} \tag{6.6}$$

The total number of parameters needed for each Fourier coefficient is $C + 1$, which makes the total number of parameters $(2N + 1)(C + 1) \approx 2NC$.

Figures 6.2 and 6.3 show the deviations that this method introduces with respect to propagated orbits for the x- and y-coordinate, respectively. In order to restrict the DROs to a useful domain, only DROs with $x_0 \geq x_2 - 0.3$ are being considered. This is in line with [17]. In order to prevent "over-fitting", only 256 different values for x_0 are used to calculate the parameters, while 512 are used to test the accuracy of the model. For the same reason, 256 different angles ϕ had been uses to obtain the parameters, and 512 are used in Figures 6.2 and 6.3. It can clearly be seen that the model works as the maximum residual for the x-coordinate is about 10^{-6} and for the y-coordinate about 10^{-5}.

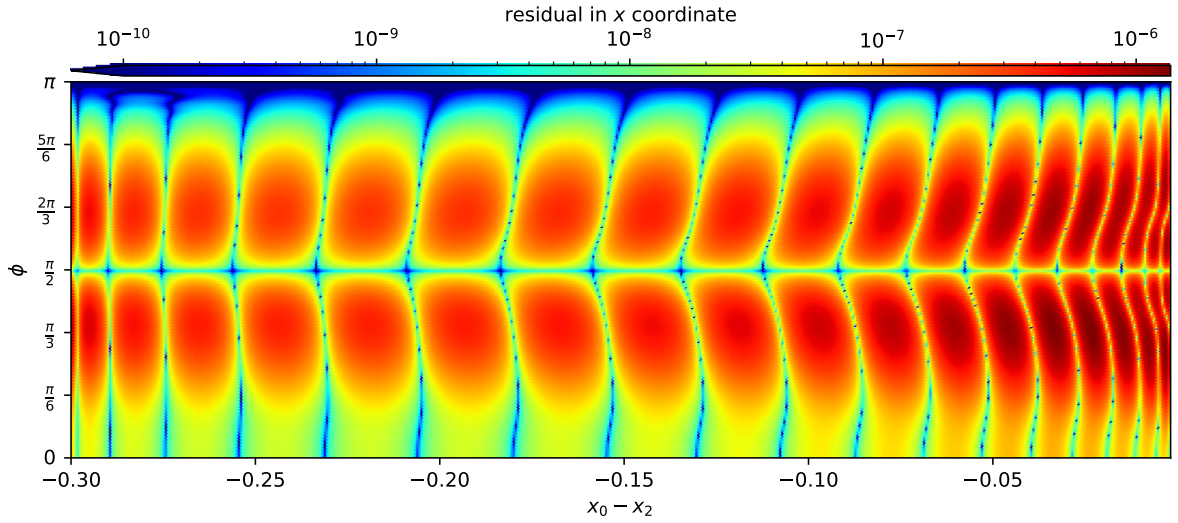

Figure 6.2: Residual in the x-coordinate depending on the angle ϕ and the starting location x_0 after modeling the DROs with a Fourier series of order $N = 50$ and a polynomial of order $C = 100$. $\mu = 2.528 \cdot 10^{-5}$.

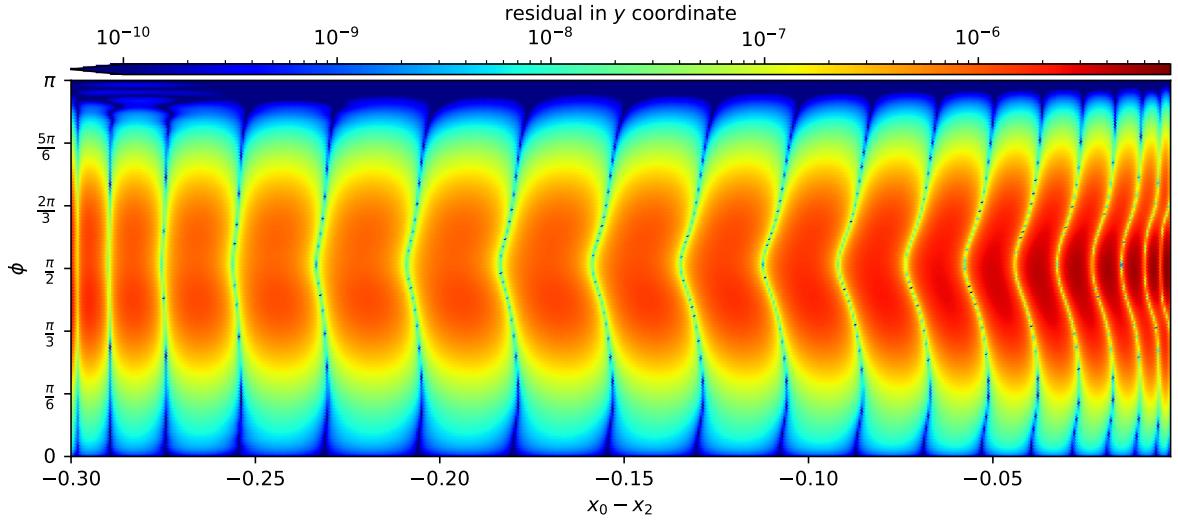

Figure 6.3: Residual in the y-coordinate depending on the angle ϕ and the starting location x_0 after modeling the DROs with a Fourier series of order $N = 50$ and a polynomial of order $C = 100$. $\mu = 2.528 \cdot 10^{-5}$.

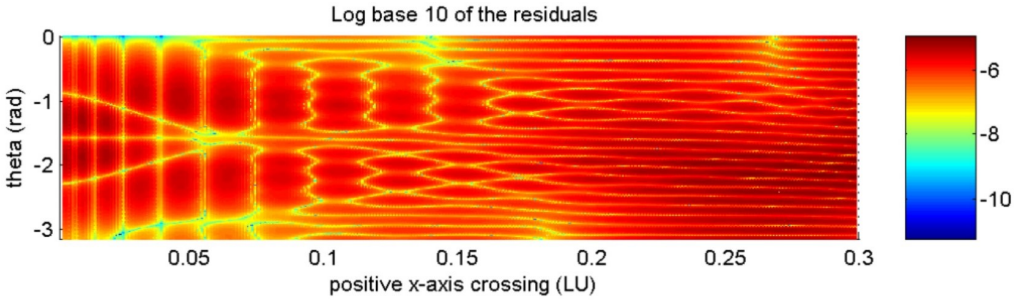

Figure 6.4: Residual in the x-coordinate depending on the angle theta and the starting location LU after modeling the DROs with a Fourier series of order $N = 50$ and a polynomial of order $C = 100$. $\mu = 2.528 \cdot 10^{-5}$. According to and taken from [17].

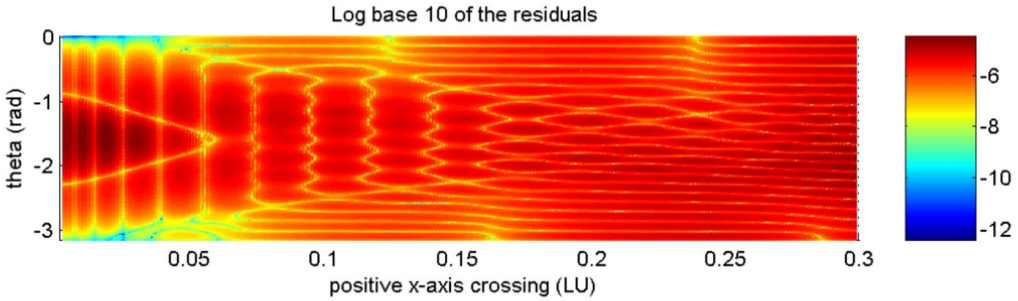

Figure 6.5: Residual in the y-coordinate depending on the angle theta and the starting location LU after modeling the DROs with a Fourier series of order $N = 50$ and a polynomial of order $C = 100$. $\mu = 2.528 \cdot 10^{-5}$. According to and taken from [17].

Figures 6.4 and 6.5 are directly taken from [17]. They represent the same problem and them showing the same order of magnitude for the residual as Figures 6.2 and 6.3 can be seen as verification for the implementation of the model. However, the pattern is obviously quite different. There is a plethora of reasons that could play a role here:

- [17] does not mention any of the propagation settings, for that reason the propagator, integrator, and step size are unknown.
- [17] does not mention how the interpolation for the times that are in between two time steps has been implemented. For this thesis, this is discussed in the next section.
- [17] does not mention the resolution of Figures 6.4 and 6.5, neither in terms of “positive x-axis crossing (LU)” nor in terms of “theta (rad)”. This is important because of potential over-/underfitting.

On the other hand, the following differences between the implementation in this thesis and [17] are probably *not* the reason for the discrepancy:

- The “x-axis crossing” in [17] is defined as the location where the DRO crosses the x-axis on the far side of the secondary, rather than the close side of the secondary as in this thesis. Since for the DROs that are considered, those two locations have a very similar distance to the secondary, this should not change the pattern. However, it should be mentioned that in Figures 6.4 and 6.5 the left-hand side of the plot represents the DROs close to the secondary while in Figures 6.2 and 6.3 this applies to the right-hand side of the plot.
- The propagations have been performed with different starting positions. Within this thesis, the propagations of DROs always start on the close side of the secondary, while in [17] they start on the far side of the secondary. For obvious reasons, the propagation error is smaller closer to the starting point of the propagation and bigger further away from it. Since the propagation errors introduced by the propagations performed in this thesis are generally smaller than the residuals seen in Figures 6.2 and 6.3, this can not be a problem. However, little is known about the error introduced by the propagations performed in [17].
- Furthermore, in order to obtain the Fourier and polynomial coefficients, in this thesis Equations (6.4) and (6.6) are evaluated while in [17] numerical integrals are used. This is not expected to make a difference as both are valid approaches in order to obtain Fourier and polynomial coefficients.

6.2. Interpolation

The DOP853 method yields the state only at discrete times and not any arbitrary angles ϕ. Therefore, in order to be able to get the distance r from the secondary as a function of ϕ, interpolation needs to be performed. Three different approaches will be mentioned here that will be compared to a benchmark. The benchmark is a propagation using the RK8 method with a lower step size than the DOP853 reaches,

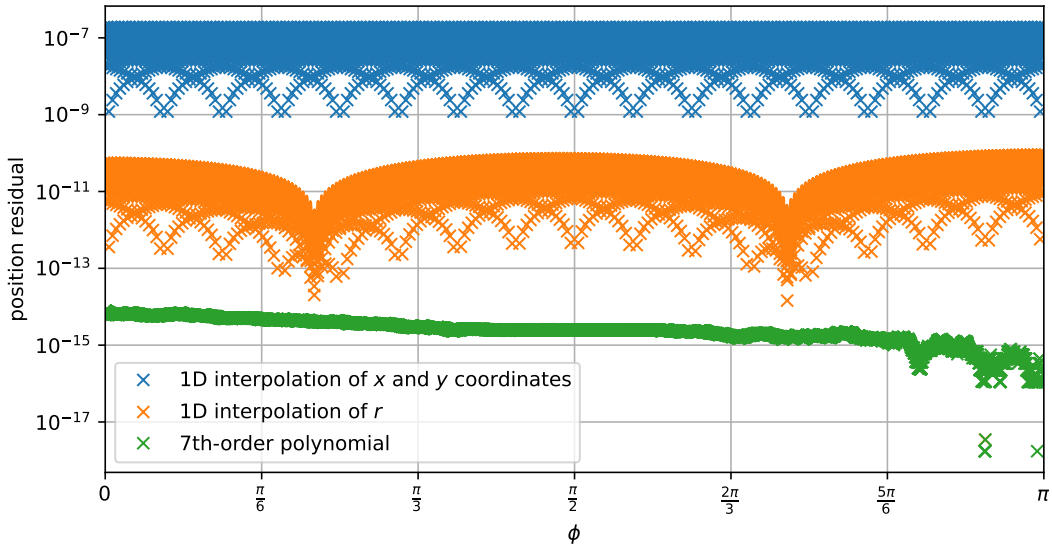

Figure 6.6: The residual of two different interpolation techniques and a 7th-order polynomial in position of the DRO with $\mu = 0.1$ and $x_0 - x_2 = -0.2$.

meaning that at more time instances the position on the DRO is available without the need for interpolation.

The three approaches are the following. Firstly, the position x, y can be linearly interpolated between two available positions. This has the obvious disadvantage of not taking the curvature of the DRO into account at all. This is corrected for in the second approach: Instead of interpolating the coordinates x and y, for any given angle ϕ the distance r from the secondary is linearly interpolated. This is expected to perform better than the first approach. The third approach is to make use of the in *SciPy* already implemented option to output a continuous function when solving an ivp with `scipy.integrate.solve_ivp`. According to the *SciPy* documentation [44], in the case of DOP853 this is a 7th-order polynomial function.

Figure 6.6 shows that – as expected – the second approach performs better than the first approach. It becomes also clear that the 7th-order polynomial is better than the other two options, making it the preferred interpolation technique. The residual is consistently below 10^{-14}, which coincides quite well with the accuracy that is reached with the chosen integrator setting, as can be seen in Figures 5.13 to 5.15. Therefore, the interpolation with the 7th-order polynomial is as good as the propagation itself, which means this interpolation is not a source of extra errors. Hence, there is no need to search for other, more sophisticated, interpolation techniques and this 7th-order polynomial will be used for the next sections.

6.3. New Set of Elements

In order to obtain a method that (hopefully) requires less Fourier parameters for the same accuracy of the orbits, a new set of elements is developed that is oriented more along the actual shape of DROs than the xy-coordinate system. Then, one of the parameters (which will be called ψ) is supposed to represent the location on the orbit while the other parameter (which will be called c) should be approximately constant during one DRO. Then, doing a Fourier transformation of $c(\psi)$ should be more accurate with less Fourier parameters than the one of $x, y(\phi)$. The coordinate transformation that is necessary to go from the xy-system to the ϕc-system is explained in the following.

As can be seen in Figure 6.7, the DROs are almost elliptical orbits around the secondary. Those ellipses, however, are bent around the primary. This effect can be resolved by regarding instead of

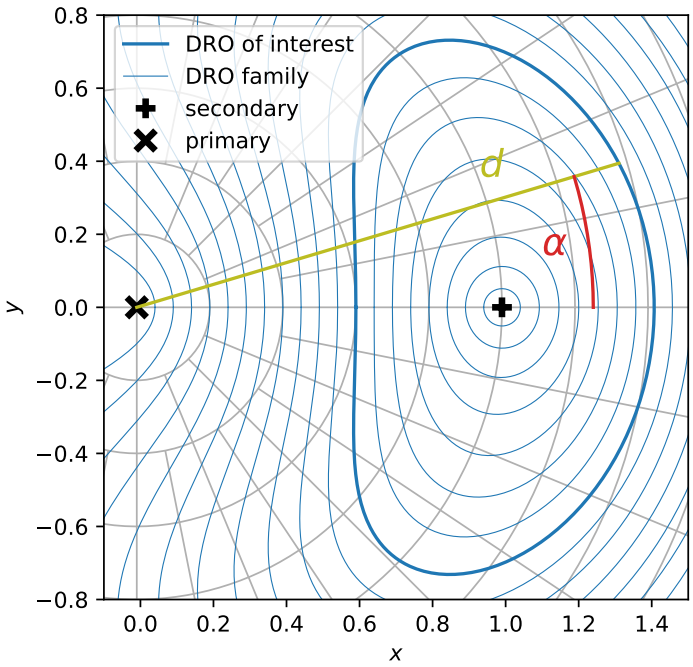

Figure 6.7: Example DROs in the EMLS ($\mu = 0.01$). The highlighted DRO has the starting location $x_0 - x_1 = 0.6$. The definition of α and d can be concluded from this plot.

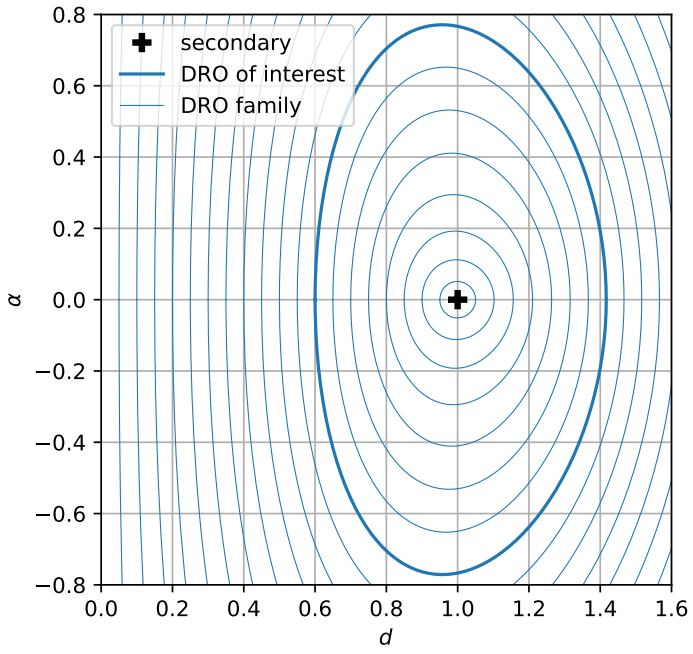

Figure 6.8: Example DROs shown in the $d\alpha$-coordinate system.

x and y the angle α that any point makes with the primary and the x-axis, and the distance d to the primary. The result of this can be seen in the $d\alpha$-coordinate system in Figure 6.8. The DROs now look a lot more like ellipses than before. While the DROs that are very close to the secondary look like circles, the DROs that are further away clearly look like ellipses with a side ratio of about two to one. This is no coincidence: Close to the secondary the DROs are circular because in this region the primary acts as nothing more than a third-body perturbation. Its gravitational forces are small compared to the ones from the secondary, which makes close-to-circular orbits possible. On the other hand, further away from the secondary, the gravitational force from the secondary is increasingly small, which brings the system closer to the assumptions of the Hill problem [15] – a secondary with negligible mass. This assumption leads to the DROs indeed being elliptical with a two-to-one side ratio, which explains the observations from Figure 6.8.

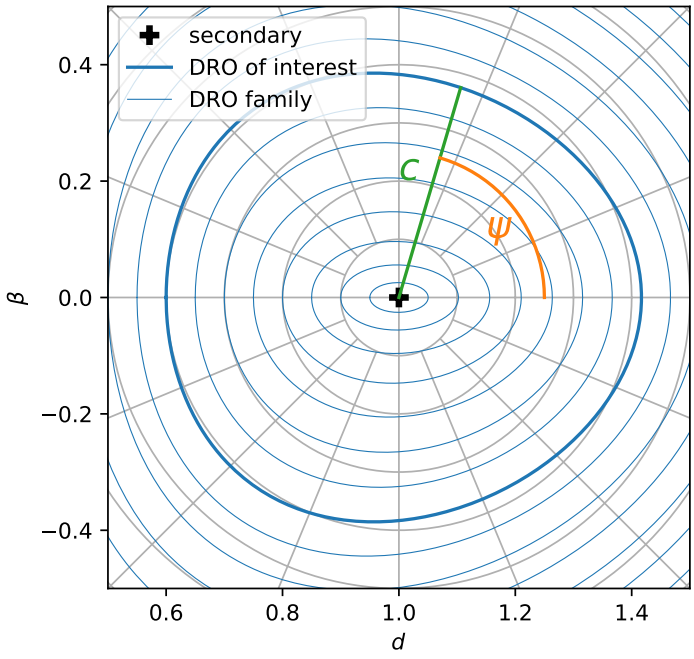

Figure 6.9: Example DROs in the $d\beta$-coordinate system. The definition of ψ and c can be concluded from this plot.

Therefore, the α-coordinate is divided by two, resulting in the β-coordinate. The $d\beta$-coordinate system can be found in Figure 6.9. It is apparent that now – given a certain distance from the secondary – the DROs are almost circular while the small DROs now have a one-to-one-half side ratio. The reason why the distant DROs have been preferred over the close DROs is in the name: *Distant Retrograde Orbit*. The orbits that are close to the secondary are ordinary two-body orbits with a third-body perturbation from the primary. There are many studies on those already, and therefore the focus of this thesis is not on them. Figure 6.10 shows the function $c(\psi)$. As it was intended, for each of the DROs c is almost constant. The coordinate transformation from xy to ψc can be summarized with a few equations:

$$\begin{aligned} d &= \sqrt{(x-x_1)^2+y^2}, \qquad \alpha = \arctan 2\,(y, x-x_1)\,, \qquad \beta = \frac{\alpha}{2}, \\ c &= \sqrt{(d-1)^2+\beta^2}, \qquad \psi = \arctan 2\,(\beta, d-1) \end{aligned} \tag{6.7}$$

Here, $\arctan 2(b,a)$ is the function giving the angle that is associated with the coordinates $(x,y) = (a,b)$. The equations for the reversed transformation are:

$$\begin{aligned} d &= 1 + c\cos(\psi), \qquad \beta = c\sin(\psi), \qquad \alpha = 2\beta \\ x &= x_1 + d\cos(\alpha), \qquad y = d\sin(\alpha) \end{aligned} \tag{6.8}$$

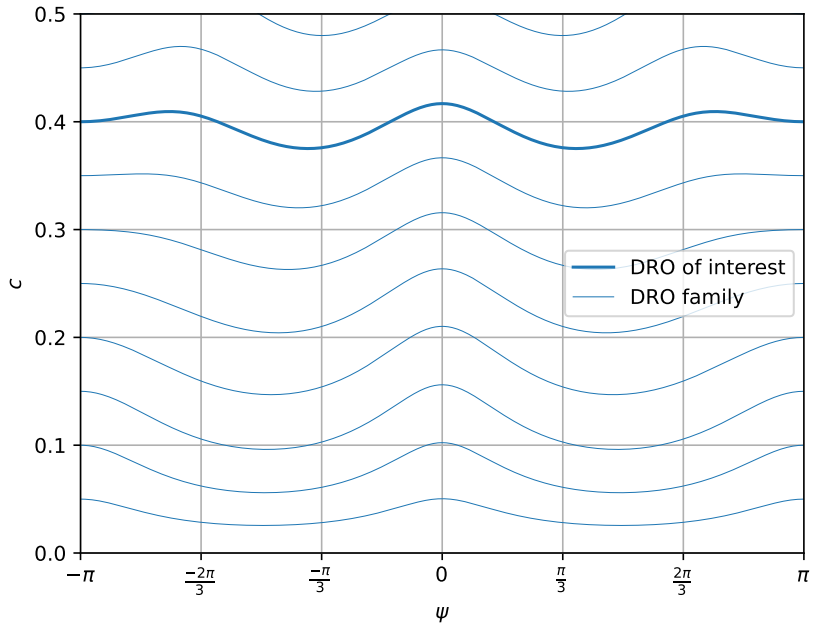

Figure 6.10: Example DROs in the ψc-coordinate system.

With these equations being defined, the function $c(\psi)$ can be modeled with a Fourier series in the same way as $x, y(\phi)$ had been modeled before. Again, due to the symmetry properties of the DROs, only the cosine terms are needed for modeling $c(\psi)$ as:

$$c(\psi) \approx \sum_{n=0}^{N} a_n \cos(n\psi) \tag{6.9}$$

With the parameters a_0 to a_N being determined as the least squares solution of the following system of linear equations:

$$\begin{bmatrix} c(\psi_1) \\ c(\psi_2) \\ \vdots \\ c(\psi_{256}) \end{bmatrix} \approx \begin{bmatrix} 1 & \cos(\psi_1) & \cos(2\psi_1) & \cdots & \cos(N\psi_1) \\ 1 & \cos(\psi_2) & \cos(2\psi_2) & \cdots & \cos(N\psi_2) \\ \vdots & \vdots & \vdots & \ddots & \vdots \\ 1 & \cos(\psi_{256}) & \cos(2\psi_{256}) & \cdots & \cos(N\psi_{256}) \end{bmatrix} \begin{bmatrix} a_0 \\ a_1 \\ a_2 \\ \vdots \\ a_N \end{bmatrix} \tag{6.10}$$

Hence, the total number of parameters needed for this approach can be expressed as $(N+1)(C+1) \approx NC$.

It should be noted that with this approach not only the position along the orbit, but also the velocity can be approximated. This is derived in Appendix C. It should also be noted that for mission design, the first and second derivatives of position and velocity with respect to the parameters x_0 and ψ are beneficial – according to [17]. This model presents analytical expressions for position and velocity, that can therefore be derived analytically. Considerations regarding mission design, however, are beyond the scope of this thesis.

6.4. Results

The maximal positional residual for any location on any orbit with $-0.3 \leq x_0 - x_2 < -0.3$ as a function of the total number of parameters is depicted in Figure 6.11. For this example, the EMLS with $\mu = 0.01$ has been chosen. In order to evaluate what relation between the order N of the Fourier series and the order C of the polynomial is optimal, various ratios have been tested. Furthermore, in order to judge if

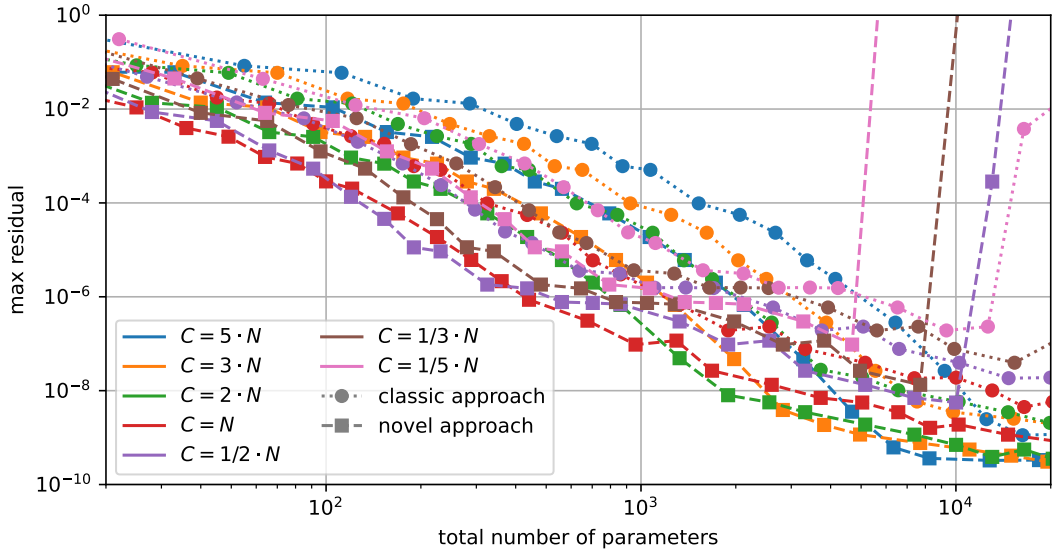

Figure 6.11: The maximum residual depending on the total number of parameters – combining N and C. Different ratios of N and C are shown as well as both, the classic approach and the novel approach. $\mu = 0.01$.

the classic approach or the novel approach performs better, both of them can be found in Figure 6.11. The general trend is that the residual decreases as more parameters are being used, which is in line with expectations. Once the number of parameters exceeds a certain threshold, the residual increases very rapidly. The threshold depends on the ratio of N and C and on the approach used; using the novel approach with $C = 1/5 \cdot N$ yields a jump at less than 5000 parameters in total. As the total number of parameters is about $N \cdot C$, this means that $N \approx 150$ and $C \approx 30$. For $C = 1/3 \cdot N$, this happens for the total number of parameters being about 7500, which translates to $N \approx 150$ and $C \approx 50$. For $C = 1/2 \cdot N$, the total number of parameters is about $11\,000$, meaning $N \approx 150$ and $C \approx 75$. Clearly there is a pattern here: If N exceeds 150, the maximal residual skyrockets. This also explains why for the traditional approach this happens only for higher total numbers of parameters: It calculates as $2CN$ rather than CN, meaning that a larger total number is needed in order to obtain the same N. The 150 is close the number of samples per orbit, which was set to be 256. This indicates that the problem that occurs here is overfitting. A note should be added to the difference between 150 and 256: The horizontal distance of two data points in Figure 6.11 is a factor of about 1.5. The mentioned thresholds of 5000, 7500, and $11\,000$ total parameters are lower bounds since the last “good” point was considered here, instead of considering the first “bad” point. Therefore, the difference between 150 and 256 is nothing to worry about.

However, the most important insight from Figure 6.11 is that the novel approach reliably outruns the classic approach. Meaning that with the same N-to-C-ratio, the novel approach always has a lower maximum residual than the classic approach – at least as long as the aforementioned threshold is not exceeded.

Figure 6.12 shows a less crowded version of Figure 6.11 – the lines for the classic approach have been removed. Now, when it comes to evaluating which ratio of N and C is best, for any number of total parameters the lowest line – the one with the lowest maximal residual – has to be taken into account. It is apparent that the best ratio is not consistent, it depends on the total number of parameters. However, it is clear that N and C should be *about the same*. For a large faction of the plot – namely for the total number of parameters being smaller than 3000 – the ratios 2, 1, and $1/2$ are to be preferred, indicating that N and C should be about the same. For more than 3000 parameters in total, it seems to be more advantageous to have a C that is larger than N, as in this region the ratios 3 and 5 are superior.

In order to get a more detailed overview of what is happening here, Figures 6.13 and 6.14 show the maximum residual depending on N and C, respectively, with the other one being fixed. Both plots show

that increasing one of the two orders N and C too far without adjusting the other is not very rewarding in terms of a smaller residual. Therefore, the plots suggest – as it was suspected before – that N and C should be chosen to be similar. And yet, there is a slight difference visible: While in Figure 6.13 for $C = 10$ a larger N is helpful until $N \approx 13$, Figure 6.14 shows that for $N = 10$ a larger C is helpful only until $C \approx 7$. This means that for the total number of parameters being $(7 + 1)(13 + 1) = 112$, a ratio of $C = 7/13$ is optimal, which can also be read from Figure 6.12. Similarly, the other findings from Figure 6.12 are represented in Figures 6.13 and 6.14 as well.

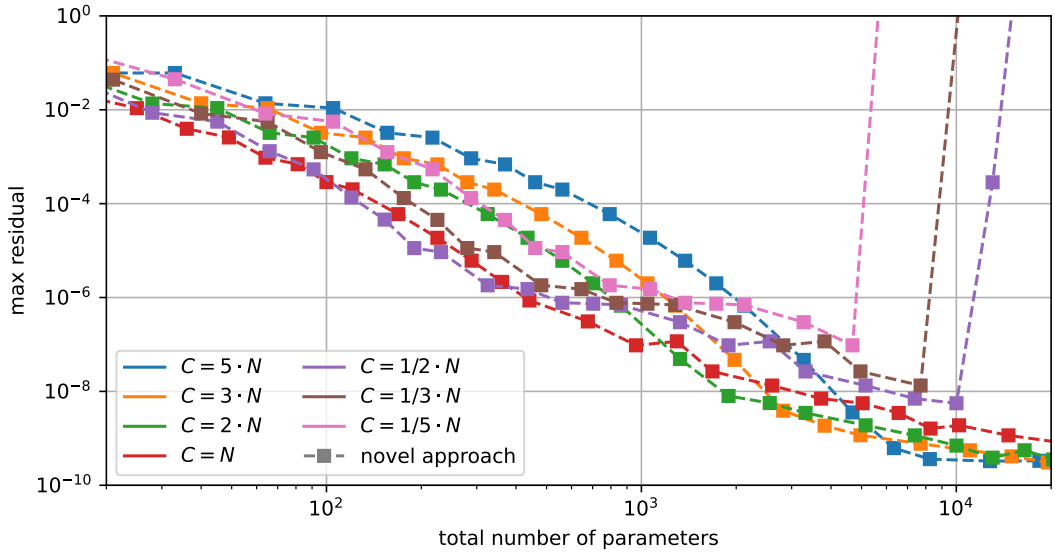

Figure 6.12: The maximum residual depending on the total number of parameters – combining N and C. Different ratios of N and C are shown in the novel approach. $\mu = 0.01$.

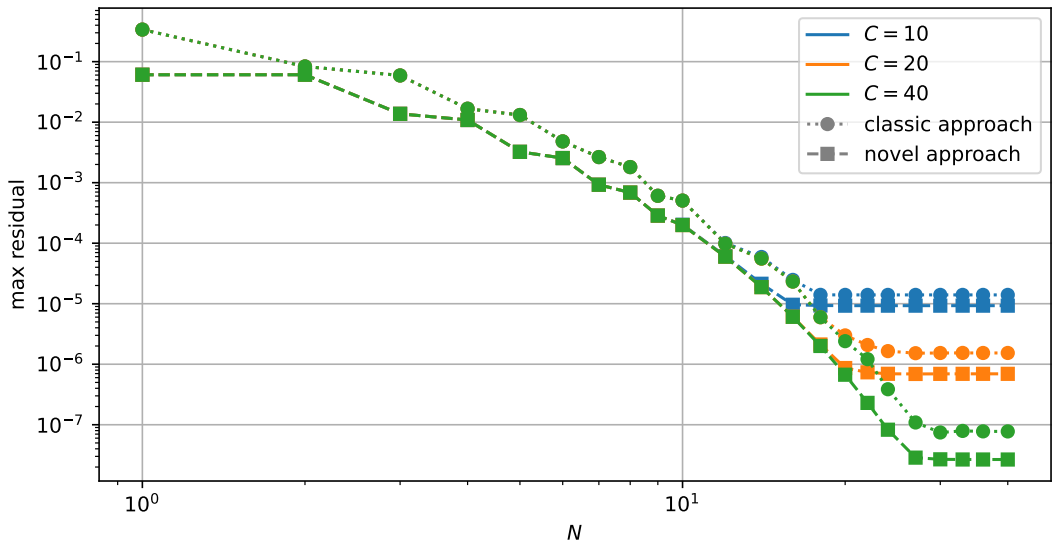

Figure 6.13: The maximum residual depending on N with C being a fixed number. Both, the classic approach and the novel approach are shown. $\mu = 0.01$.

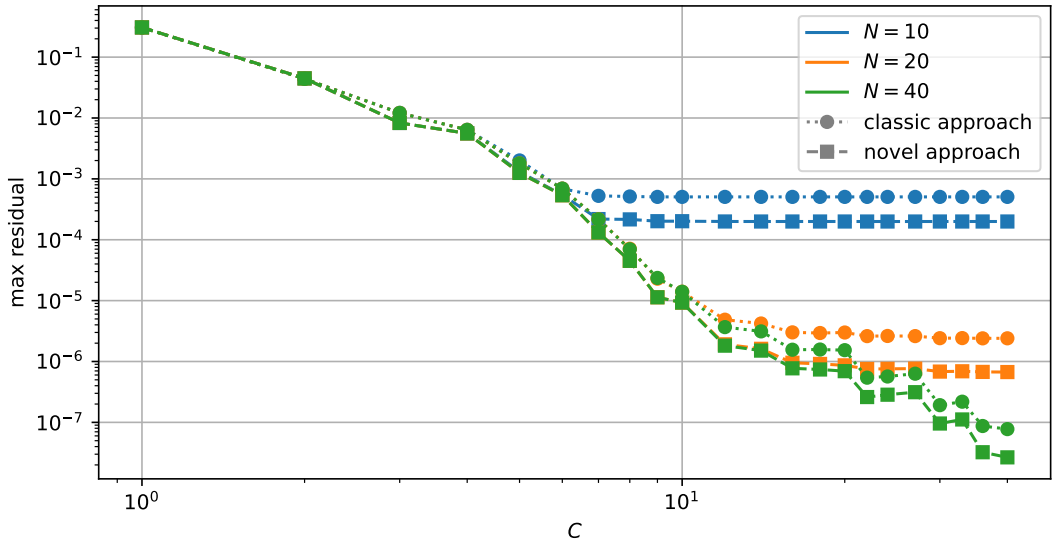

Figure 6.14: The maximum residual depending on C with N being a fixed number. Both, the classic approach and the novel approach are shown. $\mu = 0.01$.

7

Stability

Analyzing stability is a crucial part of this thesis as their stability is the strongest argument for DROs. Therefore, after general remarks on stability in Section 7.1, the stability of DROs in the CR3BP is evaluated in Section 7.2. However, this is only a model of reality and in order to provide an insight into how the stability of DROs is affected by perturbations, this is discussed in Sections 7.3 to 7.5.

7.1. Introduction

The stability of closed, non-disturbed orbits can be assessed with the eigenvalues of the monodromy matrix $\mathbf{M}$, which is the state transition matrix $\mathbf{\Phi}$ after exactly one revolution. Any (small) state change $\Delta\mathbf{X}_0$ at time $t = 0$ (the start of the first revolution) results in the state change $\Delta\mathbf{X}_1 = \mathbf{M}\Delta\mathbf{X}_0$ after one revolution. Therefore, the state change after n revolutions is $\Delta\mathbf{X}_n = \mathbf{M}\Delta\mathbf{X}_{n-1} = \mathbf{M}^n\Delta\mathbf{X}_0$. This clearly shows that it can be guaranteed that a (small) state change $\Delta\mathbf{X}$ does not grow with every revolution if and only if for all eigenvalues λ of the monodromy matrix $\mathbf{M}$ it holds that $|\lambda| \leq 1$.

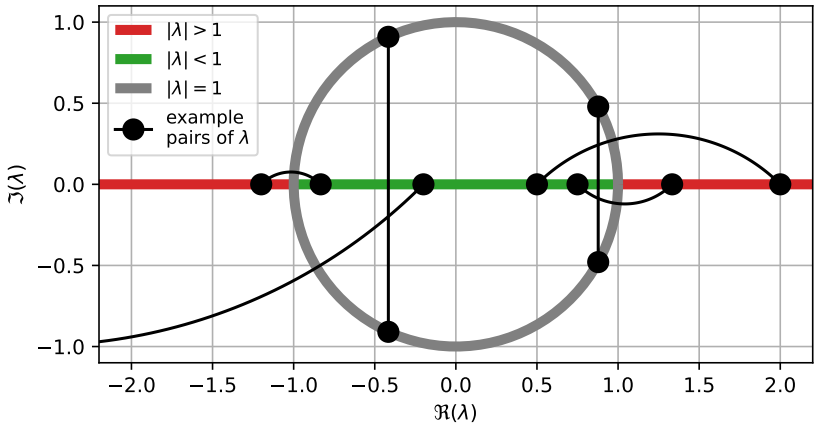

Figure 7.1: All possible positions of eigenvalues λ in the complex plane. The color indicates if the absolute value is above, below, or exactly 1. Some examples for valid pairs of eigenvalues are shown.

The eigenvalues of a square matrix are the roots of its respective characteristic polynomial. Since the monodromy matrix $\mathbf{M}$ is real, so is its characteristic polynomial, which means that all of its eigenvalues are either real or occur in complex conjugated pairs. Furthermore, the specifics of the CR3BP demand the eigenvalues to come in inverse pairs [10]. One of those pairs has to be $(1, 1)$. This is generally true in the CR3BP, and in this specific case it can be explained with the DROs being a family of orbits: A neighboring DRO has a slightly different starting position and starting velocity, but after one

revolution – since it is a closed orbit – those changes remain the same. Therefore, one eigenvalue has to be one. Thus, the eigenvalues are:

$$\lambda_1 = \lambda_2 = 1, \qquad \lambda_3 = \frac{1}{\lambda_4}, \qquad \lambda_5 = \frac{1}{\lambda_6} \tag{7.1}$$

This means λ_3 and λ_4 can either be both real while satisfying Equation (7.1), for example $\lambda_3 = 0.5$ and $\lambda_4 = 2$. Or, they can be both complex, but then need to satisfy Equation (7.1) while at the same time being each other's complex conjugate. This is only possible if they are on the unit circle of the complex plane, for example $\lambda_3 = i$ and $\lambda_4 = -i$ or $\lambda_3 = -0.5 + \sqrt{3}i/2$ and $\lambda_4 = -0.5 - \sqrt{3}i/2$. The same is true for λ_5 and λ_6. Therefore, all of the eigenvalues λ_1 to λ_6 are on the real axis or on the unit circle in the complex plane, which can be seen in Figure 7.1. This figure also shows the relation of two connected eigenvalues (λ_3 and λ_4 or λ_5 and λ_6): If they are on the unit circle, they are each other's complex conjugate and if they are on the real axis they are each other's inverse.

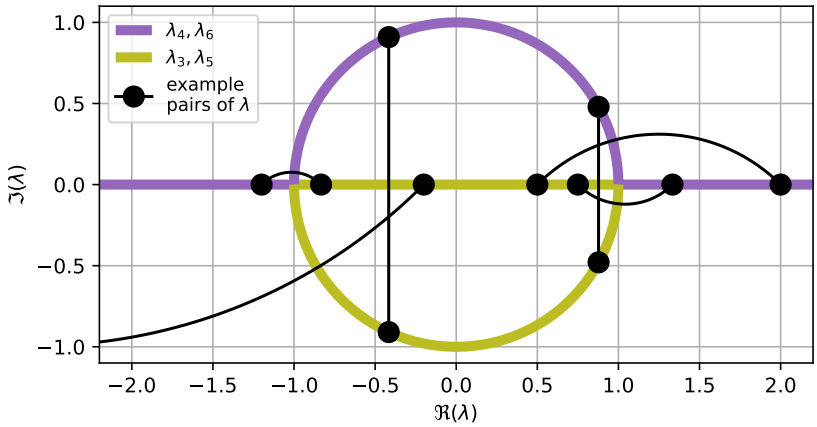

Figure 7.2: All possible positions of eigenvalues λ in the complex plane are divided into two groups, which are shown in green and purple.

The possible values for λ are divided in two different groups; the first being the part of the unit circle with a negative imaginary part $\Im$ and the part of the real axis that has a smaller-than-one absolute value; the second being the part of the unit circle with a positive imaginary part $\Im$ and the part of the real axis that has a greater-than-one absolute value. This becomes more obvious when looking at Figure 7.2 where the first group is colored green while the second group is colored purple. Now, due to the rules for pairs of eigenvalues λ that have been discussed before, a pair of eigenvalues λ (like $\lambda_{1/2}$, $\lambda_{3/4}$ or $\lambda_{5/6}$) always consist of one eigenvalue λ in the first and one in the second group. It should be noted that only the eigenvalue in the second group can have an absolute value that is greater than one and thus implies that the orbit is unstable. Without loss of generality, this chapter makes a few assumptions about the numbering of the eigenvalues λ_1 to λ_6:

- The two eigenvalues λ that are one are λ_1 and λ_2.
- The other two eigenvalues that lie in the xy-plane are λ_3 and λ_4.
- The two eigenvalues that do have non-zero z- and $\dot{z}$-components are λ_5 and λ_6.
- Among $\lambda_{3/4}$ and $\lambda_{5/6}$ the eigenvalues λ that are in the first group are λ_3 and λ_5 – and therefore λ_4 and λ_6 are in the second group.

The reason why there are four eigenvalues λ_1 to λ_4 that have eigenvectors that are in the xy-plane and two eigenvalues λ_5 and λ_6 is that any state with $z = \dot{z} = 0$ leads to the entire orbit fulfilling $z = \dot{z} = 0$, as can be seen in Equation (3.5). Since the DROs are entirely in the xy-plane, the four eigenvalues λ_1 to λ_4 can be obtained by propagating a two-dimensional version of the state transition matrix $\mathbf{\Phi}$ and finding the eigenvalues λ of the resulting monodromy matrix $\mathbf{M}$. For λ_5 and λ_6, the three-dimensional state transition matrix $\mathbf{\Phi}$ has to be used.

7.2. Stability of without Perturbations

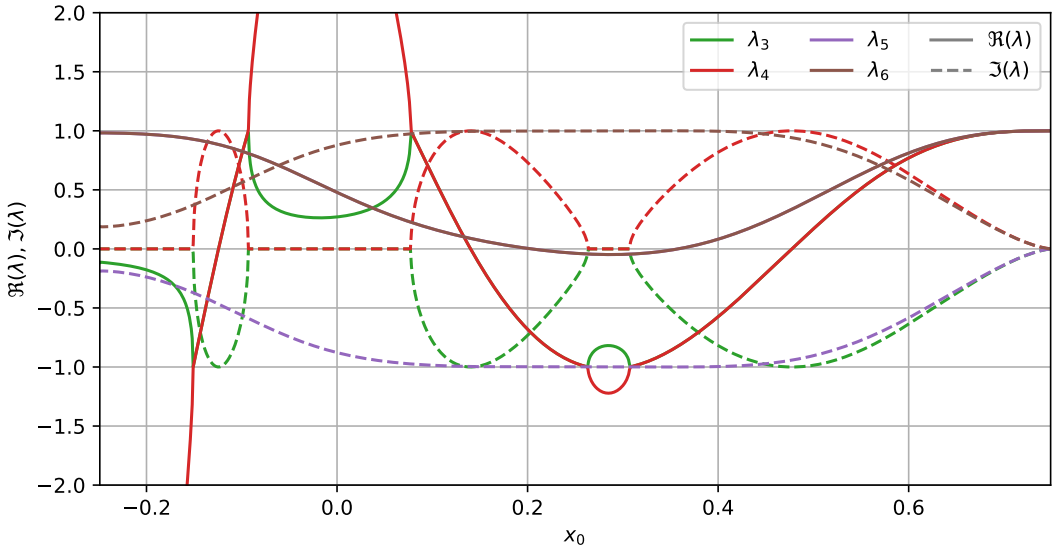

Figure 7.3: The real part $\Re(\lambda)$ and the imaginary part $\Im(\lambda)$ of the four eigenvalues λ_3 to λ_6 of the monodromy matrix $\mathbf{M}$ as a function of the starting position x_0 for $\mu = 0.25$.

Figure 7.3 shows the real part $\Re(\lambda)$ and the imaginary part $\Im(\lambda)$ of the four eigenvalues λ_3 to λ_6 depending on the starting position x_0 for a CR3BP with a specific mass ratio μ. This yields a plot that is quite crowded and badly readable, as it includes eight lines that partly coincide – since always either the real part $\Re(\lambda)$ or the imaginary part $\Im(\lambda)$ of two related eigenvalues λ is the same.

An alternative to this can be found in Figure 7.4, which conveys the same information as Figure 7.3 but with only two lines. One for the two non-trivial in-plane eigenvalues λ_3 and λ_4 and one for the two out-of-plane eigenvalues λ_5 and λ_6. The vertical axis on the left-hand side is dedicated to the two eigenvalues λ_4 and λ_6 in the second group. Those are the ones that are potentially unstable. The vertical axis on the right-hand side is dedicated to the two eigenvalues λ_3 and λ_5 in the first group, which can not be unstable. The plot is divided vertically in three parts: The upper third represents the positive real axis, with values above one on the left-hand side and values below one on the right-hand side. In order to have two related eigenvalues λ be represented by the same line, the left- and right-hand side vertical axes have to be chosen such that their product is always one. Therefore, they are both logarithmic, one ascending, one descending. The same applies to the lower third of the plot, just on the negative side of the real axis. The middle part of the plot is dedicated to the eigenvalues λ on the unit circle of the complex plane. The axes are linear with respect to the angle x that defines the position e^{ix} on the circle. As for the other parts, the product of any value on the left vertical axis and its respective value on the right axis is one; furthermore, they are complex conjugates.

Figure 7.5 shows for every DRO that is in a two-body system with a mass ratio smaller than $\mu = 0.3$ if the absolute values of λ_4 and λ_6 are smaller or greater than one. The green region indicates that both absolute values are smaller than one, and therefore the DRO is stable. It can be seen that the majority of DROs is stable, especially those with a starting positions closer to the secondary than to the primary. DROs that are in the vicinity of the primary are not of interest for this thesis and should be treated as perturbed orbits instead. When comparing Figure 7.4 with Figure 7.5, they obviously coincide for $\mu = 0.25$: For x_0 below approximately -0.15, λ_4 is smaller than -1, as well as for a small region around $x_0 = 0.3$. Between $x_0 = -0.1$ and $x_0 = 0.1$ there is a region where λ_4 is greater than 1. Other than that, both eigenvalues λ_4 and λ_6 are always between -1 and 1.

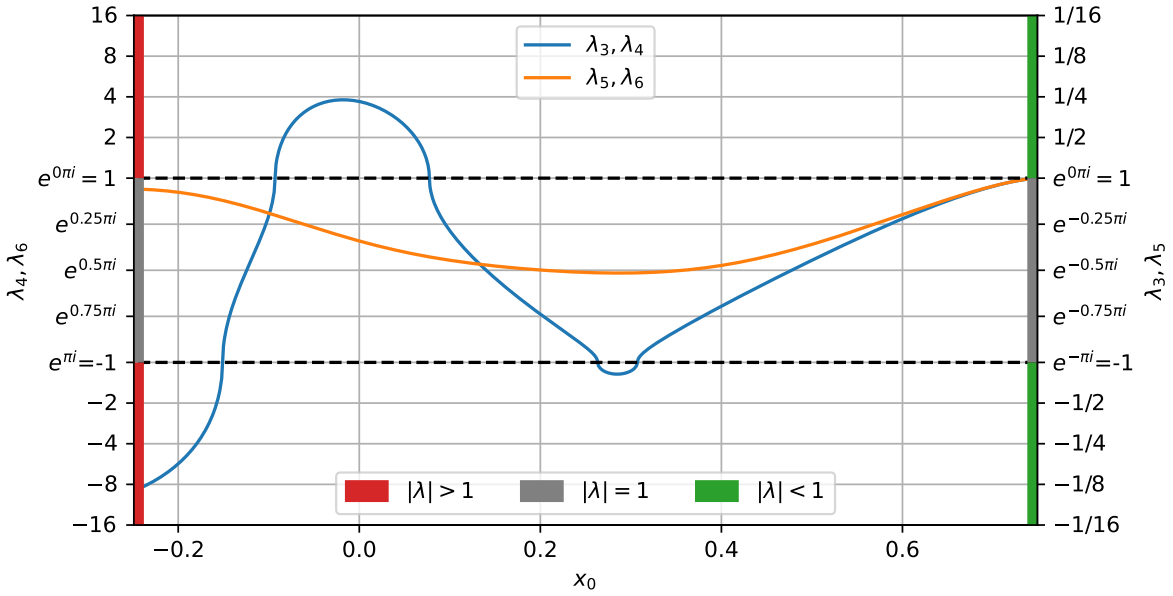

Figure 7.4: The four eigenvalues λ_3 to λ_6 of the monodromy matrix $\mathbf{M}$ as a function of the starting position x_0 for $\mu = 0.25$. The plot is vertically divided in three parts that each has a logarithmic vertical axis or a vertical axis that is linear with the argument (angle) of the complex number on the unit circle. λ_4 and λ_6 can be read from the left axis while λ_3 and λ_5 can be read from the right axis.

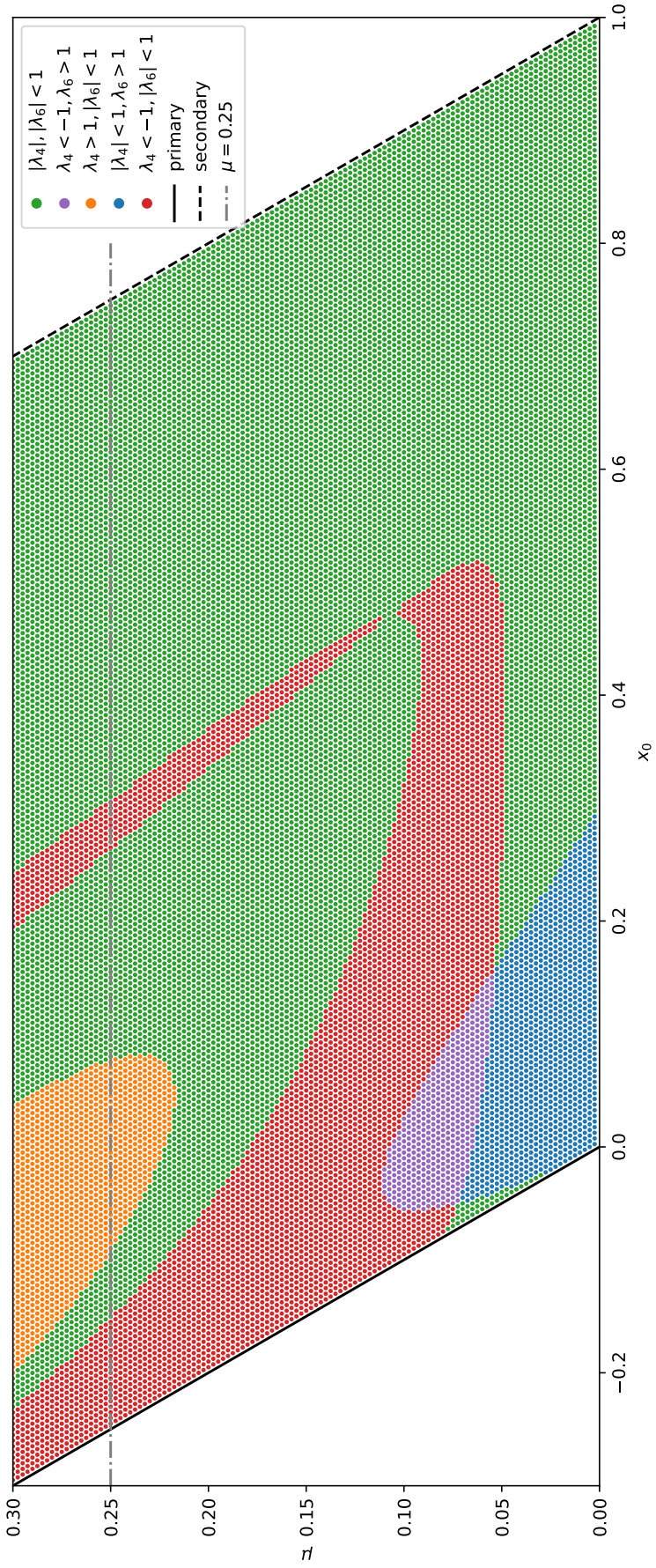

Figure 7.5: Stability of DROs depending on the mass ratio μ and the starting position x_0. The green region represents stable orbits while the other colors indicate different kinds of instability.

7.3. Perturbations in the Earth-Moon System

Table 7.1: Estimations for the maximal direct and relative accelerations related to the most important perturbations for a DRO around the Moon with the starting position $x_0 = x_2 - 0.2$. The relative acceleration is given both in metric units as well as in dimensionless units of the CR3BP. The main body attraction parameters can be found in [50, Appendix B] and the coefficients for Earth's spherical harmonics gravity field can be found in [45].

Source	Min Distance to Source [m]	Max Direct Acceleration [m/s^2]	Max Relative Acceleration [m/s^2]	... in CR3BP [-]
Earth p.m.g.	$3.1 \cdot 10^{8}$	$4.2 \cdot 10^{-3}$	—	—
Moon p.m.g.	$7.7 \cdot 10^{7}$	$8.2 \cdot 10^{-4}$	—	—
Sun p.m.g.	$1.5 \cdot 10^{11}$	$5.9 \cdot 10^{-3}$	$3.7 \cdot 10^{-5}$	$1.3 \cdot 10^{-2}$
s.r.p.	$1.5 \cdot 10^{11}$	$6.1 \cdot 10^{-8}$	$6.1 \cdot 10^{-8}$	$2.2 \cdot 10^{-5}$
Earth $J_{2,0}$	$3.1 \cdot 10^{8}$	$5.9 \cdot 10^{-9}$	$5.9 \cdot 10^{-9}$	$2.2 \cdot 10^{-6}$
Venus p.m.g.	$4.1 \cdot 10^{10}$	$1.9 \cdot 10^{-7}$	$4.3 \cdot 10^{-9}$	$1.6 \cdot 10^{-6}$
Jupiter p.m.g.	$6.3 \cdot 10^{11}$	$3.2 \cdot 10^{-7}$	$4.7 \cdot 10^{-10}$	$1.7 \cdot 10^{-7}$
Mars p.m.g.	$7.8 \cdot 10^{10}$	$7.0 \cdot 10^{-9}$	$8.2 \cdot 10^{-11}$	$3.0 \cdot 10^{-8}$
Mercury p.m.g.	$9.2 \cdot 10^{10}$	$2.6 \cdot 10^{-9}$	$2.7 \cdot 10^{-11}$	$9.7 \cdot 10^{-9}$
Saturn p.m.g.	$1.3 \cdot 10^{12}$	$2.3 \cdot 10^{-8}$	$1.7 \cdot 10^{-11}$	$6.0 \cdot 10^{-9}$
Earth $J_{2,2}$	$3.1 \cdot 10^{8}$	$9.8 \cdot 10^{-12}$	$9.8 \cdot 10^{-12}$	$3.6 \cdot 10^{-9}$
Uranus p.m.g.	$2.7 \cdot 10^{12}$	$7.8 \cdot 10^{-10}$	$2.7 \cdot 10^{-13}$	$9.8 \cdot 10^{-11}$
Neptune p.m.g.	$4.4 \cdot 10^{12}$	$3.6 \cdot 10^{-10}$	$7.6 \cdot 10^{-14}$	$2.8 \cdot 10^{-11}$

There are many different perturbations that could be taken into account. This ranges from third-body perturbations like the Sun's or Jupiter's point mass gravity (p.m.g.) to the spherical harmonics gravity (s.h.g.) fields of the primaries and other factors like the solar radiation pressure (s.r.p.). In order to get an estimate of the sizes of those perturbing forces, a specific DRO has to be assumed. As the most prominent and important example of a two-body system, the Earth-Moon system is chosen (more specifically, the EMLS with $\mu = 0.01$). The distance to the secondary (the Moon) in the starting position is chosen to be $x_0 = x_2 - 0.2$, as this value promises to be very far inside the stable region, according to Figure 7.5. For this specific DRO, approximate maximum values for the most important perturbations can be found in Table 7.1. The table is ordered by the magnitude of the relative acceleration; "relative" meaning after subtracting the acceleration that is exerted by this effect on the Earth-Moon-system itself. The s.r.p. and the s.h.g. effects of Earth have no (or only negligible) impact on the Earth-Moon-system itself, therefore for these perturbations the direct and the relative acceleration is the same. On the other hand, the Earth's and Moon's p.m.g. fields are the primary forces in this system, thus they are not considered perturbations and thus do not have a relative acceleration.

The p.m.g. effects are calculated with the planets' semi-major axes a_p and masses m_p compared to the semi-major axis $a_\oplus$ of Earth. Then, the maximal possible direct acceleration a_a occurs when Earth and the third-body planet are closest to each other, for which the distance $d_\mathrm{p,min}$ can be approximated to be $d_\mathrm{p,min} = |a_\mathrm{p} - a_\oplus|$. Thus, $a_\mathrm{a,max}$ calculates to:

$$a_\mathrm{a,max} = G\frac{m_\mathrm{p}}{d_\mathrm{p,min}^2} \tag{7.2}$$

In order to obtain an indication of the size of the maximum value for the relative acceleration a_r, the spacecraft is assumed to be in front of Earth, as seen from the planet. The largest distance between Earth and spacecraft in this scenario is about 1.2 times the distance $d_{\oplus\mathbb{C}}$ between Earth and Moon (which is approximated with the Moon's semi-major axis). Then, $a_\mathrm{r,max}$ is approximated with:

$$a_\mathrm{r,max} = G\frac{m_\mathrm{p}}{\left(d_\mathrm{p,min} - 1.2 \cdot d_{\oplus\mathbb{C}}\right)^2} - G\frac{m_\mathrm{p}}{d_\mathrm{p,min}^2} = Gm_\mathrm{p}\left(\frac{1}{\left(d_\mathrm{p,min} - 1.2 \cdot d_{\oplus\mathbb{C}}\right)^2} - \frac{1}{d_\mathrm{p,min}^2}\right) \tag{7.3}$$

These equations can also be used for the third-body perturbation caused by the Sun, in this case $a_\mathrm{p} = 0$. This is a very good example of how Table 7.1 makes some simplifying assumptions: Even though the

shortest possible distance between Earth and Sun is indeed a known value, the semi-major axis is used instead, which is of course *not* the shortest possible distance. But for the sake of this table – which is focused on the orders of magnitude rather than the exact values – these simplifications are acceptable.

For the s.r.p., assumptions regarding the spacecraft's mass m and surface area A have to be made. For their similarity with the International Space Station (ISS), $m = 4.4 \cdot 10^5\,\text{kg}$ and $A = 3000\,\text{m}^2$ have been chosen. When assuming the s.r.p. to be $9.08\,\mu\text{Pa}$ at Sun-Earth distance – as suggested in [50, Table B.1] – the acceleration $a_{\text{s.r.p.}}$ resulting from the s.r.p. calculates to:

$$a_{\text{s.r.p.}} = \frac{9.08\,\mu\text{Pa} \cdot A}{m} = \frac{9.08\,\mu\text{Pa} \cdot 3000\,\text{m}^2}{4.4 \cdot 10^5\,\text{kg}} \approx 6 \cdot 10^8\,\frac{\text{m}}{\text{s}^2} \tag{7.4}$$

Yet again, this completely neglects many effects, for example if and at what angle the solar radiation is reflected from the spacecraft. But for the order of magnitude, these considerations would not have a large impact.

The acceleration that is introduced by s.h.g. can be computed with the potential U [12]:

$$U = \frac{Gm_\oplus}{r} \sum_{l=0}^{\infty} \sum_{m=0}^{l} \left(\frac{R_\oplus}{r}\right)^l \bar{P}_{lm}\left(\sin\phi\right)\left(\bar{C}_{lm}\cos m\theta + \bar{S}_{lm}\sin m\theta\right) \tag{7.5}$$

In this equation, $R_\oplus$ is the radius of Earth, r is the spacecraft's distance to the center of Earth, $\bar{P}_{lm}$ refers to normalized associated Legendre polynomials, and $\bar{C}_{lm}$ and $\bar{S}_{lm}$ are the Earth's normalized s.h.g. field coefficients. In order to obtain the acceleration that results from the potential U, its partial derivatives with respect to the spatial directions have to be computed. However – as a simplification – only the radial direction is considered important here. The potential U_{lm} that belongs to degree l and order m is:

$$U_{lm} = \frac{Gm_\oplus R_\oplus^l}{r^{l+1}} \bar{P}_{lm}\left(\sin\phi\right)\left(\bar{C}_{lm}\cos m\theta + \bar{S}_{lm}\sin m\theta\right) \tag{7.6}$$

Therefore, the acceleration a_{lm} in radial direction that results from the s.h.g. of degree l and order m is:

$$a_{lm} = \frac{\partial}{\partial r} U_{lm} = (-l-1)\frac{Gm_\oplus R_\oplus^l}{r^{l+2}} \bar{P}_{lm}\left(\sin\phi\right)\left(\bar{C}_{lm}\cos m\theta + \bar{S}_{lm}\sin m\theta\right) \tag{7.7}$$

Knowing that the normalized associated Legendre polynomials are always between minus one and one, an upper bound for the absolute value of a_{lm} can be found:

$$|a_{lm}| = (l+1)\frac{Gm_\oplus R_\oplus^l}{r^{l+2}} \underbrace{\left|\bar{P}_{lm}(\sin\phi)\right|}_{\leq 1} \underbrace{\left|\bar{C}_{lm}\cos m\theta + \bar{S}_{lm}\sin m\theta\right|}_{\leq \sqrt{\bar{C}_{lm}^2 + \bar{S}_{lm}^2}} \leq (l+1)\frac{Gm_\oplus R_\oplus^l}{r^{l+2}} \sqrt{\bar{C}_{lm}^2 + \bar{S}_{lm}^2} \tag{7.8}$$

This formula is used to compute approximate upper bounds for $a_{2,0}$ and $a_{2,2}$ in Table 7.1. These are the two with the strongest effects on DROs.

A note on the last column of Table 7.1: The dimensionless acceleration in the CR3BP is directly proportional to the relative acceleration (in fact, it *is* the relative acceleration, just with a different unit). The distance 1 in the CR3BP is the distance between Earth and Moon, which is about $384\,400\,000\,\text{m}$ [34]. The time 2π in the CR3BP is the (sidereal) period of the Moon's orbit, which is about 27.3217 days [34]. Therefore, to translate a relative acceleration in m/s^2 into dimensionless CR3BP units, it has to be adjusted by a factor.

This all being said, it should be stressed again that in Table 7.1 only the order of magnitude is of interest, not the values themselves. From the table it can be concluded that the Sun's p.m.g. is the most severe perturbing factor by far – the second most important one is the s.r.p. which is three orders of magnitude smaller. The relative acceleration arising due to the Sun's p.m.g. is quite complex and varies depending on the position in both strength and direction. For the sake of simplicity, in this chapter only

a constant acceleration with a constant angle is investigated. This is meant to be a very first estimate of the consequences of the Sun's p.m.g. on the stability of DROs. However, the insights are quite limited. This is not so much because the relative acceleration due to the Sun's p.m.g. changes with the position in the CR3BP – since a DRO with starting position $x_0 = x_2 - 0.2$ is small and therefore the differences are not large. The more severe discrepancy between the Sun's p.m.g. and the perturbation model in this chapter is the time-dependency of the Sun's p.m.g. that is not modeled here. Even a weak perturbation can cause instabilities if it is of periodic nature. Therefore, the results from the next sections can only be understood as a very first and rather theoretical estimation of the influence of the Sun's p.m.g..

7.4. Initial Conditions with Perturbations

The perturbation is modeled as an external acceleration in the xy-plane, constant in magnitude and direction. This can easily be implemented by altering the potential U from Equation (3.8).

$$U = \underbrace{\frac{1}{2}(x^2+y^2) + \frac{1-\mu}{r_1} + \frac{\mu}{r_2}}_{\text{CR3BP}} \underbrace{+a_x x + a_y y}_{\substack{\text{external} \\ \text{acceleration}}} \tag{7.9}$$

This being said, the question arises if the initial conditions that had been calculated in Chapter 4 are still valid. By definition they are not, since this perturbed circular restricted three-body problem (PCR3BP) does not have the symmetry that the CR3BP had. Therefore, the x-axis crossings are not necessarily perpendicular to the x-axis anymore. This means that the differential corrector has to be applied in a different way, as the implementation in Section 3.4 was exploiting this fact. Now, there is no condition that the DRO would have to satisfy after half an orbit, therefore an entire revolution has to be regarded. Similar to Section 3.4, an initial guess $\mathbf{X}_0$ for the state $\mathbf{X}(0)$ is needed, whereas this time, it is allowed to have a velocity component $\dot{x}_0$in x-direction:

$$\mathbf{X}_0 = \begin{bmatrix} x_0 & 0 & \dot{x}_0 & \dot{y}_0 \end{bmatrix}^\mathsf{T} \tag{7.10}$$

This is propagated until the x-axis is crossed a second time – after one revolution. Then, state $\mathbf{X}_1$ and state transition matrix $\mathbf{\Phi}_1$ are:

$$\mathbf{X}_1 = \begin{bmatrix} x_1 & 0 & \dot{x}_1 & \dot{y}_1 \end{bmatrix}^\mathsf{T}, \qquad \mathbf{\Phi}_1 = \mathbf{\Phi}(t_1, t_0) = \frac{\partial \mathbf{X}_1}{\partial \mathbf{X}_0} = \begin{bmatrix} \Phi_{1,1} & \Phi_{1,2} & \Phi_{1,3} & \Phi_{1,4} \\ \Phi_{2,1} & \Phi_{2,2} & \Phi_{2,3} & \Phi_{2,4} \\ \Phi_{3,1} & \Phi_{3,2} & \Phi_{3,3} & \Phi_{3,4} \\ \Phi_{4,1} & \Phi_{4,2} & \Phi_{4,3} & \Phi_{4,4} \end{bmatrix} \tag{7.11}$$

The state change $\Delta\mathbf{X}_1$ after one orbit resulting from the state change $\Delta\mathbf{X}_0$ is then:

$$\Delta\mathbf{X}_1 = \mathbf{\Phi}_1 \Delta\mathbf{X}_0 + \Delta t \dot{\mathbf{X}}_1 \tag{7.12}$$

$$\begin{bmatrix} \Delta x_1 \\ \Delta y_1 \\ \Delta \dot{x}_1 \\ \Delta \dot{y}_1 \end{bmatrix} = \begin{bmatrix} \Phi_{1,1} & \Phi_{1,2} & \Phi_{1,3} & \Phi_{1,4} \\ \Phi_{2,1} & \Phi_{2,2} & \Phi_{2,3} & \Phi_{2,4} \\ \Phi_{3,1} & \Phi_{3,2} & \Phi_{3,3} & \Phi_{3,4} \\ \Phi_{4,1} & \Phi_{4,2} & \Phi_{4,3} & \Phi_{4,4} \end{bmatrix} \begin{bmatrix} \Delta x_0 \\ \Delta y_0 \\ \Delta \dot{x}_0 \\ \Delta \dot{y}_0 \end{bmatrix} + \Delta t \begin{bmatrix} \dot{x}_1 \\ \dot{y}_1 \\ \ddot{x}_1 \\ \ddot{y}_1 \end{bmatrix} \tag{7.13}$$

Yet again, these are four equations with nine unknowns. This time the state $\mathbf{X}_1$ after one orbit should be exactly the same as the state $\mathbf{X}_0$ in the beginning. This condition gives the four equations:

$$\begin{cases} x_1 + \Delta x_1 = x_0 + \Delta x_0 \\ y_1 + \Delta y_1 = y_0 + \Delta y_0 \\ \dot{x}_1 + \Delta \dot{x}_1 = \dot{x}_0 + \Delta \dot{x}_0 \\ \dot{y}_1 + \Delta \dot{y}_1 = \dot{y}_0 + \Delta \dot{y}_0 \end{cases} \tag{7.14}$$

No change should be applied to the initial position, therefore $\Delta x_0 = \Delta y_0 = 0$. This yields:

$$\begin{cases} \Delta x_1 = x_0 - x_1 \\ \Delta y_1 = y_0 - y_1 \\ \Delta \dot{x}_1 = \dot{x}_0 - \dot{x}_1 + \Delta \dot{x}_0 \\ \Delta \dot{y}_1 = \dot{y}_0 - \dot{y}_1 + \Delta \dot{y}_0 \end{cases} \tag{7.15}$$

These equations can be plugged into Equation (7.13), while at the same time setting $\Delta x_0 = \Delta y_0 = 0$:

$$\begin{bmatrix} x_0 - x_1 \\ y_0 - y_1 \\ \dot{x}_0 - \dot{x}_1 + \Delta\dot{x}_0 \\ \dot{y}_0 - \dot{y}_1 + \Delta\dot{y}_0 \end{bmatrix} = \begin{bmatrix} \Phi_{1,3} & \Phi_{1,4} \\ \Phi_{2,3} & \Phi_{2,4} \\ \Phi_{3,3} & \Phi_{3,4} \\ \Phi_{4,3} & \Phi_{4,4} \end{bmatrix} \begin{bmatrix} \Delta\dot{x}_0 \\ \Delta\dot{y}_0 \end{bmatrix} + \Delta t \begin{bmatrix} \dot{x}_1 \\ \dot{y}_1 \\ \ddot{x}_1 \\ \ddot{y}_1 \end{bmatrix} \tag{7.16}$$

This seems to be an over-determined system of linear equations, as there are now four equations for only three unknowns. However, also in the PCR3BP there is a constant (like the Jacobi constant in the CR3BP), which guarantees that if after one orbit both position components and one velocity component are the same, then also the second velocity component has to be the same, which is derived in Appendix D. This only holds for its absolute value, meaning that theoretically it would be possible that one of the velocity components has its sign flipped; however, this did not actually happen in the simulations. Therefore, it is sufficient to fulfill the first three equations of Equation (7.16), and the fourth one will be fulfilled automatically. The first three equations can be written as:

$$\begin{bmatrix} x_0 - x_1 \\ y_0 - y_1 \\ \dot{x}_0 - \dot{x}_1 \end{bmatrix} = \begin{bmatrix} \Phi_{1,3} & \Phi_{1,4} & \dot{x}_1 \\ \Phi_{2,3} & \Phi_{2,4} & \dot{y}_1 \\ \Phi_{3,3} - 1 & \Phi_{3,4} & \ddot{x}_1 \end{bmatrix} \begin{bmatrix} \Delta\dot{x}_0 \\ \Delta\dot{y}_0 \\ \Delta t \end{bmatrix} \tag{7.17}$$

This system of linear equations can easily be solved numerically and yields the changes $\Delta\dot{x}_0$ and $\Delta\dot{y}_0$ that need to be applied to the initial state $\mathbf{X}_0$. As before, this procedure can be repeated until the residual is sufficiently small.

7.5. Stability with Perturbations

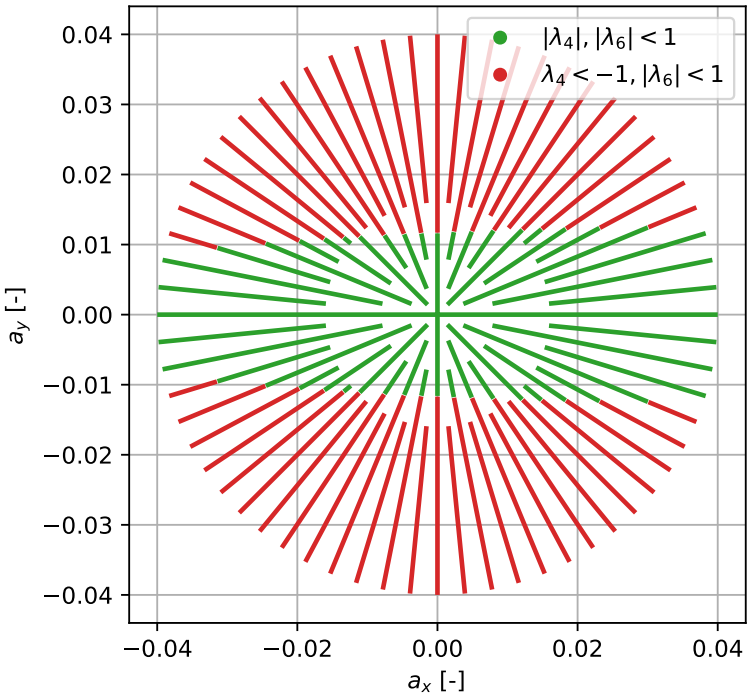

Figure 7.6: Stable (green) and unstable (red) regions when applying an external force a with components a_x and a_y to the DRO that starts at $x_0 = x_2 - 0.2$. $\mu = 0.0121$.

To investigate the stability of perturbed DROs, a specific DRO in the Earth-Moon system has been chosen. As in Section 7.3, this is the DRO with starting position $x_0 = x_2 - 0.2$. A force has been applied to this DRO which is expressed as an external acceleration with the components a_x and a_y. Figure 7.6 shows that the stability of the resulting DRO does not only depend on the strength of the external acceleration, but also on its direction. An external acceleration in x-direction has a smaller effect than one in

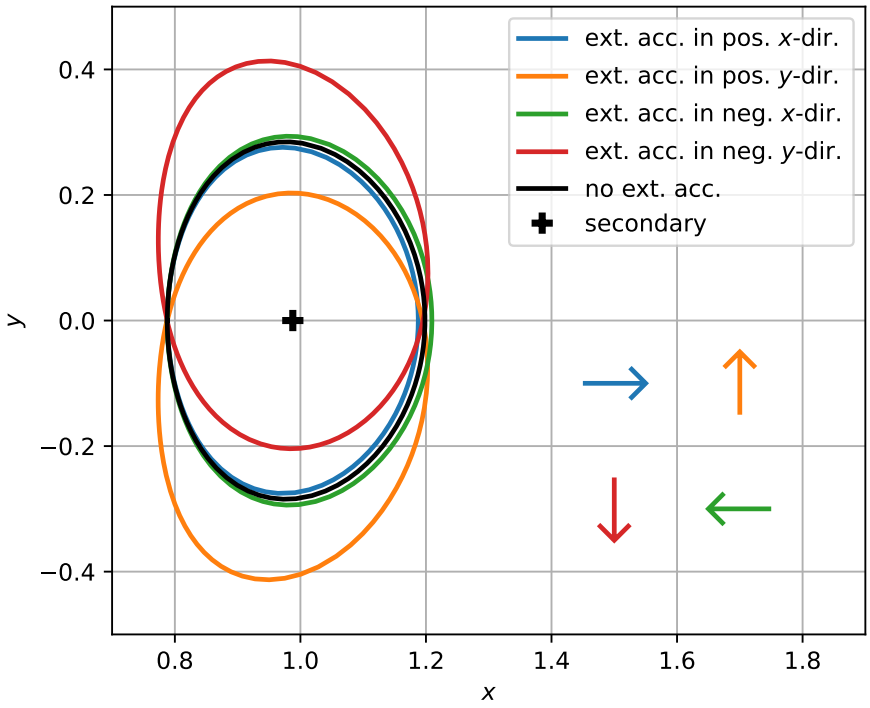

Figure 7.7: DROs with $x_0 = x_2 - 0.2$ in the PCR3BP with an external acceleration of 0.02. The direction of the external acceleration is indicated by the arrows. $\mu = 0.0121$.

y-direction. If the acceleration exceeds 0.01 in y-direction (in dimensionless PCR3BP coordinates), the DRO is bound to become unstable, while a DRO that is subject to an acceleration of 0.04 in x-direction is still stable. This is possibly related to the symmetry of the CR3BP that is disturbed by the y-direction acceleration, but not by the x-direction acceleration. Furthermore, DROs that are disturbed in x-direction do not change as much as DROs that are disturbed in y-direction. This can be seen in Figure 7.7: While the green and the blue DRO are very similar to the unperturbed black one, the orange and the red DRO are shifted significantly in y-direction. Also the direction of the shift is interesting: All four DROs are shifted into the opposite direction of the external acceleration. This can be explained easily by taking the red DRO (external acceleration in negative y-direction) as an example: At the force-facing side of the DRO – thus on the top side of Figure 7.7 – the external force is "pushing" the object towards the secondary, which adds to the gravitational acceleration that is caused by the secondary. In order to compensate for this, the DRO is farther away from the secondary than the unperturbed version. On the other hand, at the force-averted side of the DRO – thus at the bottom of Figure 7.7 – the external force is directed away from the secondary, canceling out some of the secondary's gravitational attraction. This is compensated by a smaller distance to the secondary, which makes its gravitational attraction larger. As a result, the orbit moves against the direction of the external acceleration.

Figure 7.8 compares the values for the external acceleration for which the DRO is still stable with the two strongest perturbations from Table 7.1. It is apparent that the strength of the s.r.p. as the second largest perturbation is by far not enough to make the DRO unstable. Only the p.m.g. of the Sun could cause instabilities. However – as mentioned before – this only tells something about a constant force with a constant direction. All of the listed perturbations revolve around the Earth-Moon system which can alter their effect. In order to determine their true effect on the stability of DROs, further research is necessary. At this point, also the non-circular character of the orbits of primary and secondary has not been taken into account yet.

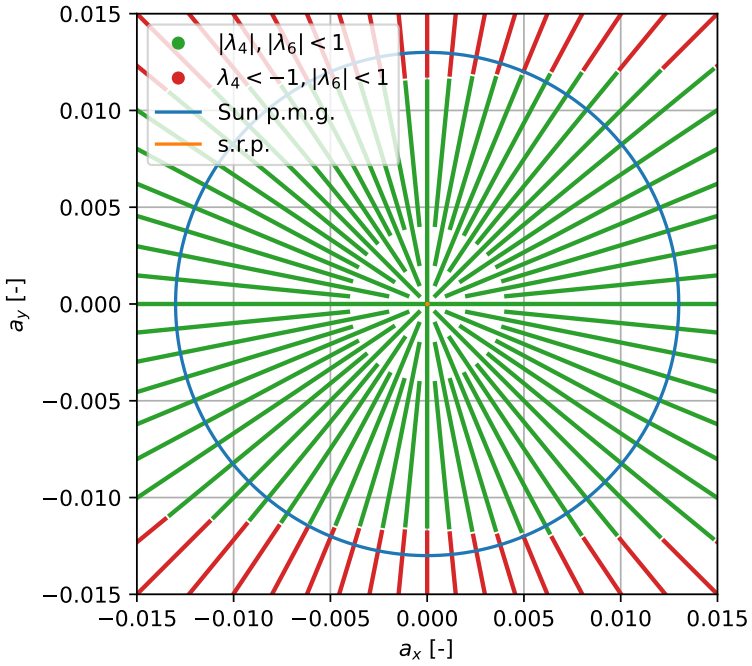

Figure 7.8: Stable (green) and unstable (red) regions when applying an external force a with components a_x and a_y to the DRO that starts at $x_0 = x_2 - 0.2$. The blue circle represents the maximal value for the relative acceleration due to the p.m.g. of the Sun and the (very small) orange circle in the center (radius $2.2 \cdot 10^{-5}$, as written in Table 7.1) represents the maximal value for the s.r.p.. $\mu = 0.0121$.

8

Verification and Validation

In order to verify the proper functioning of the implementation of the CR3BP and the differential corrector, they are used to reproduce the initial conditions for an L_1-Lyapunov orbit in the Sun-Earth system. In [1] the initial conditions for an L_1-Lyapunov orbit in a CR3BP with the mass ratio

$$\mu = 3.001348389698916 \cdot 10^{-6} \tag{8.1}$$

are given to be [1, Table 2]:

$$\begin{cases} x_0 = 0.9870554733155437 \\ \dot{y}_0 = 0.0245251097803396 \end{cases} \tag{8.2}$$

Running the implemented differential corrector algorithm with

$$\begin{cases} x_0 = 0.9870554733155437 \\ \dot{y}_0 = 0.025 \end{cases} \tag{8.3}$$

yields after six iterations:

$$\begin{cases} x_0 = 0.9870554733155437 \\ \dot{y}_0 = 0.0245251097802778 \end{cases} \tag{8.4}$$

Therefore, the initial velocity $\dot{y}_0$ that is obtained with the author's own implementation coincides with the solution from [1] in eleven significant figures, which verifies the proper functioning of both the implementation of the CR3BP and the differential corrector. It should be mentioned that the algorithms for obtaining initial conditions for L_1-Lyapunov orbits and for DROs are the same, just a different initial velocity $\dot{y}_0$ has to be used. In this case, if $\dot{y}_0 = 0.03$ is applied instead of Equation (8.3), the outcome is a DRO. Both, the DRO and the L_1-Lyapunov orbit can be seen in Figure 8.1. A comparison between Figures 8.1 and 8.2 shows that the shapes of the two L_1-Lyapunov orbits are the same. As it was already implied in other chapters, the advantage that DROs have compared to L_1-Lyapunov orbits is their stability, which is advantageous for long-term missions. For example, the DRO in Figure 8.1 is stable while the L_1-Lyapunov orbit has two unstable eigenvalues: $\lambda_4 = 491.6$ and $\lambda_6 = 1.6$. This is using the convention for the numbering of eigenvalues that has been introduced in Section 7.1. It means that any state change in the direction of the eigenvector that belongs to λ_4 is multiplied by 491.6 *every orbit*. Obviously, this would require a lot of orbital station-keeping making this L_1-Lyapunov orbit highly unattractive for long-term missions.

Verification of the implementation of the Fourier series (in the xy-coordinate system) and the polynomial has already been done in Section 6.1, by comparing the author's own results with the ones from [17].

The validation of DROs is not possible, as until recently it has never been performed (see Chapter 2). For the DRO that the service module of the *Chang'e-5* mission performed, no orbit data are available yet.

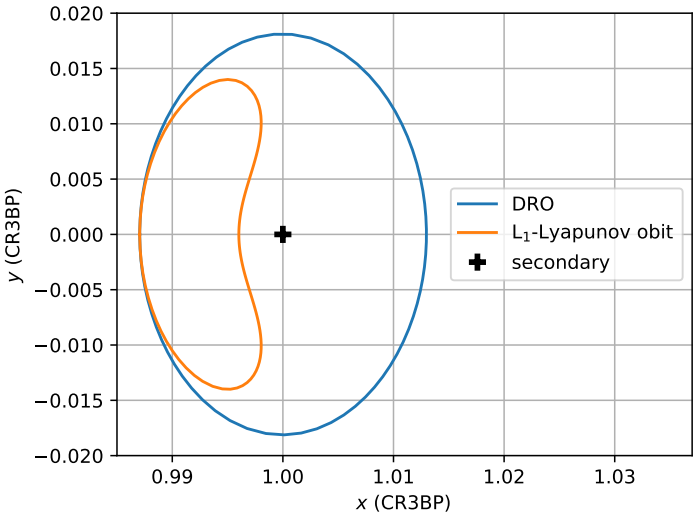

Figure 8.1: DRO and L_1-Lyapunov orbit. In both cases the initial velocity $\dot{y}$ has been determined with the differential corrector. $\mu = 3.001348389698916 \cdot 10^{-6}$.

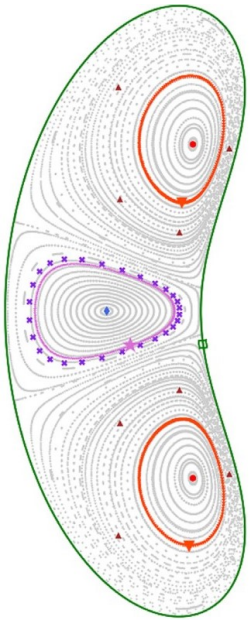

Figure 8.2: DRO in green. Taken from [1, Figure 9]. $\mu = 3.001348389698916 \cdot 10^{-6}$.

9

Conclusions and Recommendations

The research that has been done for this thesis project can roughly be divided in two parts: Chapters 4 and 5 prepare the theoretical knowledge that is necessary for Chapters 6 and 7. Therefore, the insights from Chapters 4 and 5 are mainly important for this thesis itself while conclusions and recommendations arising from Chapters 6 and 7 are summarized in the next sections.

9.1. Modeling with Fourier Series

This thesis project found a novel way of modeling DROs that requires less parameters in order to obtain a higher accuracy than the traditional approach presented in [17]. This is achieved by exploiting specific knowledge about the shape of DROs: In rough approximation, DROs are ellipses with a two-to-one aspect ratio that bend around the primary. By using this information, it was possible to find a parametrization $c(\psi)$ that shows less variability than that of the parametrization $x(\phi)$, $y(\phi)$ in the traditional approach. This function $c(\psi)$ is modeled with a Fourier series (whose parameters are modeled with a polynomial depending on x_0), which yields the novel model of DROs. It gives analytical expressions for position and velocity within a family of DROs, together with analytical expressions for their derivatives. This is important for mission design, as pointed out in [17].

9.2. Stability

In order to be able to evaluate which DROs would be suitable target orbits for asteroid retrieval missions or space hubs for interplanetary travel, the stability of DROs was analyzed. The stability of DROs is the best argument for them, as it differentiates them from the other orbits in two-body systems. An overview over which of the DROs in a two-body system with any mass ratio μ are stable was created in Figure 7.5. It shows that for mass ratios μ that are smaller than 0.05 – which is true for all Solar System Planet-Moon systems, as can be seen in Figure 3.2 – DROs are always stable if the starting position x_0 fulfills $x_0 > 0.3 - \mu$. If the DRO does not fulfill this inequality, it is better modeled as an elliptic orbit around the primary, with the secondary as perturbation, as can be observed in Figure 3.5.

Figure 7.5 only considers unperturbed orbits in the perfect CR3BP environment. Unfortunately, reality is not that simple. Usually, primary and secondary do not revolve around each other in perfect circles; furthermore, the third body is usually subject to various perturbations, of which the most important ones (for a satellite in an Earth-Moon DRO) are listed in Table 7.1. By far the largest perturbation in this table is the Sun's p.m.g., followed by the s.r.p.. In order to get a feeling for the implications of perturbations on the stability of DROs, a constant external acceleration is implemented. It shifts the position of the DRO against the direction of the external acceleration, as can be seen in Figure 7.7. With this idealized version of a real Earth-Moon DRO, the perturbing force introduced by the Sun's p.m.g. is or is not strong enough to make the orbit unstable depending on the direction, as can be seen in Figure 7.8. However, this is not an excellent representation of the Sun's p.m.g. as perturbation, as this would be changing with both time and position.

As for future recommendations, it is clear that the analysis on the stability of DROs should be extended in order to better represent the perturbations, especially the Sun's p.m.g.. Furthermore, the eccentricity of the Moon's orbit around Earth has not been taken into account. The implications of this are not investigated at all in this thesis project and can be analyzed by incorporating the ephemeris of Earth and Moon into the calculations. This would require an entirely different approach than the one presented in this work as firstly, it makes the use of the CR3BP impossible and secondly, it makes the use of the monodromy matrix impossible, as the DROs will not be closed orbits anymore.

9.3. Answers to Research Question

The research question that was posed in Chapter 1 asked what investigations would be needed in order to do the orbit design for a future DRO mission. The first sub-question asked how DROs can be modeled efficiently in order to make the planning of missions that include DROs easier. This has been answered in Section 9.1: A more efficient way of modeling DROs than the one presented in [17] was found. It gives analytic expressions for position and velocity in a family of orbits, which is important for mission design.

The second sub-question asked what DROs would be stable enough to be interesting for future missions. The research shows, that virtually all DROs that can be considered are stable. However, this does not take perturbations into account, which could only be analyzed in a very limited way. Therefore, in order to give an educated answer to this sub-question, more research is necessary, possibly involving the ephemeris of some Solar System bodies.

With this it is possible to answer the main research question. The first step for orbit design is to identify suitable DROs depending on the respective two-body system. Those are typically stable orbits, for which the preliminary analysis in this thesis helps. However, a more thorough analysis for the long-term stability is appropriate. The second step is to find a suitable transfer orbit to the identified range of stable DROs, for which the modeling with Fourier series that has been done in this thesis can be of help.

A

Supporting Material for Initial Conditions

Figures A.1 to A.4 show different zooms into Figure 4.17. Figures A.5 to A.7 depict Figure 4.19 for other mass ratios μ.

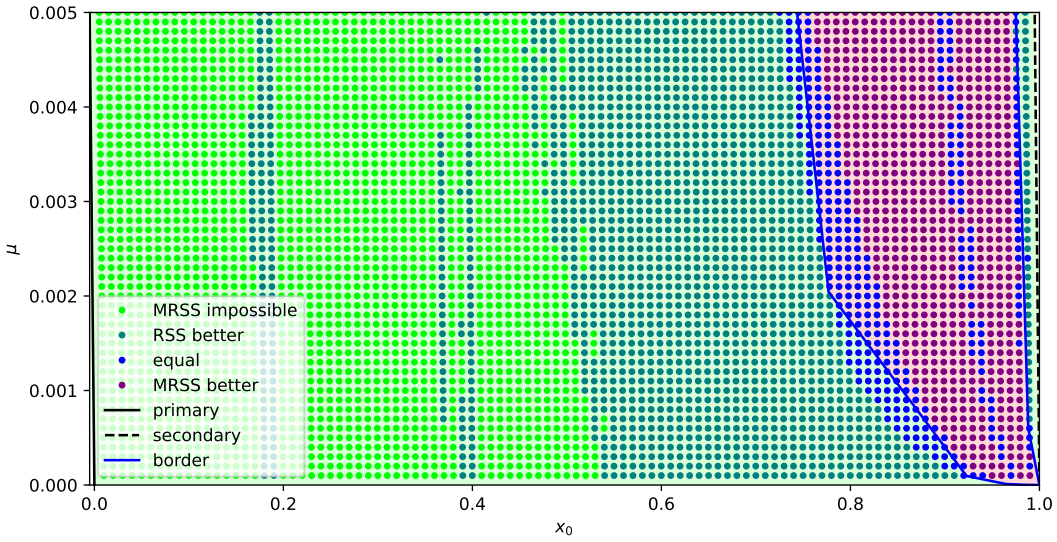

Figure A.1: Zoom into Figure 4.17.

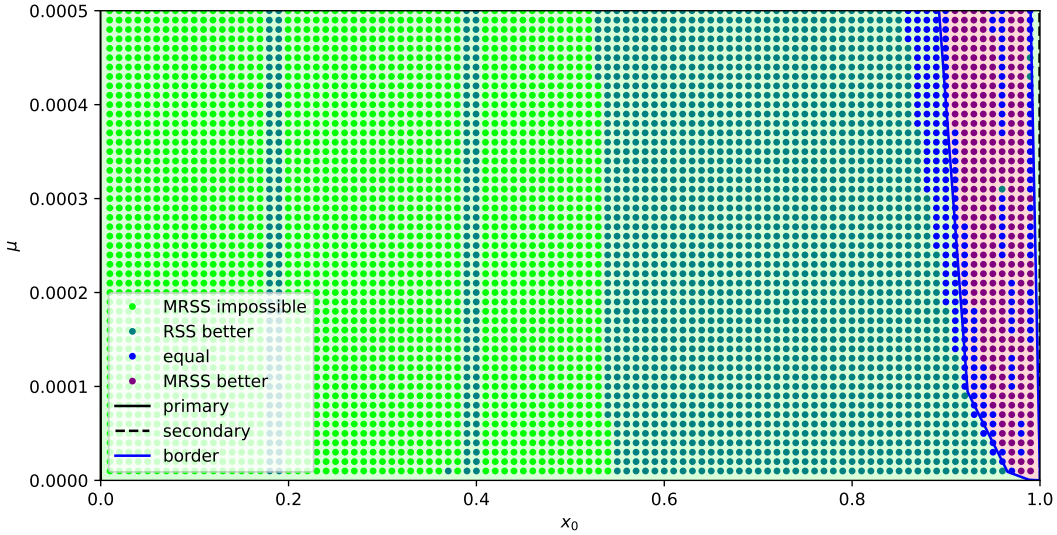

Figure A.2: Zoom into Figure 4.17.

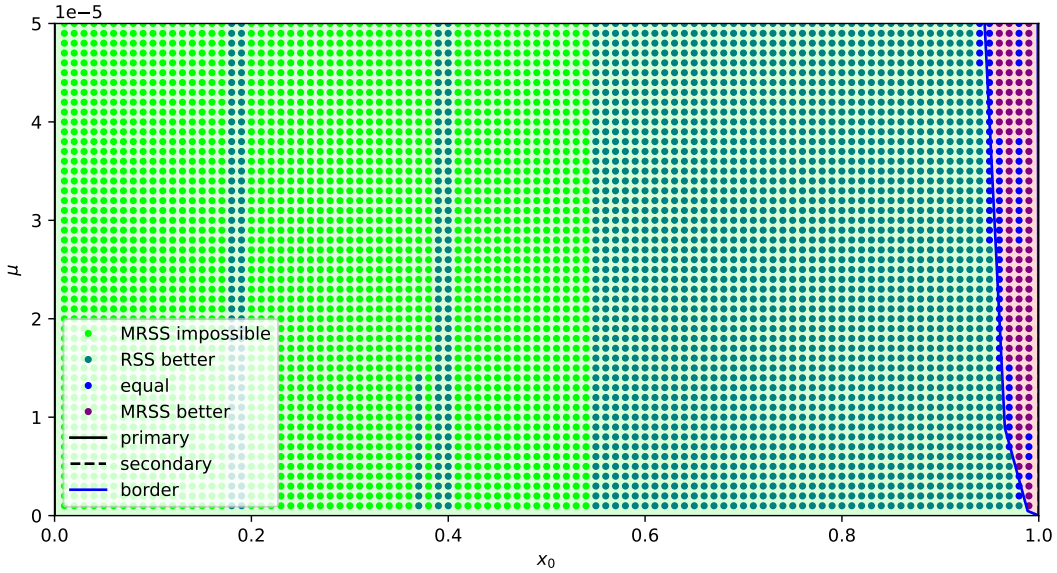

Figure A.3: Zoom into Figure 4.17.

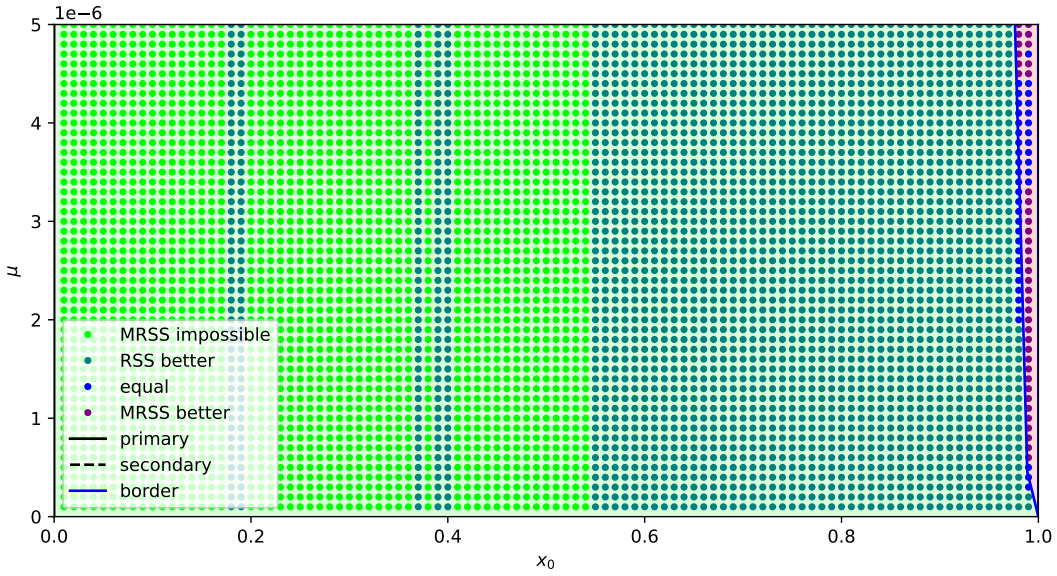

Figure A.4: Zoom into Figure 4.17.

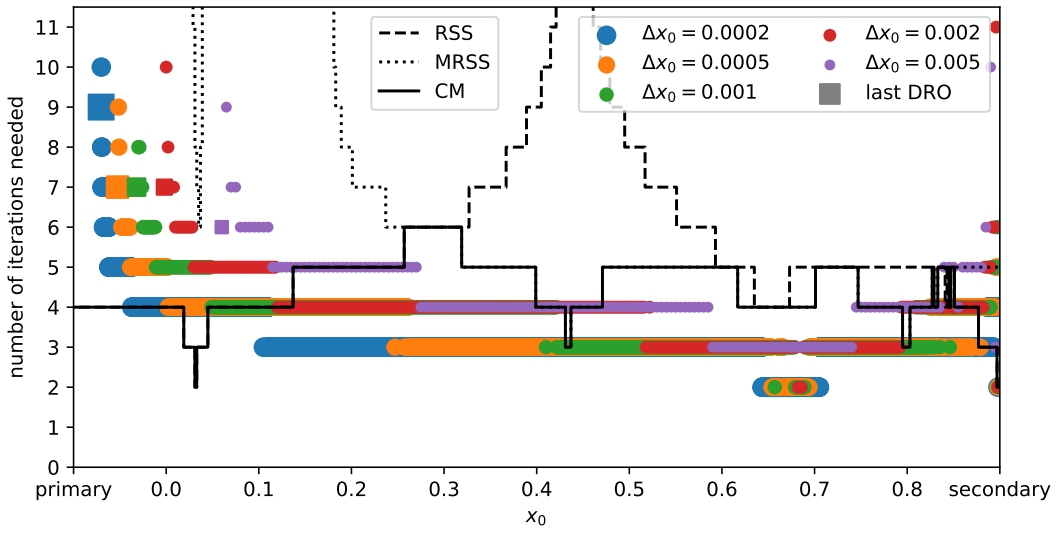

Figure A.5: Figure 4.19 for $\mu = 0.1$.

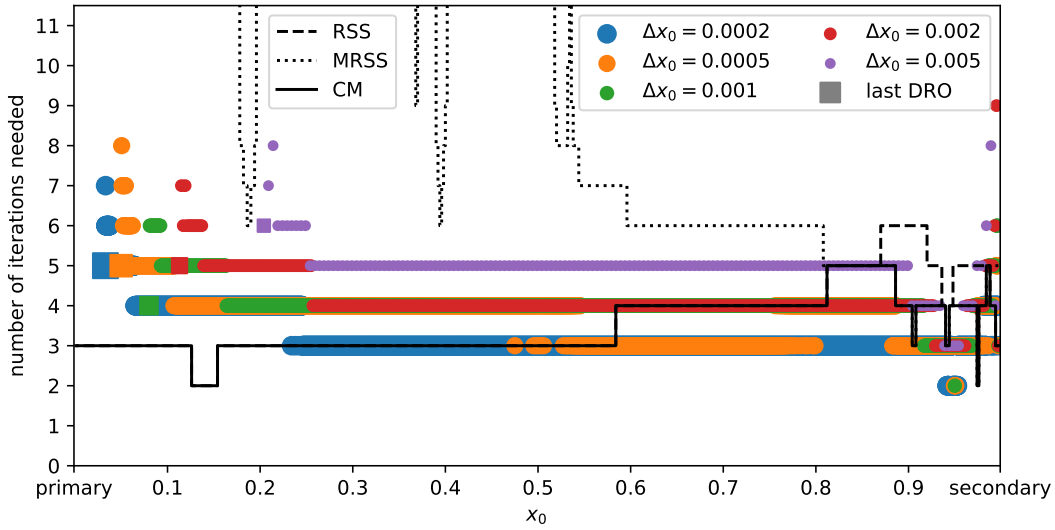

Figure A.6: Figure 4.19 for $\mu = 0.001$.

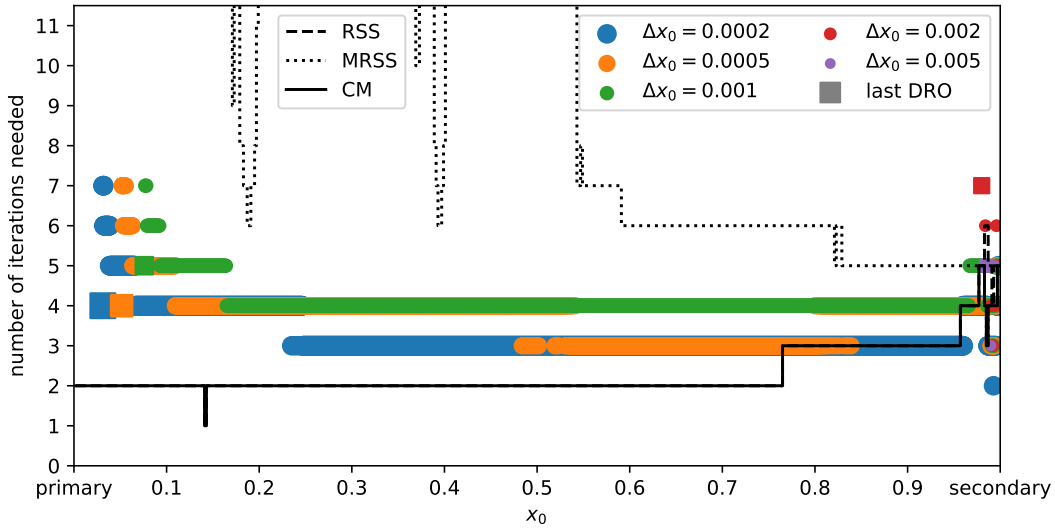

Figure A.7: Figure 4.19 for $\mu = 3 \cdot 10^{-6}$.

B

Supporting Material for Integrator Settings

In this appendix, Figures 5.13 to 5.15 are depicted for various other mass ratios μ.

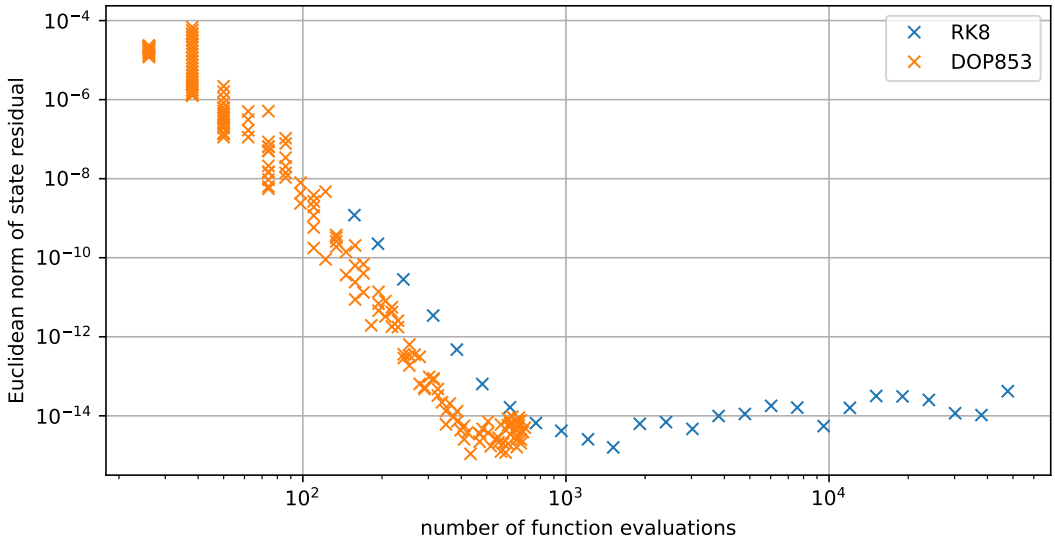

Figure B.1: Figure 5.13 for $\mu = 3 \cdot 10^{-6}$ (SELS).

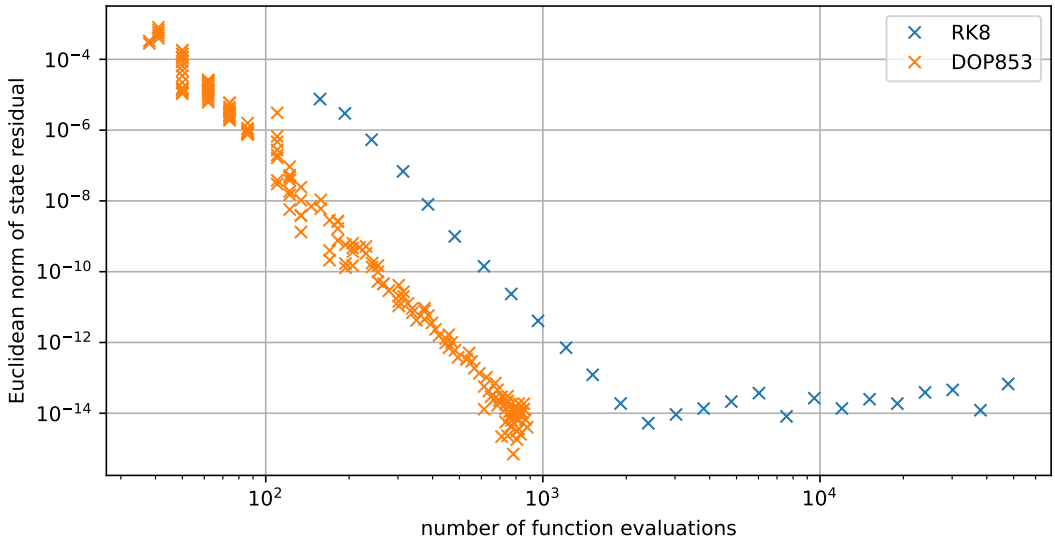

Figure B.2: Figure 5.14 for $\mu = 3 \cdot 10^{-6}$ (SELS).

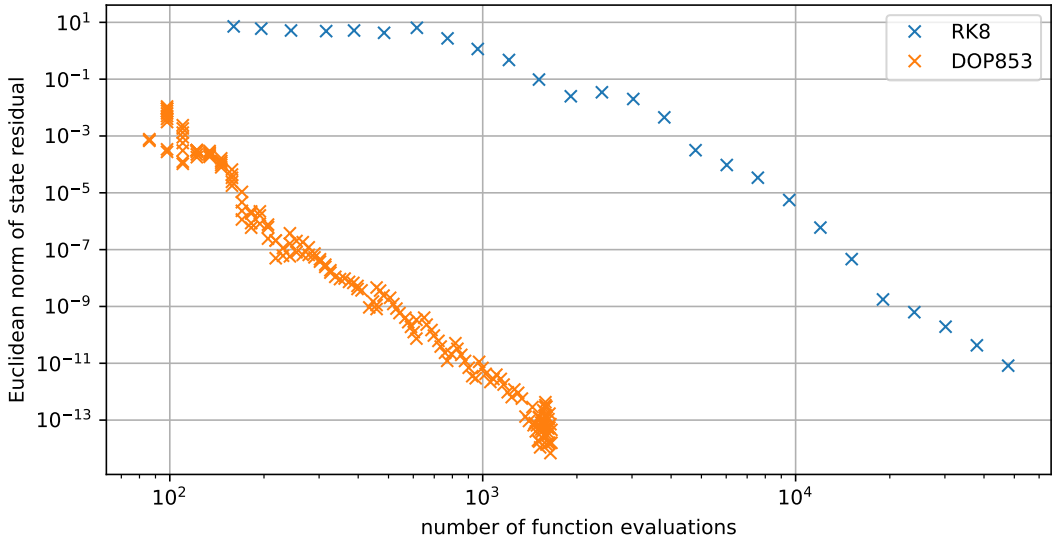

Figure B.3: Figure 5.15 for $\mu = 3 \cdot 10^{-6}$ (SELS).

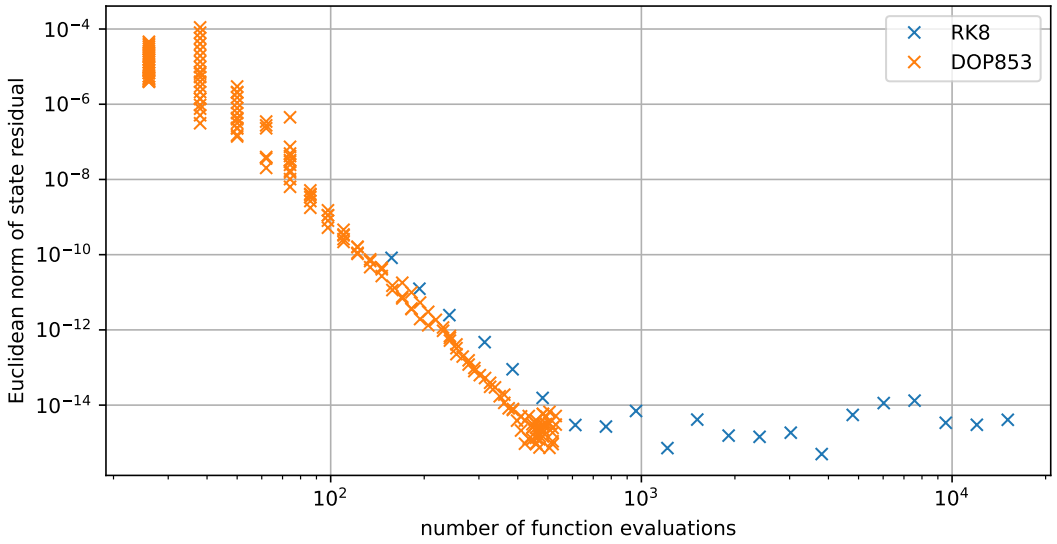

Figure B.4: Figure 5.13 for $\mu = 0.001$ (SJLS).

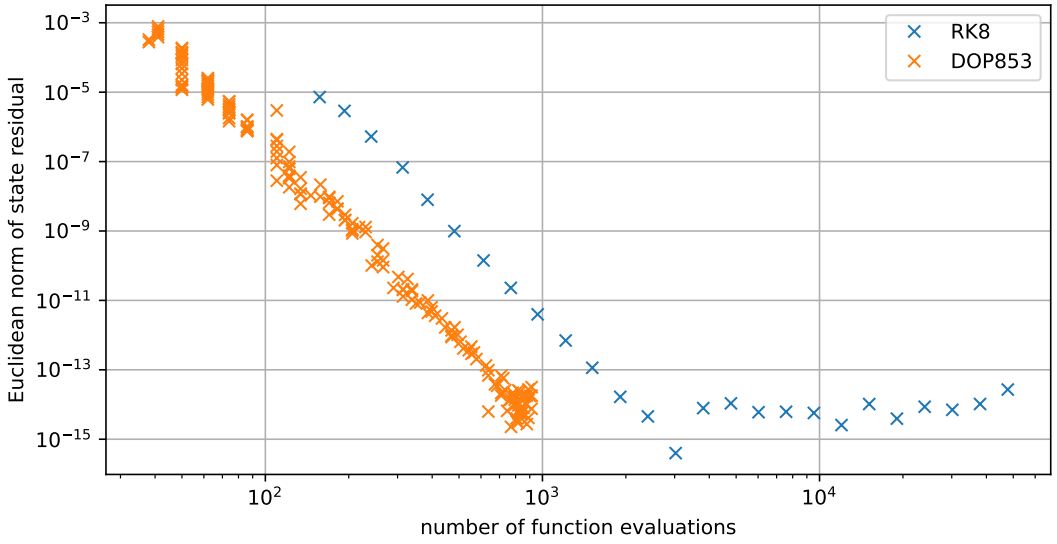

Figure B.5: Figure 5.14 for $\mu = 0.001$ (SJLS).

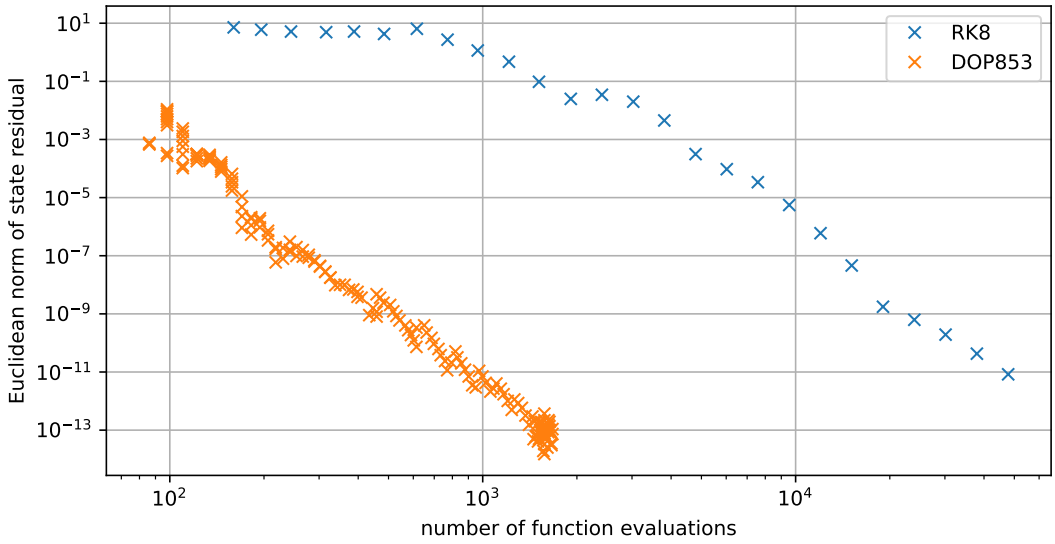

Figure B.6: Figure 5.15 for $\mu = 0.001$ (SJLS).

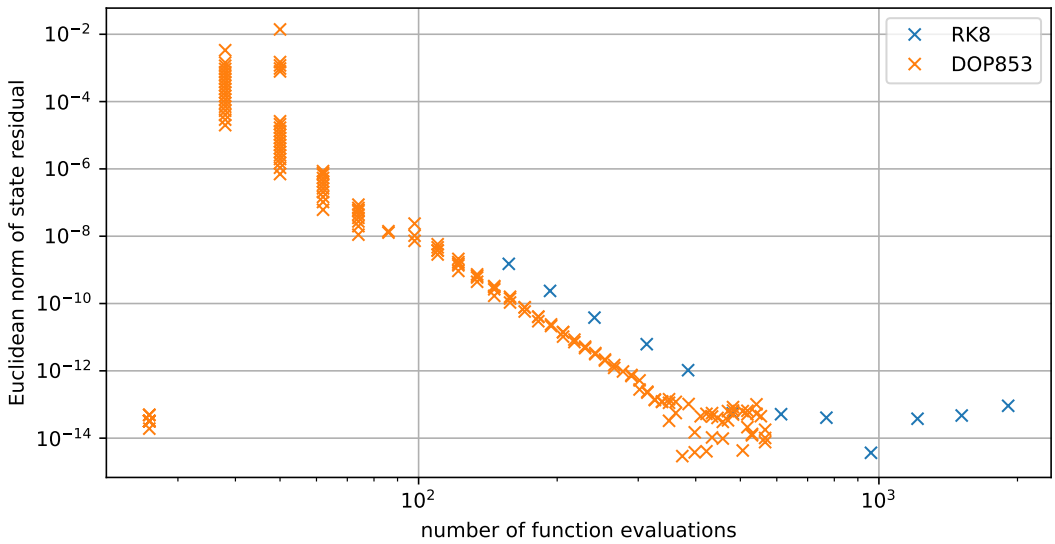

Figure B.7: Figure 5.13 for $\mu = 0.1$ (PCLS).

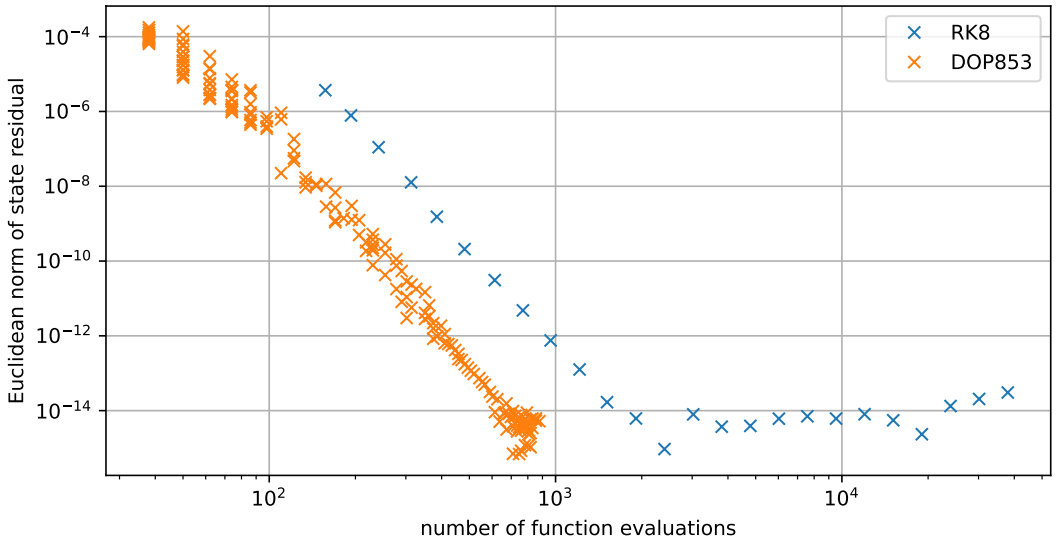

Figure B.8: Figure 5.14 for $\mu = 0.1$ (PCLS).

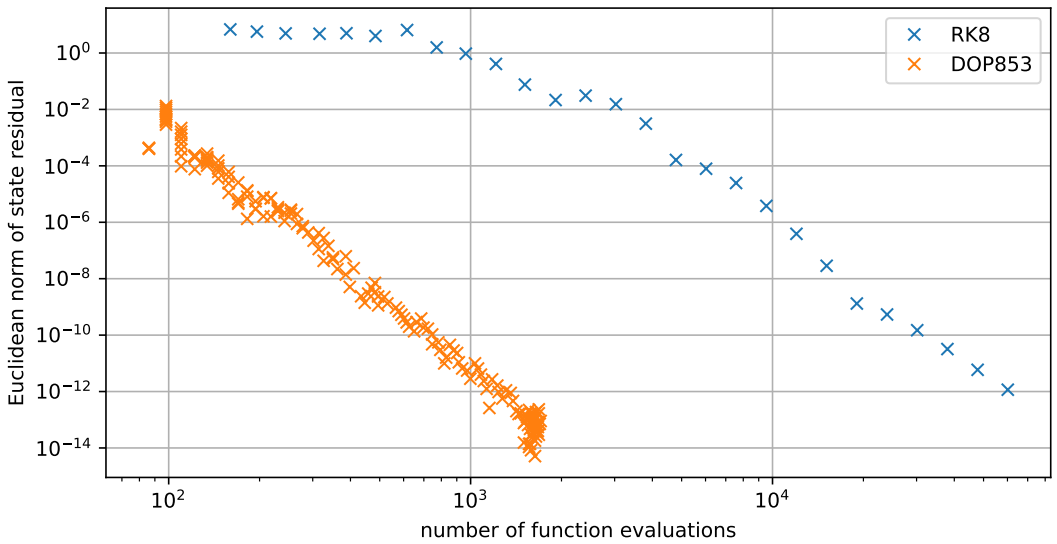

Figure B.9: Figure 5.15 for $\mu = 0.1$ (PCLS).

C

Velocity for Modeled Orbits

This appendix is inspired by [17]. It shows how the velocity can be calculated analytically from the model developed in Chapter 6. The position on the DRO with the starting location x_0 depending on the parameter ψ is:

$$x(x_0,\psi) = x_1 + (1 + c(x_0,\psi)\cos(\psi))\cos(2c(x_0,\psi)\sin(\psi)) \tag{C.1}$$

$$y(x_0,\psi) = (1 + c(x_0,\psi)\cos(\psi))\sin(2c(x_0,\psi)\sin(\psi)) \tag{C.2}$$

With the function $c(x_0,\psi)$ being approximated with:

$$c(x_0,\psi) = \sum_{n=0}^{N} a_n(x_0)\cos(n\psi) \qquad \text{and} \qquad a_n(x_0) = \sum_{s=0}^{C} p_{n,s}x_0^s \tag{C.3}$$

According to Equation (3.10), the Jacobi constant $C(x_0)$ in the xy-plane is:

$$C(x_0) = \frac{1}{2}\left(x^2(x_0,\psi) + y^2(x_0,\psi)\right) + \frac{1-\mu}{r_1(x_0,\psi)} + \frac{\mu}{r_2(x_0,\psi)} - \frac{1}{2}\left(\dot{x}^2(x_0,\psi) + \dot{y}^2(x_0,\psi)\right) \tag{C.4}$$

The Jacobi constant $C(x_0)$ has to be known. Then, the velocity $v(x_0,\psi)$ is:

$$v(x_0,\psi) = \sqrt{\dot{x}^2(x_0,\psi) + \dot{y}^2(x_0,\psi)} = \sqrt{\left(x^2(x_0,\psi) + y^2(x_0,\psi)\right) + \frac{2(1-\mu)}{r_1(x_0,\psi)} + \frac{2\mu}{r_2(x_0,\psi)} - 2C(x_0)} \tag{C.5}$$

The direction of the velocity can be found out with the partial derivatives:

$$\begin{aligned}\frac{\partial x(x_0,\psi)}{\partial\psi} = &-\left(1 + c(x_0,\psi)\cos(\psi)\right)\sin\left(2c(x_0,\psi)\sin(\psi)\right)\left(2c(x_0,\psi)\cos(\psi) + 2\frac{\partial c(x_0,\psi)}{\partial x_0}\sin(\psi)\right)\\ &+\left(-c(x_0,\psi)\sin(\psi) + c'(x_0,\psi)\cos(\psi)\right)\cos\left(2c(x_0,\psi)\sin(\psi)\right)\end{aligned} \tag{C.6}$$

$$\begin{aligned}\frac{\partial y(x_0,\psi)}{\partial\psi} = &\left(1 + c(x_0,\psi)\cos(\psi)\right)\cos\left(2c(x_0,\psi)\sin(\psi)\right)\left(2c(x_0,\psi)\cos(\psi) + 2\frac{\partial c(x_0,\psi)}{\partial x_0}\sin(\psi)\right)\\ &+\left(-c(x_0,\psi)\sin(\psi) + c'(x_0,\psi)\cos(\psi)\right)\sin\left(2c(x_0,\psi)\sin(\psi)\right)\end{aligned} \tag{C.7}$$

With the partial derivative $\partial c(x_0,\psi)/\partial x_0$ being:

$$\frac{\partial c(x_0,\psi)}{\partial x_0} = \sum_{n=0}^{N}\left(\sum_{s=1}^{C} s p_{n,s}x_0^{s-1}\right)\cos(n\psi) \tag{C.8}$$

Then, the velocity components $\dot{x}(x_0,\psi)$ and $\dot{y}(x_0,\psi)$ are:

$$\begin{bmatrix}\dot{x}(x_0,\psi)\\ \dot{y}(x_0,\psi)\end{bmatrix} = \frac{v(x_0,\psi)}{\sqrt{\left(\frac{\partial x(x_0,\psi)}{\partial\psi}\right)^2 + \left(\frac{\partial y(x_0,\psi)}{\partial\psi}\right)^2}}\begin{bmatrix}\frac{\partial x(x_0,\psi)}{\partial\psi}\\ \frac{\partial y(x_0,\psi)}{\partial\psi}\end{bmatrix} \tag{C.9}$$

D

Jacobi Constant with Perturbation

In this appendix a constant in the PCR3BP similar to the Jacobi Constant in the CR3BP shall be derived. In the PCR3BP, the equations of motion are (compare to Equations (3.3) to (3.5) and (7.9)):

$$\ddot{x} = x - \frac{1-\mu}{r_1^3}(\mu + x) + \frac{\mu}{r_2^3}(1 - \mu - x) + 2\dot{y} + a_x \tag{D.1}$$

$$\ddot{y} = y - \frac{1-\mu}{r_1^3}y - \frac{\mu}{r_2^3}y - 2\dot{x} + a_y \tag{D.2}$$

$$\ddot{z} = -\frac{1-\mu}{r_1^3}z - \frac{\mu}{r_2^3}z \tag{D.3}$$

An equivalent to the Jacobi constant in the CR3BP can be defined in the PCR3BP:

$$C = \underbrace{\frac{1}{2}x^2 + \frac{1}{2}y^2}_{K} + \underbrace{\frac{1-\mu}{r_1^2}}_{L} + \underbrace{\frac{\mu}{r_2}}_{M} + \underbrace{a_x x + a_y y}_{N} \underbrace{-\frac{1}{2}\dot{x}^2}_{O} \underbrace{-\frac{1}{2}\dot{y}^2}_{P} \underbrace{-\frac{1}{2}\dot{z}^2}_{Q} \tag{D.4}$$

With

$$r_1 = \sqrt{(x+\mu)^2 + y^2 + z^2} \quad \text{and} \quad r_2 = \sqrt{(x-1+\mu)^2 + y^2 + z^2} \tag{D.5}$$

and thus

$$\dot{r}_1 = \frac{(x+\mu)\dot{x} + y\dot{y} + z\dot{z}}{r_1} \quad \text{and} \quad \dot{r}_2 = \frac{(x-1+\mu)\dot{x} + y\dot{y} + z\dot{z}}{r_2} \tag{D.6}$$

the time derivatives of K, L, M, N, O, P, and Q calculate to:

$$\dot{K} = \underbrace{x\dot{x}}_{\text{I}} + \underbrace{y\dot{y}}_{\text{II}} \tag{D.7}$$

$$\dot{L} = -\frac{1-\mu}{r_1^3}\left(\underbrace{(x+\mu)\dot{x}}_{\text{III}} + \underbrace{y\dot{y}}_{\text{IV}} + \underbrace{z\dot{z}}_{\text{V}}\right) \tag{D.8}$$

$$\dot{M} = -\frac{\mu}{r_2^3}\left(\underbrace{(x-1+\mu)\dot{x}}_{\text{VI}} + \underbrace{y\dot{y}}_{\text{VII}} + \underbrace{z\dot{z}}_{\text{VIII}}\right) \tag{D.9}$$

$$\dot{N} = \underbrace{a_x\dot{x}}_{\text{IX}} + \underbrace{a_y\dot{y}}_{\text{X}} \tag{D.10}$$

$$\dot{O} = -\dot{x}\ddot{x} = \underbrace{-x\dot{x}}_{\text{I}} + \underbrace{\frac{1-\mu}{r_1^3}(\mu + x)\dot{x}}_{\text{III}} \underbrace{-\frac{\mu}{r_2^3}(1 - \mu - x)\dot{x}}_{\text{VI}} \underbrace{-2\dot{x}\dot{y}}_{\text{XI}} \underbrace{-a_x\dot{x}}_{\text{IX}} \tag{D.11}$$

$$\dot{P} = -\dot{y}\ddot{y} = \underbrace{-y\dot{y}}_{\text{II}} + \underbrace{\frac{1-\mu}{r_1^3}y\dot{y}}_{\text{IV}} + \underbrace{\frac{\mu}{r_2^3}y\dot{y}}_{\text{VII}} + \underbrace{2\dot{x}\dot{y}}_{\text{XI}} \underbrace{-a_y\dot{y}}_{\text{X}} \tag{D.12}$$

$$\dot{Q} = -\dot{z}\ddot{z} = \underbrace{\frac{1-\mu}{r_1^3}z\dot{z}}_{\text{V}} + \underbrace{\frac{\mu}{r_2^3}z\dot{z}}_{\text{VIII}} \tag{D.13}$$

In the sum

$$\dot{C} = \dot{K} + \dot{L} + \dot{M} + \dot{N} + \dot{O} + \dot{P} + \dot{Q} \tag{D.14}$$

all term that have in same roman number in Equations (D.7) to (D.13) cancel each other out. Therefore:

$$\dot{C} = 0 \tag{D.15}$$

Bibliography

[1] Sergey Aksenov, Stanislav Bober, and Maria Guskova. Mapping of initial conditions for libration point orbits. *Advances in Space Research*, 68(6):2501–2514, September 2021. ISSN 02731177. doi: 10.1016/j.asr.2021.04.035. URL https://linkinghub.elsevier.com/retrieve/pii/S0273117721003343.

[2] Andrew Jones. A Chinese spacecraft is testing out a new orbit around the moon, February 2022. URL https://spacenews.com/a-chinese-spacecraft-is-testing-out-a-new-orbit-around-the-moon/. Accessed: 13-04-2022.

[3] Astronomical Institute of the Czech Academy of Sciences. Binary Asteroid Parameters, 2019. URL http://www.asu.cas.cz/~asteroid/binastdata.htm. Accessed: 18-10-2021.

[4] R. H. Battin. *An introduction to the mathematics and methods of astrodynamics*. AIAA education series. American Institute of Aeronautics and Astronautics, Reston, VA, rev. ed. edition, 1999. ISBN 978-1-56347-342-5.

[5] D. Benest. Effects of the Mass Ratio on the Existence of Retrograde Satellites in the Circular Plane Restricted Problem. *Astronomy and Astrophysics*, 32:39, April 1974. ISSN 0004-6361. URL http://adsabs.harvard.edu/abs/1974A%26A....32...39B.

[6] C. J. Bezrouk and J. S. Parker. Long Duration Stability of Distant Retrograde Orbits. In *AIAA/AAS Astrodynamics Specialist Conference*, San Diego, CA, August 2014. American Institute of Aeronautics and Astronautics. ISBN 978-1-62410-308-7. doi: 10.2514/6.2014-4424. URL http://arc.aiaa.org/doi/10.2514/6.2014-4424.

[7] C. J. Bezrouk and J. S. Parker. Long term evolution of distant retrograde orbits in the Earth-Moon system. *Astrophysics and Space Science*, 362(9):176, August 2017. ISSN 1572-946X. doi: 10.1007/s10509-017-3158-0. URL https://doi.org/10.1007/s10509-017-3158-0.

[8] D. Boccaletti and G. Pucacco. *Theory of orbits*. Astronomy and astrophysics library. Springer, Berlin; New York, corr. 3rd print edition, 2004. ISBN 978-3-540-58963-1.

[9] Carl Ludwig Charlier. *Die Mechanik des Himmels Band 1*. De Gruyter, December 1927. ISBN 978-3-11-142415-6. doi: 10.1515/9783111424156. URL https://www.degruyter.com/document/doi/10.1515/9783111424156/html.

[10] Kathleen Connor Howell. Three-dimensional, periodic, halo orbits. *Celestial Mechanics*, 32(1): 53–71, January 1984. ISSN 0008-8714, 1572-9478. doi: 10.1007/BF01358403. URL http://link.springer.com/10.1007/BF01358403.

[11] Merton E. Davies, Patricia G. Rogers, and Tim R. Colvin. A control network of Triton. *Journal of Geophysical Research: Planets*, 96(E1):15675–15681, August 1991. ISSN 01480227. doi: 10.1029/91JE00976. URL http://doi.wiley.com/10.1029/91JE00976.

[12] D. Dirkx and K. Cowan. AE4868 – Numerical Astrodynamics – Acceleration Models, November 2019. Delft University of Technology, Delft, The Netherlands.

[13] A. Farkas-Takács, Cs. Kiss, A. Pál, L. Molnár, Gy. M. Szabó, O. Hanyecz, K. Sárneczky, R. Szabó, G. Marton, M. Mommert, R. Szakáts, T. Müller, and L. L. Kiss. Properties of the Irregular Satellite System around Uranus Inferred from *K2* , *Herschel* , and *Spitzer* Observations. *The Astronomical Journal*, 154(3):119, August 2017. ISSN 1538-3881. doi: 10.3847/1538-3881/aa8365. URL https://iopscience.iop.org/article/10.3847/1538-3881/aa8365.

[14] M. Henon. Numerical Exploration of the Restriced Problem. V. Hill's Case: Periodic Orbits and Their Stability. *Astron. & Astrophys.*, 1:223–238, November 1968. URL https://ui.adsabs.harvard.edu/abs/1969A%26A.....1..223H/abstract. Accessed: 05-10-2020.

[15] G. W. Hill. Researches in the Lunar Theory. *American Journal of Mathematics*, 1(1):5–26, 1878. ISSN 0002-9327. doi: 10.2307/2369430. URL https://www.jstor.org/stable/2369430. Publisher: Johns Hopkins University Press.

[16] G. W. Hill. On the part of the motion of the lunar perigee which is a function of the mean motions of the sun and moon. *Acta Mathematica*, 8(0):1–36, 1886. ISSN 0001-5962. doi: 10.1007/BF02417081. URL http://projecteuclid.org/euclid.acta/1485888530.

[17] A. N. Hirani and R. P. Russell. Approximations of distant retrograde orbits for mission design. January 2006. URL https://trs.jpl.nasa.gov/handle/2014/38896.

[18] J. Jackson. Retrograde Satellite Orbits. *Monthly Notices of the Royal Astronomical Society*, 74(2):62–82, December 1913. ISSN 0035-8711, 1365-2966. doi: 10.1093/mnras/74.2.62. URL https://academic.oup.com/mnras/article-lookup/doi/10.1093/mnras/74.2.62.

[19] R. A. Jacobson, J. K. Campbell, A. H. Taylor, and S. P. Synnott. The masses of Uranus and its major satellites from Voyager tracking data and earth-based Uranian satellite data. *The Astronomical Journal*, 103:2068, June 1992. ISSN 00046256. doi: 10.1086/116211. URL http://adsabs.harvard.edu/cgi-bin/bib_query?1992AJ....103.2068J.

[20] Jet Propulsion Laboratory. Astronomic Constants, 2021. URL https://ssd.jpl.nasa.gov/?constants. Accessed: 22-09-2021.

[21] E Karkoschka. Voyager's Eleventh Discovery of a Satellite of Uranus and Photometry and the First Size Measurements of Nine Satellites. *Icarus*, 151(1):69–77, May 2001. ISSN 00191035. doi: 10.1006/icar.2001.6597. URL https://linkinghub.elsevier.com/retrieve/pii/S0019103501965972.

[22] E Karkoschka. Sizes, shapes, and albedos of the inner satellites of Neptune. *Icarus*, 162(2):400–407, April 2003. ISSN 00191035. doi: 10.1016/S0019-1035(03)00002-2. URL https://linkinghub.elsevier.com/retrieve/pii/S0019103503000022.

[23] C. Kiss, A. Pál, A. I. Farkas-Takács, G. M. Szabó, R. Szabó, L. L. Kiss, L. Molnár, K. Sárneczky, T. G. Müller, M. Mommert, and J. Stansberry. Nereid from space: rotation, size and shape analysis from K2, *Herschel* and *Spitzer* observations. *Monthly Notices of the Royal Astronomical Society*, 457(3):2908–2917, April 2016. ISSN 0035-8711, 1365-2966. doi: 10.1093/mnras/stw081. URL https://academic.oup.com/mnras/article-lookup/doi/10.1093/mnras/stw081.

[24] Kristin Burke. What is China doing at the lunar distant retrograde orbit?, April 2022. URL https://www.thespacereview.com/article/4365/1. Accessed: 13-04-2022.

[25] Jet Propulsion Laboratory. Planetary Satellite Physical Parameters, 2021. URL https://ssd.jpl.nasa.gov/sats/phys_par/. Accessed: 11-05-2022.

[26] T. Lam and G. J. Whiffen. Exploration of Distant Retrograde Orbits Around Europa (AAS 05-110). *Advances in the Astronautical Sciences*, 120, January 2005. URL https://trs.jpl.nasa.gov/bitstream/handle/2014/37526/05-0195.pdf. In: Vallado DA, Gabor MJ, Desai PN (eds) AAS/AIAA Spaceflight Mechanics Meeting 2005, American Astronautical Society, Univelt, Inc., USA.

[27] M. Lara, R. Russell, and B. Villac. Classification of the Distant Stability Regions at Europa. *Journal of Guidance, Control, and Dynamics*, 30(2):409–418, 2007. doi: 10.2514/1.22372. URL https://doi.org/10.2514/1.22372.

[28] Chris Lewicki, Peter Diamandis, Eric Anderson, Chris Voorhees, and Frank Mycroft. Planetary Resources—The Asteroid Mining Company. *New Space*, 1(2):105–108, June 2013. ISSN 2168-0256, 2168-0264. doi: 10.1089/space.2013.0013. URL https://www.liebertpub.com/doi/10.1089/space.2013.0013.

[29] Takehiko Matukuma. Periodic Orbits in Hill's Case. Third Paper (Periodic Ejectional Orbit). *Proceedings of the Imperial Academy*, 9(8):364–366, 1933. ISSN 0369-9846, 1881-1140. doi: 10.2183/pjab1912.9.364. URL https://www.jstage.jst.go.jp/article/pjab1912/9/8/9_8_364/_article.

[30] X. Ming and X. Shijie. Exploration of distant retrograde orbits around Moon. *Acta Astronautica*, 65(5):853–860, September 2009. ISSN 0094-5765. doi: 10.1016/j.actaastro.2009.03.026. URL http://www.sciencedirect.com/science/article/pii/S0094576509001404.

[31] B. K. Muirhead and J. R. Brophy. Asteroid Redirect Robotic Mission feasibility study. In *2014 IEEE Aerospace Conference*, pages 1–14, March 2014. doi: 10.1109/AERO.2014.6836358. ISSN: 1095-323X.

[32] National Aeronautics and Space Administration. Solar System Small Worlds Fact Sheet, April 2016. URL https://nssdc.gsfc.nasa.gov/planetary/factsheet/galileanfact_table.html. Accessed: 22-09-2021.

[33] National Aeronautics and Space Administration. Mars Fact Sheet, December 2021. URL https://nssdc.gsfc.nasa.gov/planetary/factsheet/marsfact.html. Accessed: 22-09-2021.

[34] National Aeronautics and Space Administration. Moon Fact Sheet, December 2021. URL https://nssdc.gsfc.nasa.gov/planetary/factsheet/moonfact.html. Accessed: 22-09-2021.

[35] National Aeronautics and Space Administration. Planetary Fact Sheet - Metric, December 2021. URL https://nssdc.gsfc.nasa.gov/planetary/factsheet/. Accessed: 22-09-2021.

[36] National Aeronautics and Space Administration. Pluto Fact Sheet, December 2021. URL https://nssdc.gsfc.nasa.gov/planetary/factsheet/plutofact.html. Accessed: 22-09-2021.

[37] J. S. Parker and R. L. Anderson. *Low-Eenergy Lunar Trajectory Design*. John Wiley & Sons, Inc., Hoboken, NJ, USA, June 2014. ISBN 978-1-118-85506-5 978-1-118-85387-0. doi: 10.1002/9781118855065. URL http://doi.wiley.com/10.1002/9781118855065.

[38] P. Pires and O. C. Winter. Location and stability of distant retrograde orbits around the Moon. *Monthly Notices of the Royal Astronomical Society*, 494(2):2727–2735, May 2020. ISSN 0035-8711, 1365-2966. doi: 10.1093/mnras/staa887. URL https://academic.oup.com/mnras/article/494/2/2727/5817352.

[39] D. J. Scheeres. *Orbital motion in strongly perturbed environments: applications to asteroid, comet and planetary satellite orbiters*. Springer-Praxis books in astronautical engineering. Springer; Published in association with Praxis Publishing, Heidelberg; New York: Chichester, UK, 2012. ISBN 978-3-642-03255-4. OCLC: ocn428029964.

[40] Scott S. Sheppard, David Jewitt, and Jan Kleyna. An Ultradeep Survey for Irregular Satellites of Uranus: Limits to Completeness. *The Astronomical Journal*, 129(1):518–525, January 2005. ISSN 0004-6256, 1538-3881. doi: 10.1086/426329. URL https://iopscience.iop.org/article/10.1086/426329.

[41] Mark R. Showalter and Jack J. Lissauer. The Second Ring-Moon System of Uranus: Discovery and Dynamics. *Science*, 311(5763):973–977, February 2006. ISSN 0036-8075, 1095-9203. doi: 10.1126/science.1122882. URL https://www.science.org/doi/10.1126/science.1122882.

[42] Philip J. Stooke. The surfaces of Larissa and Proteus. *Earth, Moon, and Planets*, 65(1):31–54, 1994. ISSN 0167-9295, 1573-0794. doi: 10.1007/BF00572198. URL http://link.springer.com/10.1007/BF00572198.

[43] The Planetary Society. Chang'e-5: China's Moon sample return mission, 2021. URL https://www.planetary.org/space-missions/change-5. Accessed: 13-04-2022.

[44] The SciPy community. scipy.integrate.solve_ivp, 2022. URL https://docs.scipy.org/doc/scipy/reference/generated/scipy.integrate.solve_ivp.html. Accessed: 15-02-2022.

[45] The University of Texas at Austin. Normalized Gravity Coefficients. URL http://www.csr.utexas.edu/publications/statod/TabD.3.new.txt. Accessed: 18-11-2020.

[46] P.C. Thomas. Radii, shapes, and topography of the satellites of Uranus from limb coordinates. *Icarus*, 73(3):427–441, March 1988. ISSN 00191035. doi: 10.1016/0019-1035(88)90054-1. URL https://linkinghub.elsevier.com/retrieve/pii/0019103588900541.

[47] P.C. Thomas. The Shape of Triton from Limb Profiles. *Icarus*, 148(2):587–588, December 2000. ISSN 00191035. doi: 10.1006/icar.2000.6511. URL https://linkinghub.elsevier.com/retrieve/pii/S0019103500965114.

[48] P.C. Thomas. Sizes, shapes, and derived properties of the saturnian satellites after the Cassini nominal mission. *Icarus*, 208(1):395–401, July 2010. ISSN 00191035. doi: 10.1016/j.icarus.2010.01.025. URL https://linkinghub.elsevier.com/retrieve/pii/S0019103510000448.

[49] G. Turner. Results of long-duration simulation of Distant Retrograde Orbits. *Aerospace*, 3(4), 2016. doi: 10.3390/aerospace3040037.

[50] K. F. Wakker. *Fundamentals of Astrodynamics*. Institutional Repository, Library, Delft University of Technology, Delft, The Netherlands, January 2015. ISBN 978-94-6186-419-2. URL http://resolver.tudelft.nl/uuid:3fc91471-8e47-4215-af43-718740e6694e.

[51] T. Widemann and others. Titania's radius and an upper limit on its atmosphere from the September 8, 2001 stellar occultation. *Icarus*, 199(2):458–476, February 2009. ISSN 00191035. doi: 10.1016/j.icarus.2008.09.011. URL https://linkinghub.elsevier.com/retrieve/pii/S0019103508003400.